# Mechanics and Collective Cell Migration

James Nicholas Graham

Pembroke College
University of Oxford

*A thesis submitted for the degree of*
*Doctor of Philosophy*

Trinity 2024

## Abstract

'Active matter' is a term used to describe non-equilibrium systems, such as living organisms and tissues, that do work using an external source of energy. Epithelial cells are a subclass of living systems that derive their energy from ATP hydrolysis and are driven by active processes in the cytoskeleton. Epithelial cells can migrate as individuals, but also organise into two-dimensional monolayers and give rise to rich emergent behaviours such as collective migration and nematic liquid-crystalline order, with implications for morphogenesis, growth, and cancer metastasis. In this Thesis we model epithelia as two-dimensional monolayers to study their collective behaviours.

Using a multi-phase field model for epithelia, we first study the contributions of polar activity and cell-cell adhesion to the rotation of pairs of cells in confinement. Then we dispense with polar activity in favour of dipolar active stresses in order to study bulk epithelia. We investigate the microphase separation of mixtures of extensile and contractile dipolar cells. Cell sorting of this type has been observed in experiment and is relevant to embryogenesis and morphogenesis, and we propose an active origin for the observations.

Then we focus on cell intercalations, which are responsible in part for tissue fluidisation and therefore collective migration. We model fluctuations in the number of cadherin proteins at adherens junctions between cells using an Ornstein-Uhlenbeck process. We vary the timescale and variance of the random process and find a region that promotes translational diffusion and neighbour rearrangements, and show that the orientational order in the system vanishes. We also find that the translational diffusion has a non-monotonic dependence on the timescale of the adhesion fluctuations.

Finally, we study the flow of epithelia confined to a channel. Plug and shear flow have been observed in experiment and have implications for gastrulation in the embryo. First, we recover macroscopic flow for contractile cells by enforcing cell orientations at the edge the channel. Then we reformulate the force balance in the multi-phase field model to include Stokesian dynamics and, therefore, internal friction. The improved model exhibits an oscillatory shear flow that becomes more persistent as the coefficient of internal friction is increased. This development helps to bridge the gap from microscopic models to continuum theories.

# Mechanics and Collective Cell Migration


James Nicholas Graham

Pembroke College

University of Oxford

A thesis submitted for the degree of

*Doctor of Philosophy*

Trinity 2024

# Abstract

'Active matter' is a term used to describe non-equilibrium systems, such as living organisms and tissues, that do work using an external source of energy. Epithelial cells are a subclass of living systems that derive their energy from ATP hydrolysis and are driven by active processes in the cytoskeleton. Epithelial cells can migrate as individuals, but also organise into two-dimensional monolayers and give rise to rich emergent behaviours such as collective migration and nematic liquid-crystalline order, with implications for morphogenesis, growth, and cancer metastasis. In this Thesis we model epithelia as two-dimensional monolayers to study their collective behaviours.

Using a multi-phase field model for epithelia, we first study the contributions of polar activity and cell-cell adhesion to the rotation of pairs of cells in confinement. Then we dispense with polar activity in favour of dipolar active stresses in order to study bulk epithelia. We investigate the microphase separation of mixtures of extensile and contractile dipolar cells. Cell sorting of this type has been observed in experiment and is relevant to embryogenesis and morphogenesis, and we propose an active origin for the observations.

Then we focus on cell intercalations, which are responsible in part for tissue fluidisation and therefore collective migration. We model fluctuations in the number of cadherin proteins at adherens junctions between cells using an Ornstein-Uhlenbeck process. We vary the timescale and variance of the random process and find a region that promotes translational diffusion and neighbour rearrangements, and show that the orientational order in the system vanishes. We also find that the translational diffusion has a non-monotonic dependence on the timescale of the adhesion fluctuations.

Finally, we study the flow of epithelia confined to a channel. Plug and shear flow have been observed in experiment and have implications for gastrulation in the embryo. First, we recover macroscopic flow for contractile cells by enforcing cell orientations at the edge the channel. Then we reformulate the force balance in the multi-phase field model to include Stokesian dynamics and, therefore, internal friction. The improved model exhibits an oscillatory shear flow that becomes more persistent as the coefficient of internal friction is increased. This development helps to bridge the gap from microscopic models to continuum theories.

# Acknowledgements

It is with deepest gratitude to my supervisor, Professor Julia M. Yeomans, that I submit this Thesis. Thank you for bringing me into the world of biophysics through your research. Thank you for your guidance, questioning, and discussion, and for believing in me even when I did not believe in myself. It is only with your support that I have been able to develop, present, write, and publish my research projects.

To everyone else in theoretical biophysics, whose research interests complement and intersect with mine: Alex Mietke for his probing questions, and Francesco Mori, Jan Rozman and Rahil Valani for their insightful thoughts and fruitful discussions, and Jan especially for his collaboration. Thanks you to fellow students in and out of the group: Saraswat Bhattacharyya, Kristian Thijssen, Rian Hughes, Guanming Zhang, Liam Ruske, Mehrana R. Nejad, Muriel van der Laan, Ioannis Hadjifrangiskou, Alva Orr, and Robbie Ewart. Thanks also to Michelle Jose for her warm kindness.

Thank you to everyone at Pembroke who has believed in me over the years, through good and bad. To Sir Ernest and Lady Janette Ryder, Tim Woollings, Caroline Barnes, and Andrew Teal: thank for having more patience with me than I deserve, and thank you for making college such a welcoming place for me and those before me. I know Pembroke will remain a tight-knit, warm scholarly community for centuries to come, and that many more students will find their home there.

I am grateful to all the communities I have found during my time at Oxford. To my old friends from our MSc cohort: Jonathan Schulz, Diego Berdeja Suarez, Christoph Weis, and Ambrose Yim, with whom it is always a joy to talk. To new friends in college: Cat Ashworth, Benjamin Bréant, Rohan Watt, and Kathryn White, who keep me level and grounded, but not always on the straight and narrow.

To all the cyclists, and most of all to Pat Maclean, Pedr Charlesworth, Georgia Acton, Becky Strain, and Izzy Leitch for a host of mad adventures. Thank you Sarah McKeown. Thank you to the fencers, to my second team, and especially to Lucas Baude de Bunnetat for their kind and welcoming sporting and social community. Thank you also to Pembroke College Boat Club and to Nik Baya in particular for encouraging me to row in the first place. Thank you to Simon Kerswell-Jensen and Harry Lyons for bringing out the best in me.

Thank you most of all to my parents, John and Sue, who have believed in me much more deeply and for far longer than anyone else in the world. I couldn't have done any of this, or anything else, without you.

# Publications

There is one authored publication contributing to this thesis:

> Graham, J. N., Zhang, G. & Yeomans, J. M. Cell sorting by active forces in a phase-field model of cell monolayers. Soft Matter **20**, 2955-2960 (2024).

There is one manuscript currently in preparation for publication contributing to this thesis:

> Graham, J. N. & Rozman, J. Adhesion-Fluctuation-Mediated Fluidisation of Phase-Field Epithelial Monolayers. In preparation (2024).

# Contents

# List of Figures

# List of Tables

*"Will you walk a little faster?" said a whiting to a snail,*

*"There's a porpoise close behind us, and he's treading on my tail.*

*See how eagerly the lobsters and the turtles all advance!*

*They are waiting on the shingle—will you come and join the dance?"*

— Lewis Carroll [1]

# 1 Introduction

'Active matter' is a broad label in non-equilibrium physics for systems that take energy from an external source and inject it into the surroundings as work [3]. These energy sources are varied: they include, for example, external driving, as in vibrated granular systems [3, 4], the catalytic hydrolysis of fuel in the bulk, as for Janus particles [4], or surfactant gradients across a droplet resulting in diffusiophoresis, as in systems of swimming droplets [5]. Critically, however, active matter also includes biological systems, on length scales ranging from subcellular components of the cytoskeleton up to flocks of macroscopic animals such as birds [4], and are generically driven by ATP hydrolysis [6].

In biology, cells are a fundamental building block, not only for multicellular organisms, but also for collectives of unicellular organisms such as biofilms and slime moulds [7, 8]. In this sense, cells are an emblematic representation of the 'More is Different' paradigm in condensed matter [9]. Cells migrate both individually and collectively, and provide therefore a rich platform for theoretical and experimental biophysics in the category of active matter. In this Thesis, we restrict our attention to epithelial cells, which join together tightly into layers, as well as into tubes and sacs [10], and can also be cultured *in vitro* as two-dimensional sheets. Embryos consist substantially of epithelial cells [10]; therefore, the study of epithelia is crucial to the understanding of morphogenesis and development [8,

11]. Epithelial tissues are also ubiquitous in fully-developed organisms, and play a role in tumorigenesis and metastasis [10].

Epithelia exhibit rich physics: force transduction from a cell to a substrate, as well as between cells, results in a number of individual and collective phenomena [8, 12–14]. These behaviours admit descriptions by active continuum theories [6, 7] that have themselves been validated *in vitro*. Agent-based models have, too, been used to describe epithelia, and it is in turn the role of these models to bridge the gap from the scale of an individual cell to the continuum. In this Thesis, we use a multi-phase field model to study the collective behaviours of epithelial cells, from persistent rotational motion in confinement to phase separation, neighbour intercalations and flow in a channel *via* monolayer fluidisation.

## 1.1 Individual Cell Motility

The collective behaviours of epithelia emerge from the motility of and stresses generated by individual epithelial cells. These stresses and motility arise from the interplay of the internal structure of a cell with the substrate and larger environment *via* chemical and physical signalling [12–14]. The actomyosin cortex and microtubules within a cell are the structures primarily responsible for migration and force transduction, and themselves exhibit polar and dipolar features that are reflected in the behaviour of the larger cell [15, 16]. While a polar force propels a particle along a particular axis, dipolar stresses result in pairs of forces pointing either inward or outward along a chosen axis, and therefore have a head-tail symmetry.

The actomyosin cortex, which crosslinks microtobules and provides structure to the cell membrane, is composed of actin filaments, themselves crosslinked by filaments of myosin-II molecular motors. The actin fibres are polar, a result of the geometry of the monomers from which they are formed, and preferentially polymerise at one end and depolymerise at the other. In addition, the myosin-II motors that create stresses within the actomyosin cortex are oriented on the fibres to which they are attached [15]. The actin filaments can orient parallel or anti-parallel to each other, and can create active isotropic or anisotropic stresses [17,

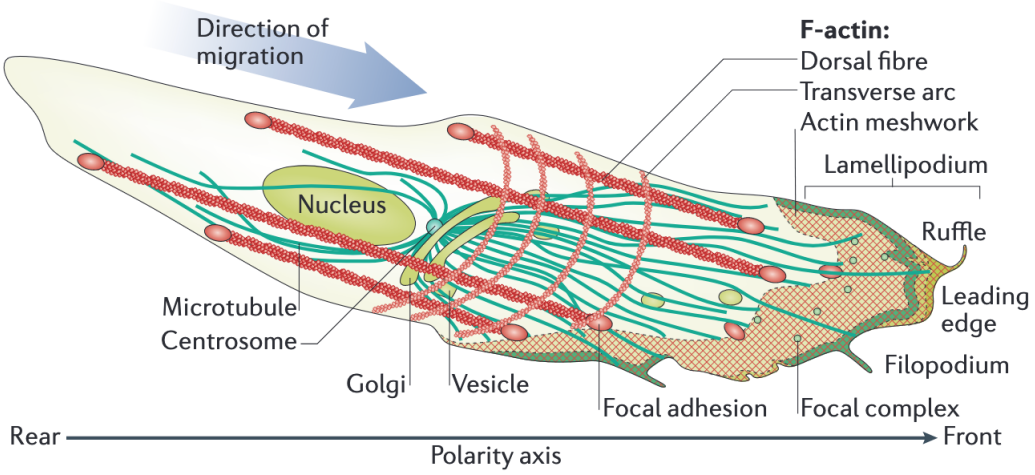


**Figure 1.1:** Schematic of a single migrating cell illustrating the major components of the cytoskeleton including microtubules, actin fibres and the polymerising actin cortex in the lamellipodium. The cell has an emergent axis of polarity along which it migrates. Adapted from [13].

18]. Analogously, microtubules are polar in both structure and polymerisation [15]. Kinesin molecular motors, similarly, have a preferred orientation when attached to microtubules and, when they crosslink a network of microtubules, create active stresses both isotropic and anisotropic within the cell [16].

Cell motility originates from the coordination of four processes: protrusion, adhesion, contraction, and retraction [19], which are fundamentally linked to the behaviours of microtubules and the actomyosin cortex. Figure 1.1 illustrates the organisation of microtubules and the actomyosin cortex within a single migrating cell. The polymerisation of microtubules causes piconewton-scale forces that deform cell membranes [20], and actomyosin provides structure to protrusions such as lamellipodia at the front of a cell [13]. These protrusions, along with the orientations of microtubules within the cell, break front-back symmetry and assign a direction for migration [13, 19].

Cells adhere to the substrate using integrin proteins at sites called focal adhesions, which are attached to the actomyosin network [21]. Microtubules, too, mediate the flow of integrins within the cell, promoting the formation of focal adhesions, and also control the disassembly of adhesions [19]. The crosslinked microtubule and

actin networks connected to the substrate *via* focal adhesions provide a foundation for the active contraction that moves a cell along its front-back axis [13].

Traction forces are applied to the substrate at focal adhesions, and are generated by the myosin-II and kinesin motor filaments embedded within the cytoskeleton [16–18]. These traction forces are exerted at both the front and the back of the cell, creating a force dipole [13, 14, 21], but polar symmetry-breaking results in a net force that pulls the cell body in the direction of migration. The active contraction results in a characteristic retrograde flow of actin cables from the front to the back of the cell [13, 19]. The final phase of migration, retraction, occurs at the rear of the cell, where focal adhesions are disassembled and both actin filaments and microtubules depolymerise [13, 14] and are recycled once again to protrude at the front of the cell [19].

The migration of a single cell is random [12] and can be described by models such as persistent random walkers [22]. The front-back symmetry is broken internally by the expression of proteins such as Rac and CDC42 that promote cytoskeletal polymerisation and the recruitment of integrins in the membrane [13, 19, 21]. However, external chemical or physical signals can also break the front-back symmetry and impose an axis of migration. For example, chemical gradients can promote directed migration in a phenomenon known as chemotaxis [11, 23–25]. Differences in substrate stiffness may also result in durotaxis [21, 26].

The features of the cytoskeleton that result in single-cell motility, including actin cables, focal adhesions and traction forces, result in emergent phenomena in the bulk. The collective behaviours of epithelial cells include tissue-scale flows, phase separation and liquid-crystalline properties.

## 1.2 Collective Cell Motility

The processes underpinning the motility of individual cells exist also in bulk tissues; however, intercellular interactions give rise to phenomena absent at the single-cell level, by distinguishing cell-cell from cell-substrate interactions [27]. Two key features of collective cell motility are the emergence of system-wide actin structures [13, 14]

and the 'contact inhibition' of individual protrusions [28]. These interactions result in diverse behaviours, including macroscopic flows and orientational order, which have been shown *in vitro* [29] as well as *in vivo* during gastrulation [30, 31].

Supracellular actin cables assemble across a monolayer and these tissue-scale fibres are advected by the retrograde actin flow [8, 13, 14]. The actin cables bridge across cell membranes at adherens junctions, which are constructed from cadherin proteins. These membrane proteins are embedded in the actomyosin cortex and support stress transduction through and between cells, including at the edge of a cluster, where an effective surface tension emerges. The supracellular network of microtubules and actomyosin creates tissue-scale active stresses [13, 14].

Adherens junctions themselves have several implications for the dynamics of epithelial monolayers. For example, cells are able to exert tractions on each other using cadherin proteins [21]. Also, the remodeling of adherens junctions permits cell rearrangements within a monolayer [8], as well as extrusions at defects in the monolayer [32]. In addition, the presence of adherens junctions suppresses the formation of focal adhesions [13] and causes a tissue to exert the largest traction forces on the substrate at its edge [14]. Clearly, cell-cell junctions and interconnected actomyosin cortices are a key source of tissue-scale stresses in epithelia.

Another key feature of bulk epithelia is the suppression of polarisation and thereby individual cell migration [11]. Cells that come into contact tend not to continue migrating and even polarise away from each other, a phenomenon first characterised by Abercrombie as 'contact inhibition' [28]. Interactions during contact inhibition of locomotion appear to be non-reciprocal: in pairwise experiments, a cell polarises away from the direction of a head-on collision more readily than it does from a collision with the rear of another cell, thereby leading to 'contact following' [33]. Certainly, the 'cryptic' lamellipodia created by cells in the bulk are smaller than those of free cells, and may indicate suppressed collective polarisation [14]. This is not to say there is no polarisation in epithelia: along the edge of a cluster, 'leader' cells with large lamellipodia can direct collective motion in the context of wound healing [12–14]

or morphogenesis [11]. These cell-cell interactions result in numerous collective behaviours, including jamming, flocking, orientational order, and phase separation.

Jamming is most clearly a result of polar activity and contact inhibition of locomotion [14]. However, epithelia are still able to flock in the bulk. Flocking is a generic feature of tissue-level behaviour and can manifest in several ways: directed migration and swirling, for example in an epithelial monolayer [14], and streaming through extracellular matrix or a second tissue, as in cancer invasion [8]. Rotational motion and collective migration have been investigated through assays on micropatterned substrates, and have been shown to emerge on a number of scales, ranging from just a pair of cells [34, 35] to tens and several tens, up to lengths of order $100\mu$m [36, 37]. Although flocking and swirling appear to be polar phenomena, flows also result from dipolar stresses, and experiments have shown clear dipolar behaviour in bulk tissues [38, 39].

Epithelia in experiment can exhibit nematic orientational order, which is unstable to flow in active systems such as cell monolayers [38, 40]. Nematic epithelia include Madin-Darby Canine Kidney (MDCK) layers [32], human bronchial epithelial cell (HBEC) monolayers [29], retinal pigment epithelium (RPE1) cells [38], and mesothelium [41]. Spontaneous shear flow has been shown also in glioma invasion, in which 'oncostreams', bundles of highly elongated, highly aligned cancer cells, migrate along collagen strands so as invade healthy tissue. The velocity fields in these streams exhibit a head-tail symmetry [42], and so can be characterised as nematic.

Not only are uniform dipolar stresses an emergent feature of epithelia, but nonuniform stresses can also lead to new emergent behaviours. Depending on the sign and magnitude of their activity, different strains of cells *in vitro* can either mix or form well-defined clusters [43], and a mixed layer can even phase separate [39]. Patterning of activity in tissues affects morphogenesis, too. Gastrulation, a crucial step in development, has been described as a patch of active material initiating a convergent extension flow in a passive background in the context of the chick embryo [30, 31].

Features of epithelial dynamics, including orientational order and spontaneous flow transitions, have been described by continuum theories and numerous agent-based models, which we now review.

## 1.3 Models for Epithelial Dynamics

There are many classes of model for epithelia, both agent-based and in the continuum. Agent-based models include vertex and Voronoi models, the Cellular Potts model, sharp-interface models, and the phase-field model, while nematohydrodynamics is a rich continuum description that reproduces many features of epithelia. All these models have inherent advantages and disadvantages, and all can be modified to account for the active forces generated by epithelial cells. In this Thesis, we use a multi-phase field model to describe epithelia.

### 1.3.1 Vertex & Voronoi Models

The vertex and Voronoi models for epithelia describe the apical surfaces of individual cells as polygons. This description is approximate, as junctions between cells are generally slightly curved [44]. The vertex and Voronoi models originate as a technique to obtain an accurate, albeit simplified, geometric description of an epithelium. As originally implemented by Honda [44], the vertices of a cell, including those with curved edges, are used to calculate the cell's approximate centre, and then a Voronoi tiling of the epithelium is constructed from the set of centres to represent the tissue geometry. This description has proven accurate and has even been used to approximate the geometry of a layer after a single cell division, given information on the axis of division and the distance between the centres of daughter cells [45], and has been improved to account also for epithelial dynamics.

Vertex and Voronoi models differ in their descriptions of the *dynamics* of epithelia: the vertices are the degrees of freedom in the vertex model, while the centres of the polygons are the degrees of freedom in the Voronoi model. In both cases, however, a free energy functional can be written for the polygons in the tiling that contains two

terms. One term assigns an area elasticity to each cell, and the other term models the line tension of the cell-cell junctions as identical Hookean springs [46–48]:

$$\tilde{\mathcal{F}} = \sum_i \left[ \frac{\tilde{K}_A}{2}(A_i - A_0)^2 + \frac{\tilde{K}_P}{2}(P_i - P_0)^2 \right] \tag{1.1}$$

where the sum is over all polygons in the system, and $A_0$ and $P_0$ are respectively the preferred area and perimeter of a single polygon. Although in the bulk the epithelial cells can be thought of as incompressible, the surface area and height of a cell can change along the apicobasal axis, and this is the origin of the area elasticity. Rescaling energy by $\tilde{K}_A A_0^2$ and lengths by $\sqrt{A_0}$ yields a new free energy

$$\mathcal{F} = \sum_i \left[ \frac{1}{2}(a_i - 1)^2 + \frac{1}{2}k(p_i - p_0)^2 \right] \tag{1.2}$$

where $a_i = A_i/A_0$, $p_i = P_i/\sqrt{A_0}$, $k = \tilde{K}_P/(\tilde{K}_A A_0)$ and $p_0 = P_0/\sqrt{A_0}$. The dimensionless parameter $p_0$ is the *shape factor* that controls the layer's crossover from solid-like to fluid-like behaviour. When $p_0 = p^*$ the critical shape factor, the shear modulus in the layer vanishes and polygons can deform to adapt to a shear stress with no free energy penalty [47]. Heuristically, the critical shape factor is the result of the target perimeter of each cell being long enough to comfortably contain its area. The critical shape factor is $p^* \approx 3.72$ for a tiling of regular hexagons, but in general depends on geometry; in a disordered system, its value has been quoted as $p^* \approx 3.81$ [49].

The dynamics of these models is given by

$$\xi \frac{\mathrm{d}\mathbf{r}_i}{\mathrm{d}t} = -\frac{\partial \mathcal{F}}{\partial \mathbf{r}_i} \tag{1.3}$$

where $\mathbf{r}_i$ denotes either a vertex of a polygon (vertex model) or its centre (Voronoi model) [46–48]. In principle, frictional forces can be implemented between neighbouring vertices or polygons so as to build cell-cell dissipation into the system [50–52].

The vertex and Voronoi models have been further modified to account for polar active forces [53]. In addition, the line tension on each junction need not be identical or constant [47]. Although relaxing this condition requires rewriting the free energy in Equation (1.1), the line tensions at junctions can then be coupled to a random

process, which fluidises the layer [54], or even coupled to orientation to enable, for instance, dipolar stresses in the model [55]. The vertex model has also been extended to describe both the apical and basal surfaces of cells in a spherical geometry [48, 56].

A substantial advantage of these models is their relative computational simplicity: a whole epithelium can be described using only a few degrees of freedom per cell. Despite the restriction of describing cell shapes using straight lines, vertex and Voronoi models can provide faithful descriptions of epithelia in both two and three dimensions [45, 47, 56]. There are, however, inherent but different drawbacks to both the vertex and Voronoi models. The Voronoi model cannot naturally handle any free edge of a cluster because the Voronoi domain of a cell on a boundary is unbounded, as recognised by Honda [44]. On the other hand, cell rearrangements are handled naturally by the Voronoi tiling, whereas in the vertex model the topology of the cells must be updated explicitly, which itself presents conceptual and algorithmic challenges. However, computing a Voronoi tiling can be computationally expensive. Both models assume the monolayer is confluent — which is not the case in experiments such as wound healing assays. In addition, both models are restricted to describing cell shapes by straight edges: a good although not perfect approximation. None of these issues is insurmountable, but other models can and do solve these problems in natural ways.

### 1.3.2 Cellular Potts Model

The cellular Potts model (CPM) is a variation of the standard Potts model for spin systems, where each cell is itself constructed from a set of spins. In a system of $N$ cells on a lattice, there is a spin at each site that can take one of $N$ values, and cell $i$ is identified with the magnetic domain where the spin is $\sigma(\mathbf{x}) = i$. A simple Hamiltonian can be written for the system [57], with terms for area elasticity and surface tension:

$$\mathcal{H} = \sum_{\text{cells } i} (A_i - A_0)^2 + \sum_{\substack{\text{neighbouring sites} \\ \mathbf{a},\mathbf{b}}} J_0(1 - \delta_{\sigma(\mathbf{a}),\sigma(\mathbf{b})}). \tag{1.4}$$

Similarly to the cellular vertex and Voronoi models, there is a harmonic potential in the area of the cell, which accounts for cell incompressibility and the unknown (in principle variable) cell heights. The area $A_i$ of a cell is simply the total number of sites where the spin is $i$. The second term is a surface tension that penalises junctions between different cells or between a cell and free space. The coefficient $J_0$ can be relaxed to a pairwise $J_{ij}$ between cells $i$ and $j$ to promote, for instance, sorting or mixing [58–60].

As in the standard Potts model, the cellular Potts model is updated stochastically, by proposing a change at site $\mathbf{a}$ from one spin to another, and accepting the change with a Boltmann weight $\min(\exp(-\Delta\mathcal{H})/T, 1)$ where $T$ is some temperature, which does not necessarily correspond to any observable [27]. Forces that are active can be implemented by biasing the Hamiltonian, for instance including a polar term $-\sum_{\mathbf{a}\in \text{ cell } i} \mathbf{p}_i \cdot (\mathbf{a} - \mathbf{a}_{COM})$ where $\mathbf{a}_{COM}$ is the centre of mass of cell $i$ [27, 57]. In this case, the stochastic update favours growth of a cell parallel to the polarisation vector $\mathbf{p}_i$, and decay antiparallel to it. Dipolar forces could also be implemented similarly, growing (decaying) a cell parallel (normal) to a preferred direction.

Computation with the CPM takes advantage of standard techniques in statistical physics. However, algorithms such as the Metropolis method that generate an equilibrium distribution of states do not manifest time in a clear sense, which is necessary for instance to calculate the mean-square displacement of cells in a system.

### 1.3.3 Sharp Interface Model

Sharp interface models are a class of model for epithelia that track the location and shape of the boundary of a cell, which evolves, like other models, according to both passive and active forces. The nature of the description and the precise degrees of freedom vary; Bresler et al. [61] derive a model for a smooth polar curve $R(\theta, t)$ and implement the model using an ordered set of points in space, which are the numerical degrees of freedom. This approach differs from the vertex model in that the contour is described by many more points than the roughly six of the vertex model, and each point in this implementation of the sharp interface model belongs

only to one cell rather than to three. The sharp interface model formulated by Saito and Ishihara [62] also describes a polar contour $R(\theta, t)$ but is implemented using a Fourier series, which can be cut off after an arbitrary number of modes, in which the Fourier coefficients are the degrees of freedom in the model. This model conserves area exactly by using Parseval's theorem to set the magnitude of the zero mode.

Both these models lend themselves to descriptions of highly deformed cells; Bresler et al. have described the behaviour of a soft cell in a background of stiff cells [61] while Saito and Ishihara characterise a rigidity transition from a solid to a fluid phase in a system of polar cells, as well as a percolation transition between a fluid phase of circular cells and a 'soft-fluid' phase of highly deformed cells, which exhibits a bimodal distribution in the cell shape factor $P/\sqrt{A}$ [62].

### 1.3.4 Phase-Field Model

The phase-field model is, fundamentally, an approach to constraining material in space, in which some solid or fluid material of interest is described by a density (phase) field $\phi$ and is assigned dynamics according to the problem in question. This technique has historically proven fruitful, for example, in the study of front propagation [63], fluid mechanics [64] and alloy crystallization [65].

In the multi-phase field model for epithelia, each cell is a fluid droplet described by a phase field $\phi$, which takes on a value 1 inside the cell and 0 outside. In a system of $N$ cells, there are $N$ phase fields: one for each cell [66]. The cells are endowed with passive dynamics to constrain their areas and to prevent overlap. In addition, the cells can be assigned arbitrary active forces, such as polar or dipolar forces [67, 68], as well as tentative descriptions of intercellular friction [27], in an effort to uncover the physics behind the collective behaviours of epithelia.

The multi-phase field model for epithelia has been augmented in several ways, for example to describe the nucleus inside each cell [69] or to include the effects of chemotaxis [70] and adherens junctions [67]. More generally, phase-field models have found other uses in the field of active matter. For example, a single phase

field can be used to localise a droplet of continuum active fluid [71] or, depending on the specifics of the model, multiple droplets in an active crystal [72].

There are certain disadvantages to the multi-phase field model. Firstly, it is computationally intensive. To define the value of a phase field at every lattice site inside and in the vicinity of a cell requires perhaps two orders of magnitude more degrees of freedom than the vertices of a polygon in the vertex model, and just as many more calculations during an update step. Therefore, a balance must be struck regarding the size of a cell in the model: too large a cell is computationally impractical to work with, while choosing too small a cell puts the smoothness of the phase field at risk. This computational overhead has been part of the motivation to develop sharp-interface models as the limit of the phase-field model when the width of the interface separating the interior from the exterior of a cell goes to zero. In addition, from a theoretical point of view it is unclear how to implement or interpret a line tension between pairs of cells, a feature that comes naturally to and is a fundamental feature of the vertex and Voronoi models.

In this Thesis, we use a multi-phase field model to describe epithelia. The multi-phase field model is ideal to describe epithelia for several reasons. The cells in this model have arbitrary shape, their interfaces are handled smoothly and naturally, and neighbour rearrangements also occur naturally. Finally, the multi-phase field model can be equipped with arbitrary physics, which permits rich possibilities to model the collective dynamics of epithelia. The precise details of the model we use are discussed in Chapter 2.

### 1.3.5 Active Nematohydrodynamics

This Thesis concerns collective behaviours in confluent epithelial monolayers. The models discussed so far describe individual cells that together form a layer, but the cells can be coarse-grained to develop a continuum theory. Epithelia exhibit orientational order without positional order, which is a property of a nematic [32, 38]. Also, like other systems with nematic order [16], epithelial monolayers and their constituent cells create dipolar stresses with head-tail symmetry that can point either

outwards or inwards [14]. Therefore, a confluent epithelial monolayer constitutes an *active nematic*, which is described by a theory titled *active nematohydrodynamics*.

Active nematohydrodynamics is a theory for fluids characterised by orientational order and dipolar stresses. The theory builds on the passive nematohydrodynamics elucidated in the latter half of the twentieth century [73, 74], by introducing a dipolar active stress, which constantly injects energy into the fluid [40]. Recent decades have seen investigation into the rich behaviour of active nematic fluids and active nematics has proven a fruitful paradigm to describe the properties of physical systems [6, 7].

### Order Parameter

To describe orientational order in a material such as a nematic, an order parameter is required that contains information about both the direction and the magnitude of the ordering. For instance, in a polar fluid, a vector $\mathbf{n}$ is sufficient to describe the local ordering of the constituent particles, as a vector has both a direction and a magnitude. However, such an approach is inadequate to describe a nematic, as the local orientation has head-tail symmetry and identifies $\mathbf{n}$ with $-\mathbf{n}$ for a local vector. The nematic order parameter is defined as

$$\mathbf{Q} = Q\left(\hat{\mathbf{n}} \otimes \hat{\mathbf{n}} - \frac{\mathbb{1}}{2}\right) = \frac{Q}{2}\begin{pmatrix} \cos(2\theta) & \sin(2\theta) \\ \sin(2\theta) & -\cos(2\theta) \end{pmatrix} \tag{1.5}$$

where $\hat{\mathbf{n}} = (\cos\theta, \sin\theta)$. The order parameter respects head-tail symmetry, and is both traceless and symmetric. It need not *a priori* be traceless, but choosing $\mathbf{Q}$ this way has the advantage of resulting in $\langle \mathbf{Q} \rangle = Q = 0$ locally when the nematogens are isotropic. The magnitude of ordering is extracted from $\mathbf{Q}$ as $\mathrm{Tr}(\mathbf{Q}^2) = Q^2/4$.

This notion of an orientational order parameter can be extended to liquid crystals of constituents with $p-$fold rotational symmetry. For these systems, an order parameter in two dimensions is written as $\mathbf{Q}_p \equiv Q_p[[\mathbf{n}^{\otimes p}]]$ where $[[\cdot]]$ denotes the traceless part and $\cdot^{\otimes p}$ denotes the tensor product of $p$ copies of a vector [75, 76]. Each order parameter $\mathbf{Q}_p$ then has two independent components: $(Q_p/2^{p-1})\cos(p\theta)$ and $(Q_p/2^{p-1})\sin(p\theta)$, just like the definition in Equation 1.5 for the nematic $\mathbf{Q}$.

**Ordering and Elastic Free Energy**

In many liquid crystalline materials, there is a transition to a nematic phase as the temperature of the material decreases or its concentration increases [73]. Phenomenologically, one writes a Landau free energy in two dimensions for the transition to nonzero $Q$ as [7, 73, 74]

$$\mathcal{F}_L = \mathcal{F}_0 + \frac{1}{2}A(T)\mathrm{Tr}(\mathbf{Q}^2) + \frac{1}{4}C(T)(\mathrm{Tr}(\mathbf{Q})^2)^2 \tag{1.6}$$

where the sign of $A$ changes at $T = T^*$ the nematic transition temperature so that $\mathcal{F}_L$ develops a double well profile. This term accounts for the free energy as a function of the orientational order but the theory requires, in addition, a contribution from variations in the orientational order. This is the elastic term, and a generic description of elasticity in three dimensions uses three constants to penalise variations in $\hat{\mathbf{n}}$ the local director [73] as

$$\mathcal{F}_{el} = \frac{1}{2}K_1(\nabla\cdot\hat{\mathbf{n}})^2 + \frac{1}{2}K_2(\hat{\mathbf{n}}\cdot\nabla\times\hat{\mathbf{n}})^2 + \frac{1}{2}K_3|\hat{\mathbf{n}}\times\nabla\times\hat{\mathbf{n}}|^2\,. \tag{1.7}$$

The three terms describe, respectively, splay, twist and bend deformations in the texture of $\hat{\mathbf{n}}$, which are illustrated in Figure 1.2. This formulation of the elastic free energy contains but does not require head-tail symmetry, and so is also an appropriate description for the elastic free energy of a polar fluid.

Twist deformations are forbidden in the plane, because the curl of $\hat{\mathbf{n}}$ is out of the plane and is therefore normal to $\hat{\mathbf{n}}$. However, writing the elastic free energy in three dimensions permits a simplifying step that is clearest in three dimensions, and equally valid in two. The three Frank coefficients are close to equal [73] and, in some cases, may actually be equal [74]. A simplifying assumption is then to take a one-constant approach, $K_1 = K_2 = K_3 = K$, as has been done in previous treatments of active nematics [32, 77]. Then the elastic free energy simplifies to

$$\mathcal{F}_{el} = \frac{1}{2}K\Big((\nabla\cdot\hat{\mathbf{n}})^2 + |\nabla\times\hat{\mathbf{n}}|^2\Big) \tag{1.8a}$$

$$= \frac{1}{2}K(\nabla\hat{\mathbf{n}})^2 \tag{1.8b}$$

where the second identity holds up to surface terms. In tensorial notation for a nematic, Equation 1.8b is equivalent to

$$\mathcal{F}_{el} = \frac{1}{2}K(\nabla\mathbf{Q})^2. \tag{1.9}$$

This contribution yields in concert with the Landau expression in Equation 1.6 the full nematohydrodynamic free energy

$$\mathcal{F}_Q = \mathcal{F}_L + \mathcal{F}_{el} = \mathcal{F}_0 + \frac{1}{2}A\,\mathrm{Tr}(\mathbf{Q}^2) + \frac{1}{4}C\,(\mathrm{Tr}(\mathbf{Q})^2)^2 + \frac{1}{2}K(\nabla\mathbf{Q})^2 \tag{1.10}$$

where $A$ and $C$ can be tuned to put the material in the nematic phase.

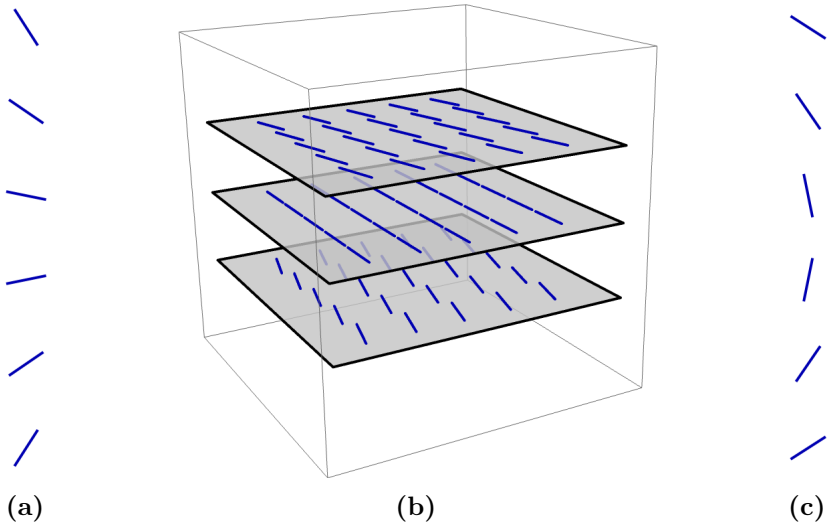


**Figure 1.2:** Schematic of (a) splay, (b) twist, and (c) bend configurations of a headless vector field corresponding in order to the terms in Equation 1.7. This field is the $\hat{\mathbf{n}}$ from which $\mathbf{Q}$ is constructed. Twist is forbidden in two dimensions.

### Topological Defects

Although in the plane, a uniform texture $\mathbf{Q}$ can minimise the free energy of Equation (1.10) given an appropriate choice of $A$ and $C$, nematic liquid crystals can display defects in the ordering. Moreover, in certain geometries such as spherical shells, it is forbidden to have a uniform director field. In both cases, the nematic gives rise to topological defects. These defects are points where $\mathbf{Q}$ is undefined, and $\mathbf{Q}$ is discontinuous on any contour that intersects these points. A nonzero winding

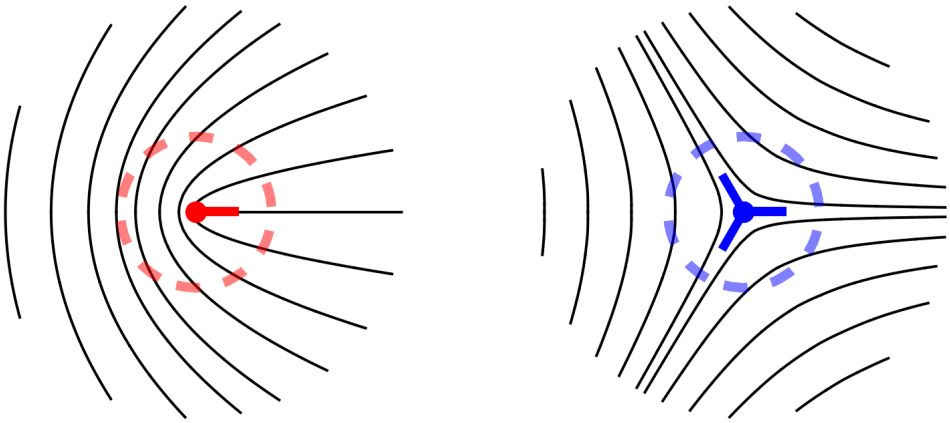

**(a)** **(b)**

**Figure 1.3:** Sketches of (a) $+1/2$ and (b) $-1/2$ topological defects in a nematic, which is represented by streamlines. The dashed curves represent contours along which the integral (1.11) is computed. Positively-charged $+1/2$ defects have a characteristic comet shape, while negatively-charged defects have a threefold-symmetric star shape.

number for the argument of the director around these points can be calculated. The winding numbers give rise to a charge given by

$$q \equiv \frac{1}{2\pi} \oint \mathrm{d}\theta \tag{1.11}$$

on a closed contour around the defect, where $\theta = \arctan(n_y, n_x) \in [-\pi/2, \pi/2)$ is the argument of the vector $\hat{\mathbf{n}}$ from which $\mathbf{Q}$ is constructed. The head-tail symmetry in a nematic permits half-integer charges $\pm 1/2$. In general, particles with $p-$fold rotational symmetry admit topological defects with charge $\pm 1/p$ [75, 76]. Topological defects with charge $+1/2$ have a characteristic comet-like shape, while negatively-charged defects have a threefold rotationally symmetric structure. Figure 1.3 illustrates topological defects with charge $\pm 1/2$, as well as representative contours along which to compute the integral in Equation (1.11). Topological defects are annealed out of passive nematics, but are created spontaneously in active nematics [7]. In addition, active plus-1/2 defects are self-propelled and can exhibit polar order [78].

### Nematohydrodynamic Equations

It remains to describe the dynamics of $\mathbf{Q}$ and its coupling to flow through the Navier-Stokes equations. Epithelial cells are characterised by small lengths and velocities [38], which means they exist at low Reynolds number and can be described by the Stokes equation.

The nematic order parameter $\mathbf{Q}$ is advected by the flow, aligns or tumbles with shear and vorticity according to a term $\mathbf{S}$, and relaxes towards equilibrium according to the traceless molecular field $\mathbf{H}$ [7]. In two dimensions, the dynamics is written as:

$$\partial_t \mathbf{Q} + \mathbf{u} \cdot \nabla \mathbf{Q} - \mathbf{S} = \Gamma \mathbf{H} \tag{1.12}$$

where

$$\mathbf{S} = \Big(\lambda \mathbf{E} + \mathbf{\Omega}\Big) \cdot \Big(\mathbf{Q} + \frac{\mathbb{1}}{2}\Big) + \Big(\mathbf{Q} + \frac{\mathbb{1}}{2}\Big) \cdot \Big(\lambda \mathbf{E} - \mathbf{\Omega}\Big) - 2\lambda \Big(\mathbf{Q} + \frac{\mathbb{1}}{2}\Big)\Big(\mathbf{Q} : \nabla \mathbf{u}\Big) \tag{1.13}$$

and

$$\mathbf{H} = -\frac{\delta \mathcal{F}}{\delta \mathbf{Q}} + \frac{\mathbb{1}}{2} \mathrm{Tr}\Big(\frac{\delta \mathcal{F}}{\delta \mathbf{Q}}\Big) \tag{1.14}$$

where $\mathbf{E}$ is the rate of strain tensor and $\mathbf{\Omega}$ is the vorticity tensor. The parameter $\lambda$ is called the *flow-tumbling parameter* and controls whether $\mathbf{Q}$ aligns with the flow ($\lambda > 0$, typical of rod-like particles) or tumbles in the flow ($\lambda > 0$, for disc-shaped particles). The Navier-Stokes equations for a constant-density fluid read

$$\nabla \cdot \mathbf{u} = 0 \tag{1.15}$$

$$\rho(\partial_t \mathbf{u} + \mathbf{u} \cdot \nabla \mathbf{u}) = \nabla \cdot \Pi \tag{1.16}$$

where $\rho$ is the fluid density and $\Pi$ is a stress tensor containing both passive and active terms. In the low-Reynolds number limit, the left-hand side of Equation (1.16) vanishes, yielding $\nabla \cdot \Pi = 0$. The stress tensor $\Pi$ contains viscous and elastic terms with viscosity $\eta$ and pressure $P$:

$$\Pi^{\mathrm{visc}} = 2\eta \mathbf{E} \tag{1.17}$$

$$\begin{aligned} \Pi^{\mathrm{elastic}} = -P\mathbb{1} + 2\lambda \Big(\mathbf{Q} + \frac{\mathbb{1}}{2}\Big)(\mathbf{Q} : \mathbf{H}) + \mathbf{Q} \cdot \mathbf{H} - \mathbf{H} \cdot \mathbf{Q} \\ - \lambda \mathbf{H} \cdot \Big(\mathbf{Q} + \frac{\mathbb{1}}{2}\Big) - \lambda \Big(\mathbf{Q} + \frac{\mathbb{1}}{2}\Big) \cdot \mathbf{H} - \nabla \mathbf{Q} \frac{\delta \mathcal{F}}{\delta \nabla \mathbf{Q}} \end{aligned} \tag{1.18}$$

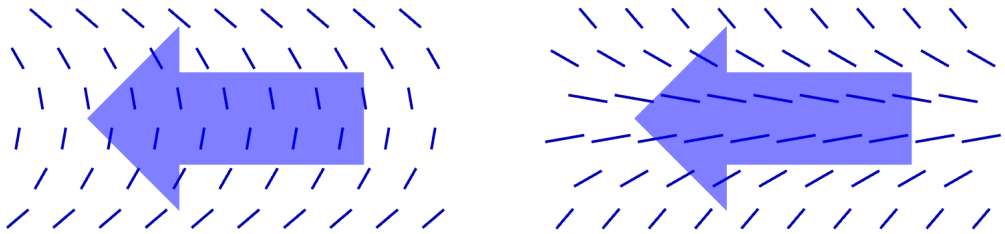


**Figure 1.4:** Cartoons of the $x$-component of the active force due to $\nabla \cdot \mathbf{Q}$ in (a) bend and (b) splay nematic textures. In both cases, the divergence of $\mathbf{Q}$ points to the left, so the active force for an extensile (contractile) nematic points to the right (left). Extensile nematics are unstable to bend and contractile to splay perturbations [40, 82].

Equations (1.12) to (1.18) describe passive nematohydrodynamics. The theory is modified to include active stresses, such as those exerted by motor proteins on crosslinked fibres in the cytoskeleton, or transduced between pairs of cells ad adherens junctions, or from a cell to a substrate *via* focal adhesions at both the front and the back of a cell [14]. These active stresses arise from force dipoles, pairs of forces in opposite directions aligned with the nematic director, which are averaged over to yield an active stress $\Pi^{\text{active}}$ of the form [40, 79, 80]

$$\Pi^{\text{active}} = -\zeta \mathbf{Q} \tag{1.19}$$

where $\zeta$ is the activity parameter that controls whether a cell pushes outwards ($\zeta > 0$, extensile) or pulls inward ($\zeta < 0$, contractile) along its dipolar director. In the passive limit, $\zeta = 0$. Both polar and nematic fluids equipped with the above active stress exhibit an instability corresponding to the sign of $\zeta$: extensile nematics are unstable to bend deformations, and contractile nematics are unstable to splay deformations [40, 81]. The divergence of $\mathbf{Q}$, in conjunction with the sign of $\zeta$, determines the direction of the active force in nematohydrodynamics [82]. Figure 1.4 shows a cartoon of $\nabla \cdot \mathbf{Q}$ for bend and splay configurations.

### Flows and Active Turbulence

A rich phenomenology of the instabilities of active nematics has been described, particularly in reference to extensile systems [83–85]. Active nematics exhibit several flow configurations according to the activity and geometry, and these flows are

paralleled in the collective behaviours of epithelia. In a bulk extensile nematic, ordered domains of size $\sim \sqrt{K/\zeta}$ form, which are connected by domain walls consisting of strong bend deformations. The domain walls relax by unbinding into topological defects with charge $\pm 1/2$, and the continuous unbinding of defects is characteristic of active nematics [83, 86]. While active $-1/2$ defects are immotile due to their rotational symmetry, the comet-shaped $+1/2$ defects self propel, towards either the head (extensile) or the tail (contractile).

The active length scale $\sqrt{K/\zeta}$ controls not only the size of ordered domains in the bulk, but also the behaviour of an active nematic in a channel *via* the activity number, the ratio $L\sqrt{\zeta/K}$ the channel width to the active length scale [87]. As the self-propulsion velocity of a $+1/2$ defect and the activity number grow, an active nematic transitions through several behaviours, from uniform or banded laminar flow to an oscillatory flow [88] to a highly vortical state characterised by $+1/2$ defects crossing paths in what is termed a 'Ceilidh dance' configuration, with hysteresis at the crossovers between laminar, oscillatory, and vortical flow [87, 89]. For channels that are yet larger, the system goes into 'active turbulence', a state characterised by short-range nematic order with chaotic flow and vorticity that results from the turnover of domain walls, hydrodynamic instabilities, and the creation and annihilation of defects [29, 80].

**Relationship to Epithelial Monolayers**

Epithelial monolayers have several properties that lend them to description by active nematohydrodynamics. A confluent monolayer is a collection of particles, which when coarse-grained can be described as a continuum fluid. In addition, force dipoles of several forms exist in epithelia: the contractile forces at focal adhesions in a single cell form pairs [14], while the crosslinked supracellular actomyosin cortex generates stresses both isotropic and anisotropic [17, 18]. The suppression of polar activity in confluent epithelia also permits dipolar properties of the monolayer to emerge [11, 14]. Epithelial monolayers can exhibit short-range nematic ordering along with spontaneous shear flow [38] and even oscillations and turbulence [29,

90]. Topological defects of both positive and negative charge are ubiquitous in epithelia and may even have biological function [32, 41].

Confluent epithelia and their collective properties, including flow and topological defects, have successfully been described by active nematohydrodynamics. The physical properties of confluent epithelia that hint at their active nematic nature, as well as the successful use of active nematohydrodynamics to model epithelia, motivate the use of an agent-based model coupled with principles of active nematics to investigate the physics of cell-cell interactions and to model the mesoscale behaviours of epithelial monolayers.

## 1.4 Thesis Outline

In this course of this Thesis, we use the multi-phase field model to investigate several collective behaviours of epithelia. First, in Chapter 2, we describe in detail the multi-phase field model, including the modelling of passive dynamics and active forces between cells, and then we consider various collective behaviours of epithelia monolayers. In Chapter 3, we consider the persistent rotational motion of pairs of confined cells when equipped with polar activity. Then we investigate microphase separation in a mixture of extensile and contractile cells in Chapter 4. Next, in Chapter 5, we characterise the fluidisation of an epithelial monolayer by fluctuations in cell-cell adhesion, in an extension to the foundational phase-field model. Finally, in Chapter 6, we examine a method of inducing flow in a channel by fixing cell orientations at the edge of the channel, and introduce viscosity to the multi-phase field model as an internal friction force, with an aim to reproduce shear viscosity as observed in experiment and in theory.

In all cases, the goal is to bridge the gap from an agent-based model of dipolar activity to continuum models under the hypothesis [13] that the bulk properties of epithelial monolayers are governed by dipolar active stresses.

*"One side of what? The other side of what?" thought Alice to herself.*

*"Of the mushroom," said the Caterpillar, just as if she had asked it aloud; and in another moment it was out of sight.*

*Alice remained looking thoughtfully at the mushroom for a minute, trying to make out which were the two sides of it; and, as it was perfectly round, she found this a very difficult question. However, at last she stretched her arms round it as far as they would go, and broke off a bit of the edge with each hand.*

*"And now which is which?" she said to herself...*

— Lewis Carroll [1]

# 2 Model

The phase-field model is a modelling technique that uses a density (phase) field $\phi(\mathbf{x}, t)$ to localise a fluid or other material in space and time. The dynamics are chosen to match the problem at hand and are, in principle, arbitrary. This approach has varied applications, such as to describe the propagation of a front [63], the dynamics of viscous flows [64], or the crystallization of an alloy out of a melt [65]. Phase-field models have been used also to describe active systems and processes, such as active crystallization [72], active droplets [91, 92] or single keratocytes [93, 94].

In this Chapter we formulate the multi-phase field model for epithelia, which describes each cell by an individual phase field, first implemented by Nonomura [66]. First we summarise the theory of the model and then discuss details of the numerics, which are based on a code written by Romain Mueller [68]. This Chapter provides a generic, albeit detailed, overview of the multi-phase field model, and variations on the model used will be described in the relevant Chapters.

## 2.1 Model Description

In this multi-phase-field model, there are $N$ phase fields $\phi_i(\mathbf{x}, t)$, each of which specifies the location of a single epithelial cell $i$. The value of the phase field indicates whether a particular location $\mathbf{x}$ at a particular time $t$ is inside or outside

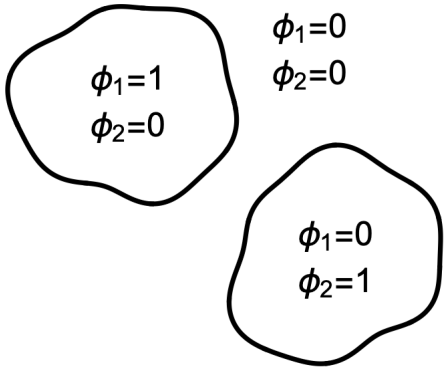


**Figure 2.1:** Cartoon of a pair of phase-field cells. The cells are indexed by $i$ and the phase fields $\phi_i$ take a value 1 inside cell $i$ and 0 outside cell $i$.

the cell. Inside a cell, its phase field takes a value 1, while outside the cell, its phase field takes a value 0. Figure 2.1 illustrates a pair of phase field cells and indicates where the phase fields take on values 0 and 1. In this Section, we write down the dynamics of the system, as well as the force balance that governs the dynamics. Next we detail the features of the model, starting first with the free energy functionals that govern the equilibrium properties of the cells. Finally, we detail the passive and active forces in the system, including the polar and dipolar forces we use to model the behaviour of epithelia.

### 2.1.1 Dynamics

Each phase field is advected by a velocity field, and is conserved up to a source term derived from the free energy in the system. The equation of motion is

$$\partial_t \phi_i + \mathbf{v}_i(\mathbf{x}, t) \cdot \nabla \phi_i = -J_0 \frac{\delta \mathcal{F}}{\delta \phi_i} \tag{2.1}$$

where the insertion of $J_0$ serves simply to rescale time for computational convenience. The phase field is in the overdamped regime, advected by active and passive force densities so that

$$\xi \mathbf{v}_i(\mathbf{x}, t) = \mathbf{f}_{\text{passive},i}(\mathbf{x}, t) + \mathbf{f}_{\text{active},i}(\mathbf{x}, t) \tag{2.2}$$

at every location $\mathbf{x}$. The passive force density is derived from the free energy functional $\mathcal{F}$:

$$\mathbf{f}_{\text{passive},i} = \frac{\delta \mathcal{F}}{\delta \phi_i} \nabla \phi_i \tag{2.3}$$

and it remains to define the free energy and any active forces of interest.

With the forces calculated, we are able to recalculate the velocity field (2.2) at each site before updating the order parameters of interest: each phase field, each structure tensor, and any directors and tensors associated with active forces and stresses.

### 2.1.2 Free Energy

The multi-phase field model uses several free energy functionals to cause each phase field to coalesce into a droplet with a particular size and to penalise the overlap of distinct droplets. The model can also be extended to include an adhesion energy that models the effect of adherens junctions between cells. There are Cahn-Hilliard and area conservation single-cell free energy functionals:

$$\mathcal{F}_{\text{CH}} = \sum_i \frac{\gamma}{\lambda} \int \mathrm{d}\mathbf{x} \left[ 4\phi_i^2 (1-\phi_i)^2 + \lambda^2 (\nabla \phi_i)^2 \right]; \tag{2.4a}$$

$$\mathcal{F}_{\text{A}} = \sum_i \mu \left[ 1 - \frac{1}{\pi R^2} \int \mathrm{d}\mathbf{x}\, \phi_i^2 \right]^2. \tag{2.4b}$$

The Cahn-Hilliard term $\mathcal{F}_{\text{CH}}$ is minimised by $\phi_i = 1$ and $\phi_i = 0$, and serves to separate the inside from the outside of a cell. However, these solutions are incompatible with the area conservation term, which is minimised when the cell area equals $\pi R^2$. The competition of the two terms therefore localises a region of $\phi_i = 1$ in a background of $\phi_i = 0$ that deviates minimally from the prescribed area $\pi R^2$ with a sufficiently small interface, where $\nabla \phi_i \neq 0$. The parameter $\lambda$ is the lengthscale of the interface, and when $\lambda \ll R\sqrt{\pi}$ the solution is approximated by the one-dimensional case [61]. In one dimension with boundary conditions $\lim_{x \to -\infty} \phi(x) = 0$ and $\lim_{x \to +\infty} \phi(x) = 1$, the function

$$\phi(x) = \frac{1}{2} + \frac{1}{2} \tanh\left( \frac{x - x_0}{\lambda} \right) \tag{2.5}$$

minimises the Cahn-Hilliard free energy, where $x_0$ is free. In two dimensions with $R \gg 1$, the hyperbolic tangent is a good approximation to the shape of the cell's interface. In the implementation of this model, however, we choose $\lambda = 2$ and $R = 8$, as listed in Table 2.1. The hyperbolic tangent approximation is therefore poor, but the lengthscale of the interface is still controlled by $\lambda$.

There are two time scales associated with the passive relaxation of a single cell: $\tau_{CH} = (\gamma h J_0)^{-1}$ and $\tau_A = (\mu J_0)^{-1}$, where $h$ is the lattice spacing. The area energy scale $\mu$ is typically much larger than the line tension $\gamma$ so that an individual cell relaxes on the timescale $\tau_{CH}$, which is $\mathcal{O}(10^2)$ timesteps for our parameters of choice, listed in Table 2.1. We identify the Cahn-Hilliard timescale as the key passive timescale in this model, $\tau_0 \equiv \tau_{CH}$.

There are two other free energy functionals, which describe pairwise interactions between phase-field cells. One term describes repulsion and the other adhesion:

$$\mathcal{F}_{\text{rep}} = \sum_i \sum_{j \neq i} \frac{\kappa}{\lambda} \int \mathrm{d}\mathbf{x}\, \phi_i^2 \phi_j^2; \tag{2.6a}$$

$$\mathcal{F}_{\text{adh}} = \sum_i \sum_{j \neq i} \omega\lambda \int \mathrm{d}\mathbf{x}\, \nabla\phi_i^2 \cdot \nabla\phi_j^2. \tag{2.6b}$$

These functionals resemble the first and second terms of the Cahn-Hilliard free energy, respectively. The parameters $\kappa$ and $\omega$ are additional line tensions that mediate a competition between repulsion and adhesion. The parameter $\kappa$ simply penalises overlap between phase field cells, while $\omega$ behaves as $-\gamma$ to promote the co-localisation of two phase-field interfaces. The adhesion free energy works as described because $\nabla\phi_i^2 \approx 0$ everywhere except on the cell membrane. Hence the quantity $\nabla\phi_i^2 \cdot \nabla\phi_j^2$ is only nonzero (in fact, is negative) where two cell membranes meet, and integrating that term over $\mathbf{x}$ gives the area of the junction between cells $i$ and $j$, which is the junction length times the cell interface length $\lambda$. Taking the gradient of $\phi_i^2$ and $\phi_j^2$ has the advantage that the right-hand side of the dynamics (2.1) is local, which is not the case for a free energy term $\sim \nabla\phi_i \cdot \nabla\phi_j$[1]. The longer

[1] Zhang et al. [67] write $\mathcal{F}_{\text{adh}} = \omega\lambda \sum_i \sum_{j \neq i} \int \mathrm{d}\mathbf{x}\, \nabla\phi_i \cdot \nabla\phi_j$. This expression has a functional derivative with respect to $\phi_i$ proportional to $\sum_{j \neq i} \int \mathrm{d}\mathbf{x}\, \nabla^2\phi_j$, which does not depend on $\phi_i$. Compare Camley et al. [95] who write a different adhesion energy density where the functional derivative with respect to $\phi_i$ is proportional to $\phi_i$ and therefore also local. These authors' adhesion term is in the form $\int \mathrm{d}\mathbf{x}\, |\nabla\phi_i|^2 \left|\nabla\phi_j\right|^2$.

the junctions between cells, the lower the adhesion free energy.

Walls are modelled by additional static phase fields $\phi_{\text{wall}}(\mathbf{x})$, one per wall, and interact with the cells as though they themselves are cells. These static phase fields are defined piecewise with a value of 1 'behind' the wall, and with an exponential profile

$$\phi_{\text{wall}}(\mathbf{x}) = \exp(-\lambda_{\text{wall}}\, r(\mathbf{x})) \tag{2.7}$$

inside the free part of the simulation domain, where $r(\mathbf{x})$ is the distance from a point inside the domain to the wall. The form of function $r(\mathbf{x})$ necessarily varies according to the shape and location of a wall. Walls interact with phase-field cells according to the free energy functionals

$$\mathcal{F}_{\text{rep, wall}} = \sum_i \sum_{j\neq i} \frac{\kappa_{\text{wall}}}{\lambda} \int \mathrm{d}\mathbf{x}\, \phi_i^2 \phi_{\text{wall}}^2; \tag{2.8a}$$

$$\mathcal{F}_{\text{adh, wall}} = 2 \sum_i \sum_{j\neq i} \omega_{\text{wall}}\, \lambda \int \mathrm{d}\mathbf{x}\, \nabla\phi_i \cdot \nabla\phi_{\text{wall}}. \tag{2.8b}$$

The most general statement of the free energy in the multi-phase field system, which appears in Equation (2.1), is then

$$\mathcal{F} = \mathcal{F}_{\text{CH}} + \mathcal{F}_{\text{A}} + \mathcal{F}_{\text{rep}} + \mathcal{F}_{\text{adh}} + \mathcal{F}_{\text{rep, wall}} + \mathcal{F}_{\text{adh, wall}}. \tag{2.9}$$

### 2.1.3 Passive Forces

The passive force density in the model is derived from the free energy $\mathcal{F}$ and is given by

$$\mathbf{f}_{\text{passive},i} = \frac{\delta\mathcal{F}}{\delta\phi_i}\nabla\phi_i. \tag{2.10}$$

To see why this is the case, we consider the change in free energy as the phase field $\phi_i$ is advected by a displacement $\delta\mathbf{x}$, illustrated in Figure 2.2. The phase field is transformed as

$$\phi_i(\mathbf{x}, t) \to \phi_i(\mathbf{x} - \delta\mathbf{x}, t) = \phi_i(\mathbf{x}, t) - \delta\mathbf{x} \cdot \nabla\phi_i(\mathbf{x}, t) + \mathcal{O}(\delta\mathbf{x}^2). \tag{2.11}$$

The work done by the phase-field system is

$$\mathcal{F}(\phi_i(\mathbf{x}, t)) - \mathcal{F}(\phi_i(\mathbf{x} - \delta\mathbf{x}, t)) \equiv -\int \mathrm{d}\mathbf{x}' \frac{\delta\mathcal{F}}{\delta\phi_i}\delta\phi_i \approx \int \mathrm{d}\mathbf{x}' \frac{\delta\mathcal{F}}{\delta\phi_i}\nabla\phi_i \cdot \delta\mathbf{x}, \tag{2.12}$$

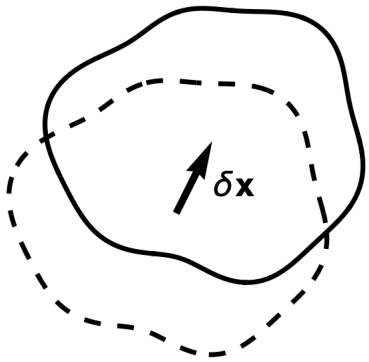


**Figure 2.2:** Cartoon of the advection of a phase field, which is transformed by a displacement $\delta\mathbf{x}$ as $\phi_i(\mathbf{x},t) \to \phi_i(\mathbf{x}-\delta\mathbf{x},t) = \phi_i(\mathbf{x},t) - \delta\mathbf{x}\cdot\nabla\phi_i(\mathbf{x},t) + \mathcal{O}(\delta\mathbf{x}^2)$. The change in free energy from before to after the displacement is equal to minus the work done by the system, which permits the passive force density to be written as $\mathbf{f}_{\text{passive},i} = \frac{\delta\mathcal{F}}{\delta\phi_i}\nabla\phi_i$.

but work is exactly an integral over space of the dot product of a force density with the displacement: therefore the passive force density is identified with the $(\delta\mathcal{F}/\delta\phi_i)\nabla\phi_i$ term.

### 2.1.4 Shape Tensor

The shape tensor is a quantity used to measure the orientation and deformation of a phase-field cell. The gradient of a phase field provides information about the cell interface according to $\nabla\phi_i(\mathbf{x}) = |\nabla\phi_i(\mathbf{x})|\,(\cos\theta(\mathbf{x}), \sin\theta(\mathbf{x}))$ with a direction and magnitude everywhere in space $\mathbf{x}$. A tensorial order parameter can be calculated at each site from that vector as [96]

$$\nabla\phi_i \otimes \nabla\phi_i - \frac{1}{2}\mathrm{Tr}(\nabla\phi_i \otimes \nabla\phi_i) = |\nabla\phi_i|^2 \begin{pmatrix} \cos(2\theta) & \sin(2\theta) \\ \sin(2\theta) & -\cos(2\theta) \end{pmatrix}. \tag{2.13}$$

These contributions are integrated over space to find a total orientation (and magnitude) for a cell — with the caveat that for a thin rodlike nematogen, $\nabla\phi_i$ is normal to the director almost everywhere. Observing that a change of sign in

the above equation takes $\theta$ to $\theta + \pi/2$, we define

$$\mathcal{D}_i = -\int \mathrm{d}\mathbf{x} \left( \nabla\phi_i \otimes \nabla\phi_i - \frac{1}{2}\mathrm{Tr}(\nabla\phi_i \otimes \nabla\phi_i) \right) \tag{2.14a}$$

$$= \begin{pmatrix} \mathcal{D}_{xx} & \mathcal{D}_{xy} \\ \mathcal{D}_{xy} & -\mathcal{D}_{xx} \end{pmatrix} \tag{2.14b}$$

$$= \frac{1}{2}\sqrt{\mathcal{D}_{xx}^2 + \mathcal{D}_{xy}^2}(\hat{\mathbf{d}}_{\parallel i} \otimes \hat{\mathbf{d}}_{\parallel i} - \frac{1}{2}\mathbb{1}). \tag{2.14c}$$

The orthonormal vectors $\hat{\mathbf{d}}_{\parallel i} = (\cos\theta_i, \sin\theta_i)$ and $\hat{\mathbf{d}}_{\perp i} = (-\sin\theta_i, \cos\theta_i)$ are defined, where $\theta$ is given by $\tan(2\theta) = \mathcal{D}_{xy}/\mathcal{D}_{xx}$. These are eigenvectors of $\mathcal{D}_i$ with eigenvalues $\pm\frac{1}{2}\sqrt{\mathcal{D}_{xx}^2 + \mathcal{D}_{xy}^2}$, respectively. The unit vector $\hat{\mathbf{d}}_{\parallel i}$, corresponding to the largest eigenvalue, is termed the *shape director*, and finds use not only in quantifying the shapes of the cells but also in aligning the directors that define active forces in the phase-field system.

### 2.1.5 Active Forces

There is substantial freedom in how we define the active forces in the system. In this Thesis we consider polar and dipolar forces. The description of the latter borrows substantially from its treatment in active nematohydrodynamics. Here we describe both polar and dipolar active forces and comment on the choice that exists in defining their directions.

#### Polar Active Forces

A polar force density, acting everywhere, on cell $i$ can be written as

$$\mathbf{f}_{\mathrm{polar},i}(\mathbf{x}, t) = \alpha_i \phi_i(\mathbf{x}, t)\mathbf{p}_i. \tag{2.15}$$

The vector $\mathbf{p}_i$ is the polarisation that dictates the direction of the active polar force, the scalar $\alpha_i$ controls the polar activity, and scaling the force density by the phase field localises the polar force to the phase-field cell itself. There are many choices to set the dynamics of $\mathbf{p}_i$, and different choices have been taken by various authors to implement, for instance, Brownian motion, alignment to

neighbour polarisations, or to the cell velocity [67, 97, 98]. The polarisation can be assigned relaxational dynamics given by

$$\frac{\mathrm{d}\mathbf{p}_i}{\mathrm{d}t} = -J_p(\mathbf{p}_i - \hat{\mathbf{u}}). \tag{2.16}$$

where $\hat{\mathbf{u}}$ is a unit vector of choice. This vector could be, for instance, a cell's normalised centre-of-mass velocity $\mathbf{v}_{COM,i}/\left|\mathbf{v}_{COM,i}\right|$ or shape director $\hat{\mathbf{d}}_{\|i}$. Several methods of aligning polarisation to velocity result in a flocking transition [67, 98] akin to that of the Toner-Tu continuum model [99]. Note the dynamics of $\mathbf{p}_i$ in Equation (2.16) do not conserve $|\mathbf{p}_i|^2$.

**Dipolar Active Forces**

Like polar forces, dipolar active forces are defined by a magnitude and a direction. Given a director $\mathbf{n}_i$ for cell $i$, a nematic tensor for cell $i$ is defined by

$$\mathbf{Q}_i = \mathbf{n}_i \otimes \mathbf{n}_i - \frac{1}{2}|\mathbf{n}_i|^2 \mathbb{1}_2. \tag{2.17}$$

In line with the definition of polar forces, this director has some dynamics

$$\frac{\mathrm{d}\mathbf{n}_i}{\mathrm{d}t} = -J_n(\mathbf{n}_i - \hat{\mathbf{u}}) \tag{2.18}$$

so that $\mathbf{n}_i$ relaxes towards a unit vector $\mathbf{u}$ of choice, with timescale $J_n^{-1}$. Choices include, but are not limited to, the normalised centre of mass velocity $\mathbf{v}_{COM,i}/\left|\mathbf{v}_{COM,i}\right|$ and the shape director $\hat{\mathbf{d}}_{\|i}$.

Where each cell has a dipolar activity $\zeta_i$, a global stress field can be written as

$$\sigma(\mathbf{x}, t) = -\sum_i \zeta_i \mathbf{Q}_i \phi_i(\mathbf{x}, t), \tag{2.19}$$

which is analogous to the active stress $\Pi^{\text{active}} = -\zeta\mathbf{Q}$ of active nematohydrodynamics. Additionally, we distinguish self-induced active stresses from those exerted by neighbours, and set different activities $\zeta_{\text{self}}$ and $\zeta_{\text{inter}}$ to further qualify the two classes of stress [100]. Self- and neighbour-induced dipolar stresses originate in different biophysical mechanisms: while both rely on the actomyosin cortex, $\zeta_{\text{self}}$ corresponds to contractility and junctions between an individual cell's plasma

membrane and its own cytoskeleton [101], while $\zeta_{\text{inter}}$ corresponds to contractility in the entire supracellular actomyosin network, which is mediated by cadherin proteins at adherens junctions [13, 14, 21]. Consequently we write force densities

$$\mathbf{f}_{\text{self},i} = -\zeta_{\text{self},i}\mathbf{Q}_i \cdot \nabla\phi_i; \tag{2.20a}$$

$$\mathbf{f}_{\text{inter},i} = -\sum_{j\neq i} \zeta_{\text{inter},j}\mathbf{Q}_j \cdot \nabla\phi_j; \tag{2.20b}$$

$$\mathbf{f}_{\text{dipolar},i} = \mathbf{f}_{\text{self},i} + \mathbf{f}_{\text{inter},i}. \tag{2.20c}$$

## 2.2 Model Implementation

The multi-phase field model has been described in Section 2.1. This Section considers the implementation of the model in the open-source software CELADRO created by Romain Mueller [68] and since developed and improved [102]. There are helper subroutines and numerical tricks to improve performance and enable parallelisation with CUDA.

### 2.2.1 Lattice

The model is solved on a square lattice with spacing $h$. Coordinates $\mathbf{x}$ thereby have discrete indices $\mathbf{x}(k)$. Derivatives and integrals are discretised, with first derivatives derivatives given by the symmetric formulae

$$\frac{\mathrm{d}f}{\mathrm{d}x} = \frac{f(x+h,y) - f(x-h,y)}{2h}, \tag{2.21a}$$

$$\frac{\mathrm{d}f}{\mathrm{d}y} = \frac{f(x,y+h) - f(x,y-h)}{2h}, \tag{2.21b}$$

and a two-dimensional five-point-stencil discrete Laplace operator:

$$\nabla^2 f = \frac{f(x+h,y) + f(x-h,y) + f(x,y+h) + f(x,y-h) - 4f(x,y)}{h^2}. \tag{2.22}$$

Integrals become sums according to

$$\int \mathrm{d}\mathbf{x}\, f(\mathbf{x}) = h^2 \sum_k f(\mathbf{x}(k)). \tag{2.23}$$

The lattice spacing is set to $h = 1$.

The lattice is implemented with periodic boundary conditions. To simulate a monolayer in confinement, phase fields representing walls are created that interact passively with the cells so as to constrain them to, for instance, a box, a channel, or an ellipse.

### 2.2.2 Patch

As observed in Subsection 2.1.2, the value of the phase field decays asymptotically from 1 to 0 on a lengthscale set by the parameter $\lambda$. Sufficiently far away from the centre of mass of the phase field, the field's value is so small that it can be treated as zero. Therefore, it is necessary to solve the dynamics in Equation (2.1) only on a small subset of the domain, a square that we term a 'patch', the size of which is a programme option. In this way, the time complexity of the phase-field model is constant in the size of the domain, which can represent a substantial speedup on large domains with many phase-field cells.

Every lattice site on the domain is assigned a unique index $k$, in the interval $[0, L_x \times L_y)$, calculated as

$$k(x, y) = y + L_y x. \tag{2.24}$$

Coordinates $(x, y)$ can be calculated as the integer part and remainder of $k/L_y$, respectively. Equivalently, every lattice site in the patch belonging to a cell $n$ is assigned a unique $q_n$, using information about the location of the patch. The algorithm stores the coordinates of the top-left corner of the patch belonging to each phase field. Given coordinates $(x, y)$, the algorithm calculates using periodic boundary conditions the corresponding coordinates $(x^*, y^*)$ relative to the top-left corner of the patch, with $x^* \in [0, L_x)$ and $y^* \in [0, L_y)$. If either $x^*$ or $y^*$ is greater than $L_{\text{patch}}$, then the coordinates are outside the patch and not assigned a value $q_n$. Otherwise, the patch index is calculated similarly to the global index:

$$q_n(x^*, y^*) = y^* + L_{\text{patch}} x^*. \tag{2.25}$$

This procedure is naturally invertible, so that coordinates $(x, y)$ can be calculated from a pair $(n, q_n)$ and indeed it is possible, given a pair $(n, q_n)$, to find the $q_k$ for

cell $k$ so that $(n, q_n)$ and $(k, q_k)$ have the same coordinates. This feature is critical to the implementation of cell-cell friction in Chapter 6.

At the end of each update, the location of each patch is updated so that it is centred on its respective phase field. In this implementation of the model, with $R = 8$ generically, the patch is a square of side length 49 lattice units, containing $N_{\text{patch}} = 49 \times 49$ sites.

### 2.2.3 Algorithm: Initialisation

When the software CELADRO is run, an instance of the `Model` class is created and populated with model parameters.

A pre-run computation is completed, during which any active forces are turned off and the cells are relaxed as though they were passive, to generate an initial condition for the simulation with full-size cells. The cells are stored as an array of arrays `phi`, where `phi[i]` is an array of $L^2_{\text{patch}}$ entries that stores data for phase field $\phi_i$. The simulation domain is populated by phase fields with radius $r = R/2$ that are later allowed to grow to full size. The centres of the phase fields can be chosen in several ways: for instance, they can be read in from an initial configuration file, calculated to form a hexagonal close-pack, or chosen randomly. If chosen randomly, the cells' centres are chosen to be no closer than $0.9R$ in any direction, so that the cells do not overlap.

### 2.2.4 Algorithm: Update

The unit of time in CELADRO is 1. However, each unit of time is subdivided into `nsubsteps` substeps, for a timestep $\delta t = 1/$`nsubsteps`, and the calculation is refined for each of `npc` predictor-corrector steps. For each predictor-corrector step within each substep, for each timestep, the model is updated. Schematically, the update is calculated as

```
UpdateSumsAtNode()
UpdatePotAtNode()
UpdateNeighbourCells()
```

`UpdateForcesAtNode()`

`UpdatePhaseFieldAtNode()`

`UpdateStructureTensorAtNode()`
`UpdatePolarization()`
`UpdateNematic()`
`UpdatePatch()`

All functions titled using `AtNode`, as well as `UpdateNeighbourCells()`, are parallelised over phase fields and lattice sites, using the correspondence between global site index $k$ and local site index $q_n$. The method `UpdateStructureTensorAtNode()` calculates the shape tensor as described in 2.1.4. The polarisation and nematic directors are updated according to 2.1.5, and the patch is updated as outlined in 2.2.2.

**Sums**

For the sake of numerical efficiency, several sums are calculated before any updates to the multiple phase fields are made. These sums are parallelised over global lattice sites $k$. These are:

$$\sum_i \phi_i(\mathbf{x}, t); \tag{2.26a}$$

$$\sum_i \phi_i^2(\mathbf{x}, t); \tag{2.26b}$$

$$\sum_i \zeta_i \mathbf{Q}_i \phi_i(\mathbf{x}, t); \tag{2.26c}$$

$$\int \mathrm{d}\mathbf{x}\, \phi_i^2(\mathbf{x}, t). \tag{2.26d}$$

Once these sums are calculated for every lattice site, subsequent updates to calculate, for instance, free energies and active forces can be parallelised over patch sites belonging to individual cells. These sums over all cells assist in calculating numerous terms involving sums over cells $j \neq i$. For example,

$$\sum_{j \neq i} \phi_j^2(\mathbf{x}, t) = -\phi_i^2(\mathbf{x}, t) + \sum_i \phi_i^2(\mathbf{x}, t). \tag{2.27}$$

### Functional Derivatives

The function `UpdatePotAtNode()` updates the functional derivatives of the free energy $\delta\mathcal{F}/\delta\phi_i$ for all phase fields $i$. These functional derivatives are used to calculate the passive forces as well as the relaxation term on the right-hand side of Equation (2.1). The functional derivatives of the free energy terms listed in Equations (2.4) and (2.6) are calculated using integration by parts when necessary and listed below as

$$\frac{\delta\mathcal{F}_{\mathrm{CH}}}{\delta\phi_i} = \frac{\gamma}{\lambda}\int \mathrm{d}\mathbf{x}\,\left[8\phi_i(1-\phi_i)(1-2\phi_i) - 2\lambda^2\nabla^2\phi_i\right]; \tag{2.28a}$$

$$\frac{\delta\mathcal{F}_{A}}{\delta\phi_i} = \frac{4\mu}{\pi R^2}\int \mathrm{d}\mathbf{x}\,\phi_i\left[1 - \frac{1}{\pi R^2}\int \mathrm{d}\mathbf{x}\,\phi_i^2\right]; \tag{2.28b}$$

$$\frac{\delta\mathcal{F}_{\mathrm{rep}}}{\delta\phi_i} = \frac{4\kappa}{\lambda}\sum_{j\neq i}\int \mathrm{d}\mathbf{x}\,\phi_i\phi_j^2; \tag{2.28c}$$

$$\frac{\delta\mathcal{F}_{\mathrm{adh}}}{\delta\phi_i} = -4\omega\lambda\sum_{j\neq i}\int \mathrm{d}\mathbf{x}\phi_i\nabla^2\phi_j. \tag{2.28d}$$

The functional derivatives of the free energy functionals listed in Equations 2.8 for interactions with walls are given by

$$\frac{\delta\mathcal{F}_{\mathrm{rep}}}{\delta\phi_i} = \frac{2\kappa_{\mathrm{wall}}}{\lambda}\sum_{j\neq i}\int \mathrm{d}\mathbf{x}\,\phi_i\phi_{\mathrm{wall}}^2; \tag{2.29a}$$

$$\frac{\delta\mathcal{F}_{\mathrm{adh}}}{\delta\phi_i} = -2\omega_{\mathrm{wall}}\,\lambda\sum_{j\neq i}\int \mathrm{d}\mathbf{x}\nabla^2\phi_{\mathrm{wall}}. \tag{2.29b}$$

### Neighbour Cells

Every cell $i$ has a set of neighbours $N_i(t)$ that evolves in time. At every time $t$, the value of each other cell $j$ is checked at every lattice site belonging to cell $i$. If both $\phi_i$ and $\phi_j$ exceed a threshold 0.2, then cells $i$ and $j$ are considered neighbours, so that $i \in N_j(t)$ and $j \in N_i(t)$. Since the interior of cell $i$ is considered to be where $\phi_i \approx 1$, and the membrane of a cell corresponds to $\phi_i \approx 0.5$, choosing a threshold 0.2 ensures that only cells, which are close together, are called neighbours, and that there are no mistaken next-nearest pairs identified as neighbours.

### Forces

Forces are calculated as outlined in Section 2.1. Furthermore, the `UpdateForcesAtNode()` method calculates the velocity fields $\mathbf{v}_i(\mathbf{x}, t)$ according to the force balance in Equation (2.2) so they are ready to be used to calculate the phase-field update.

### Phase Field Update

The passive forces come from $\mathbf{f}_{\text{passive},i} = \frac{\delta \mathcal{F}}{\delta \phi_i} \nabla \phi_i$, where we take advantage of integration by parts in the Cahn-Hilliard and adhesion terms. For each site, we compute quantities such as $\sum_i \phi_i^n$ for $n \in \{1, \ldots, 4\}$ as these are required to calculate contributions to the molecular field and the active force density. In the code, to avoid computing $\sum_{j \neq i} a_j$ for a number of quantities, we calculate instead $-a_i + \sum_j a_j$.

We must integrate the equation of motion

$$\partial_t \phi_i = -\mathbf{v}_i(\mathbf{x}, t) \cdot \nabla \phi_i - J_0 \frac{\delta \mathcal{F}}{\delta \phi_i} \tag{2.30}$$

where several choices are free: the formulation of the free energy, the modelling of active forces, and the calculation of the velocity field $\mathbf{v}_i(\mathbf{x}, t)$ in either the dry or the wet regime. We solve the PDE on a cell's patch, which is a square subset of the computational domain. We assume that a cell's phase field is identically zero outside its patch; the patch's size relies on our choice of parameters, and setting the patch too small can cause numerical problems.

The method of iterating in time is through a one-step predictor-corrector process with timestep $\delta t$, first proposing and then refining an update:

$$\delta \phi_i^{(k+1)} = -\mathbf{v}_i^{(k)}(\mathbf{x}, t) \cdot \nabla \phi_i^{(k)} - J_0 \frac{\delta \mathcal{F}}{\delta \phi_i^{(k)}} \tag{2.31a}$$

$$\phi_i^{(k+1)}(t + \delta t) = \phi_i^{(0)}(t) + \frac{1}{2} \delta t (\delta \phi_i^{(0)} + \delta \phi_i^{(k+1)}) \tag{2.31b}$$

with $\phi_i^{(0)} = \phi_i(\mathbf{x}, t)$. Typically, five predictor-corrector steps are used. The location of the patch is updated after each predictor-corrector step to ensure the centre of mass of the cell is to within rounding error in the centre of the patch.

### 2.2.5 Numerical Stability

Although the forward Euler scheme described in 2.2.4 is not particularly sophisticated, it is suitable for solving the multi-phase field model. However, care must be taken that large gradients of the free energy and large forces, both active and passive, do not cause an exponential numerical divergence.

To that end, we must choose a sufficiently small timestep and a sufficiently small coefficient $J_0 \lesssim 10^{-1}$. The unit of time is always 1, and it is subdivided into at least five smaller timesteps. For active systems with large activity, i.e. $\alpha \gtrsim 1.0$ or $|\zeta| \gtrsim 1.0$, the number of substeps may be as large as 50.

Finally, the relatively coarse lattice spacing relative to the lengthscale of the phase-field interface ($\lambda = 2$) could result in large gradients and Laplacians. We use a function to suppress large Laplacians:

$$f(x) = \frac{x}{\sqrt{1+x^2}}. \tag{2.32}$$

This function remains within $\sim 10\%$ of the identity for $x \in [-1/2, 1/2]$ and saturates at $\pm 1$. The phase-field cells in this model have interfaces approximately equal to hyperbolic tangents with lengthscale 2. The magnitude of the Laplacian of such a phase-field profile is $\sim 10^{-1}$. We can be confident that the implementation of the suppression does not substantially alter the model, since the Laplacians in the system are typically small, and serves only to preserve the numerical stability of the Euler scheme.

### 2.2.6 Cell Area and Packing Fraction

It is only easy to define the packing fraction of hard particles. The packing fraction of soft particles is not uniquely defined, so we choose to measure an approximate area fraction of cells. To approximate the area of a single cell we use

$$A_i \approx \int \mathrm{d}\mathbf{x}\, \phi_i^2 \tag{2.33}$$

and this is the calculation used in the area free energy functional Equation 2.4b. This calculation is used instead of some other expression such as $\int \mathrm{d}\mathbf{x}\, |\phi_i|$ or

$\int \mathrm{d}\mathbf{x}\,\Theta(\phi_i - \phi^*)$ with some threshold $\phi^*$ because, among positive-definite quantities to associate with area, the latter do not have continuous functional derivatives. There is a caveat to this calculation, in that we identify the contour $\phi_i = 0.5$ as setting the boundary of the cell, but the phase-field naturally (except in the limit $\lambda \to 0$) extends past this level curve. Nevertheless, we define the packing fraction as

$$\Phi = \sum_i A_i / A_D \tag{2.34}$$

where $A_D$ is the area of the domain available to the cells, which accounts features such as confinement. In modelling confluent layers, we choose a number density of cells such that $\Phi > 0.8$.

### 2.2.7 Data

Raw data from CELADRO are written to file at intervals given by the parameter `ninfo`, which ranges from 100 to 1000 timesteps. From these data, we compute observables of interest including, but not limited to, mean velocity, cluster size, and mean square displacement. These calculations are run using the Pandas package for Python, and data are visualised using the Matplotlib and Seaborn packages.

### 2.2.8 Parameters

We generally use $\gamma = 1.4$, $\lambda = 2.0$, $\mu = 120$ and $\kappa = 1.5$. The adhesion line energy $\omega$ is used as a control parameter in Chapter 3 and is neglected in Chapter 4. The coefficient of friction in the substrate force balance is chosen as $\xi = 3.0$ and the target cell radius is $R = 8.0$. Relaxation according to the free energy is controlled by the parameter $J_0 = 5 \times 10^{-3}$ and each cell's nematic director relaxes with rate $J_n = 0.1$. The unit of time is 1. Each step was divided into five substeps and there are `npc` $= 5$ predictor-corrector steps per substep.

Parameters of interest in the model include the magnitude $\alpha_i$ of any polar activity, the magnitudes $\zeta_{\mathrm{self},i}$ and $\zeta_{\mathrm{inter},i}$ of autologous and neighbour-neighbour dipolar stresses. The parameter $\omega$ mediating the adhesion interaction is promoted to a dynamical (random) variable in Chapter 5. Although the substrate coefficient

| Parameter | Value | Dimensions | Equation |
|---|---|---|---|
| $J_0$ | $5 \times 10^{-3}$ | 1/(Energy×Time) | (2.1) |
| $J_p$ | 0.1 | 1/Time | (2.16) |
| $J_n$ | 0.1 | 1/Time | (2.18) |
| $\xi$ | 3.0 | Energy×Time/Length$^2$ | (2.2) |
| $\gamma$ | 1.4 | Energy/Length | (2.4a) |
| $\lambda$ | 2.0 | Length | (2.4a) |
| $\mu$ | 120 | Energy | (2.4b) |
| $\kappa$ | 1.5 | Energy/Length | (2.6a) |
| $\omega$ | 0.4 | Energy/Length | (2.6b) |
| $\lambda_{\text{wall}}$ | 3.0 | Length | (2.7) |
| $\kappa_{\text{wall}}$ | 4.0 | Energy/Length | (2.8a) |
| $\omega_{\text{wall}}$ | 0.0 | Energy/Length | (2.8b) |
| $h$ | 1 | Length | (2.21),(2.22),(2.23) |
| $\delta t$ | 1/`nsubsteps` | Time | (2.31b) |
| `nsubsteps` | 5 | 1 | (2.31b) |
| `npc` | 5 | 1 | (2.31) |

**Table 2.1:** Parameters used in the multi-phase field model. The substrate friction coefficient $\xi$ and the adhesion interface tension $\omega$ are occasionally treated as control parameters.

$\xi$ is not used as a control parameter, the implications of modifying it are discussed in the second half of Chapter 6.

*"Now here, you see, it takes all the running you can do, to keep in the same place. If you want to get somewhere else, you must run at least twice as fast as that!"*

— Lewis Carroll [2]

# 3 Persistent Rotational Motion in Confinement

## 3.1 Introduction

Rotational motion is a ubiquitous collective behaviour of epithelial cells. These cells organise into monolayers [12] and adhere to each other at adherens junctions mediated by cadherin proteins, and to extra-cellular matrix (ECM) at focal adhesions mediated by integrin proteins [13, 14, 19, 21]. Adherens junctions connect to an internal cytoskeleton composed of microtubules and the actomyosin cortex, which distributes stresses across the entire cell layer [13]. Active stresses in epithelia can be polar for small groups and individual cells [13, 19] or dipolar in large collectives, as lamellipodia are suppressed [11, 14].

The collective rotation that can emerge from these cell-cell interactions and active stresses in the epithelium exists across a range of lengthscales. Groups of cells have been observed to rotate in vitro in sizes ranging from just pairs [34, 35] to almost ten [36] or several tens [37]. The monolayers break chiral symmetry to rotate clockwise or anticlockwise on a fibronectin substrate, which is designed to accommodate anywhere from 2 to $10^2$ cells. In these experiments, the fibronectin pattern is entirely covered by epithelial cells, so that the systems can be described as confluent.

Pairs of bovine endothelial cells plated on fibronectin micropatterns 20$\mu$m to 50$\mu$m in diameter deformed into a Yin-Yang pattern and rotated either clockwise or anticlockwise with no preference for one direction over the other. On the other hand, pairs of mouse fibroblasts similarly prepared failed to rotate collectively [35]. These behaviours were described by a one-dimensional model with control parameters representing the persistence of a single cell's random walk and a coupling, a measure of how strongly a cell tends to move in the same direction as its neighbour. Fibroblasts' smaller persistence time while performing a random walk is cited as the reason for their failure to rotate on the micropattern. The origin of the dynamic coupling is left unspecified but may be related to contact following of locomotion, as in the front-rear polarisation trains in [33]. The persistence-dynamic coupling model reproduces the Yin-Yang rotation behaviour and is susceptible to external perturbations that reverse the direction of rotation, or set randomly-moving cells into a coherent rotational state.

Doxzen et al. plated MDCK cells on much larger circular patterns, with diameters in the hundreds of $\mu$m [37]. Subconfluent populations were allowed to divide into confluent and, subsequently, over-confluent monolayers. An order parameter characterising rotational motion was defined, and the subconfluent layers were found not to rotate. In contrast, both the confluent and over-confluent monolayers rotated persistently, although the latter displayed a smaller velocity and mean order parameter than the former, with a larger spread.

The diameter of the circular pattern was varied and the spatial velocity correlation function was calculated. For small patterns (i.e. those with diameters 100$\mu$m and 200$\mu$m) the velocity correlation was consistent with that of a solid rotating disc, while larger patterns (diameters 500$\mu$m and 1000$\mu$m) showed a correlation length of 170$\mu$m, so that the monolayer did not rotate collectively. This correlation length in confinement was roughly the same size as in the unconfined epithelial monolayer, an upper limit on the size of vortices [37]. This behaviour was reproduced using a Cellular Potts Model, and further experiments showed that the clusters

rotated only transiently, changing direction, when intercellular force transmission was downregulated. This suggests that cell-cell adhesion

The persistent rotation of pairs of cells on square micropatterns has been studied numerically as a testbed for the investigation of mechanisms of cell polarisation [95]. A phase-field model described the cytoplasm and nucleus of each cell, and polarisation was modelled using a reaction-diffusion system representing a Rho GTPase, which promotes actin polymerisation, and an inhibitor. Two inhibition mechanisms were also investigated: a CIL algorithm in which contact anywhere on the cell generated GTPase inhibitor was found to suppress rotational motion. A front-front inhibition mechanism, where contact with only the front of a neighbouring cell generated the inhibitor, allowed rotation to take place, but the behaviour was found not to be persistent.

Camley et al. found that a Vicsek-type alignment [103] of each cell's polarisation to the mean of its neighbours' velocities failed to reproduce persistent rotational motion (PRM). However, a polarisation mechanism that relaxed each cell's polarisation towards its own velocity did result in PRM [95]. Zhang et al. obtained a similar result in a bulk epithelium, where a sufficiently strong noisy polarisation aligned towards each cell's velocity resulted in an unjamming transition. As polar activity is tuned, the layer transitions from a jammed state to a liquid phase, and then to flocking liquid and solid phases that migrate in a single direction [67]. Zhang et al. also found a liquid phase when the polarisation aligns to the long axis of the cell.

The unjamming transition is a characteristic feature of polar activity [14], and a lack of persistence in a random walk has been implicated in a tendency to jam [35]. In addition, cell-cell adhesion has been suggested to promote persistent rotational motion in epithelial sheets [37]. These results therefore motivate the study of the interplay of adhesion, polar activity, and noise in the context of persistent rotational motion. In this Chapter we implement a multi-phase field model for epithelia equipped with cell-cell adhesion and noisy polar active forces and analyse the behavioural states that emerge.

## 3.2 Model

The multi-phase field model used in this Chapter substantially follows the description detailed in Chapter 2. The key differences are in the description of the cell-cell adhesion and the dynamics of the polar force. The free energy functional that models cell-cell adhesion *via* adherens junctions is

$$\mathcal{F}_{\text{adh}} = \sum_i \sum_{j \neq i} \omega\lambda \int \mathrm{d}\mathbf{x}\, \nabla\phi_i \cdot \nabla\phi_j \tag{3.1}$$

following Zhang et al. [67]. This description of the adhesion differs from that in Equation (2.6b) by the use here of the gradients of the phase fields, rather than the gradients of their *squares*. This modified free energy can be rewritten up to a surface term as

$$\mathcal{F}_{\text{adh}} = -\sum_i \sum_{j \neq i} \omega\lambda \int \mathrm{d}\mathbf{x}\, \phi_i \nabla^2\phi_j \tag{3.2}$$

and has functional derivative

$$\frac{\delta\mathcal{F}_{\text{adh}}}{\delta\phi_i} = -2\sum_{j \neq i} \omega\lambda \int \mathrm{d}\mathbf{x}\, \nabla^2\phi_j. \tag{3.3}$$

This term is non-local, as it causes $\phi_i$ to grow everywhere in the domain, rather than in the vicinity of cell $i$. At sufficiently large values of $\omega$, this term violates the assumption underpinning the use of patches, that $\partial_t\phi_i \approx 0$ except near the centre of mass of cell $i$, and can cause phase-field cells to become non-contiguous. This is not the case for the range of values considered in this chapter; heuristically, the formulation of Equation (3.1) is acceptable.

In addition, the formulation of the polar force differs from that outlined in Chapter 2. Here we localise the polar force density on the front of the phase-field cell so as to model cytoskeleton polymerisation and integrin recruitment, which is biased by Rho GTPase enzymes [13, 19]:

$$\mathbf{f}_{\text{polar},i} = \alpha\lambda(-\nabla\phi_i \cdot \hat{\mathbf{p}}_i)\Theta(-\nabla\phi_i \cdot \hat{\mathbf{p}}_i)\hat{\mathbf{p}}_i \tag{3.4}$$

Here, the polarisation director $\hat{\mathbf{p}}_i = (\cos\theta_i, \sin\theta_i)$ is a unit vector. The Heaviside step restricts the force density to act on the part of the cell where $\nabla\phi_i \cdot \hat{\mathbf{p}}_i < 0$; that

is, on the front of the cell. Furthermore, the factor of $-\nabla\phi_i \cdot \hat{\mathbf{p}}_i$ maximises the force density where the gradient is antiparallel to the polarisation, and falls off towards the sides of the cell. The factor of $\lambda$ in the force density exists for dimensional reasons, to cancel out the inverse length dimension contributed by the gradient.

To ensure that the polarisation $\hat{\mathbf{p}}_i$ in this formulation is a unit vector, its dynamics necessarily differ from those outlined in Chapter 2. In contrast to Camley et al. [95] but in concert with Zhang et al. [67], the angle $\theta_i$ of the polarisation aligns to the long axis of the cell as

$$\partial_t \theta_i = -J_{\mathrm{pol}} \sqrt{-\det(\mathcal{D}_i)} \angle(\hat{\mathbf{p}}_i, \hat{\mathbf{d}}_{\parallel i}) + D_{\mathrm{pol}} \eta, \tag{3.5}$$

where $\mathcal{D}_i$ is the shape tensor as defined in Equation (2.14) and $\hat{\mathbf{d}}_{\parallel i}$ is the eigenvector corresponding to the largest eigenvalue of $\mathcal{D}_i$. The angle between $\hat{\mathbf{p}}_i$ and $\hat{\mathbf{d}}_{\parallel i}$ is taken to be acute because of the symmetry as $\hat{\mathbf{d}}_{\parallel i} \to -\hat{\mathbf{d}}_{\parallel i}$. Therefore the polarisation aligns more strongly with the shape axis of a highly elongated cell than it does with the shape axis of a slightly elongated cell. The coefficients $J_{\mathrm{pol}}$ and $D_{\mathrm{pol}}$ are a relaxation rate and a diffusion constant, respectively, and $\eta$ is Gaussian noise with unit variance: $\langle \eta \rangle = 0$, $\langle \eta(t)\eta(t') \rangle = \delta(t - t')$.

In this model, there is a positive feedback between polar activity $\alpha$, the shape of the cell, and the direction of the polarisation. Once the isotropic symmetry of the polarisation is broken, the polar force density in Equation (3.4) advects the front of the cell, deforming it along the axis of polarisation — but the axis of deformation controls the direction of the polarisation through Equation (3.5). The competition between alignment to shape and the noise requires $J_{\mathrm{pol}} \sqrt{-\det(\mathcal{D}_i)} \gtrsim D_{\mathrm{pol}}^2$ for persistent rotational motion to emerge, and this is where a threshold $\alpha$ for rotation originates. In addition, the coupling of shape to activity occurs at a rate $\tau_0^{-1} = \gamma h J_0 = \mathcal{O}(10^{-3})$ that competes with the polar reorientation rate $D_{\mathrm{pol}}^2$.

The dynamics is in the overdamped regime, with the frictional force balance at the substrate given by Equation (2.2):

$$\xi \mathbf{v}_i(\mathbf{x}, t) = \mathbf{f}_{\mathrm{passive},i}(\mathbf{x}, t) + \mathbf{f}_{\mathrm{active},i}(\mathbf{x}, t) \tag{3.6}$$

Because of the presence of noise in Equation (3.5), the model is solved using an implicit Euler-Maruyama scheme. The increments in the phase fields are computed as outlined in Equations (2.31), while the polar angle $\theta_i$ is updated iteratively as

$$\eta^{(0)} \sim N(0,1) \tag{3.7a}$$

$$\delta\theta_i^{(k+1)} = -J_{\mathrm{pol}}\sqrt{-\det(\mathcal{D}_i)}\angle(\hat{\mathbf{p}}_i^{(k)}, \hat{\mathbf{d}}_{\parallel i}^{(k)}) \tag{3.7b}$$

$$\theta_i^{(k+1)} = \theta_i^{(0)} + \delta t\, \delta\theta_i^{(k+1)} + \sqrt{\delta t} D_{\mathrm{pol}}\eta^{(0)} \tag{3.7c}$$

where $X^{(0)} = X(\mathbf{x}, t)$ for all variables. Thus the drift $\theta_i$ is revised for each of five predictor-corrector steps, while the noise term is sampled only once.

The confinement is modelled as a static phase field $\phi_{\mathrm{wall}}(\mathbf{x})$ given by

$$\phi_{\mathrm{wall}}(\mathbf{x}) = \begin{cases} \exp\Big(-\lambda_{\mathrm{wall}}(R^* - d(\mathbf{x}))\Big) & d(\mathbf{x}) < R^* \\ 1 & d(\mathbf{x}) > R^* \end{cases} \tag{3.8}$$

where $R^*$ is the radius of the confining circle and $d(\mathbf{x})$ is the distance from the centre of the domain to the point $\mathbf{x}$.

The control parameters in this model are $\alpha$, the strength of the active polar force, and $\omega$, the strength of the adhesive interaction between cells. We set $\alpha \in 1 \times 10^{-3}, 5 \times 10^{-1}]$ and $\omega \in [1 \times 10^{-1}, 5 \times 10^{-1}]$. The parameters in Equation 3.5 are set to $J_{\mathrm{pol}} = 2 \times 10^{-2}$ and $D_{\mathrm{pol}} = 1 \times 10^{-1}$. Other free energy parameters are $\gamma = 1.4$, $\lambda = 2.0$, $\mu = 120$ and $\kappa = 1.0$. Substrate friction is given by $\xi = 3.0$ and the target cell radius is $R = 8.0$. The passive relaxation is controlled by the parameter $J_0 = 1 \times 10^{-3}$. The confining walls have lengthscale $\lambda_{\mathrm{wall}} = 3.0$ and line energies for repulsion and adhesion $\kappa_{\mathrm{wall}} = 1.0$ and $\omega_{\mathrm{wall}}$, respectively.

Simulations of pairs of cells in confinement were run for $2 \times 10^5$ timesteps, and data were collected every 200 timesteps. The circular confinement had a radius of $R^* = 24.6$ lattice units and was implemented as a constant phase field $\phi_{\mathrm{wall}}$ that took a value 1 outside the circle and decayed exponentially with a lengthscale 1 inside the circle. The nominal area fraction, equal to the nominal area of all the cells, divided by the area of the confinement, is $\approx 0.85$.

## 3.3 Results

### 3.3.1 Single-Cell Motility

Equations (3.4) and (3.5) have a feedback between polar activity $\alpha$, shape $\sqrt{-\det(\mathcal{D}_i)}$ and polar angle $\theta_i$. However, the relationship is not as straightforward as, for example, that between self-propulsion velocity, rotational diffusion, and mean-square displacement for an active Brownian particle [104]. Indeed, it is not clear *a priori* what kind of relationship exists between $\alpha$ and self-propulsion velocity for a single phase-field cell. Therefore we investigate single-cell motility with polar dynamics given by Equations (3.4) and (3.5). We fix $J_{\mathrm{pol}} = 0.1$ in this Subsection, and run several several simulations for $t = 1 \times 10^5$ timesteps for either fixed $D_{\mathrm{pol}}$ or fixed $\alpha$.

Setting $D_{\mathrm{pol}} = 0$, we are able to find a relationship between polar activity $\alpha$ and self-propulsion velocity. The dynamics put the polar force density on only the front half of the cell, and let the rear of the cell recoil and decay as the rear of a single cell does *in vitro*. The relationship between self-propulsion and $\alpha$ is illustrated in Figure 3.1, which shows that, although a cell becomes faster with increasing $\alpha$, the relationship is not linear.

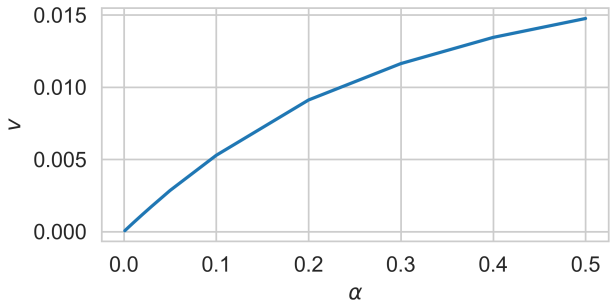


**Figure 3.1:** Self-propulsion velocity $v$ versus polar activity $\alpha$ for a single phase-field cell. The relationship is not linear, as only the front of the cell is advected by the active force, which changes the shape of the cell and thereby the position and velocity of the cell's centre of mass.

In addition, when $D_{\mathrm{pol}} = 0.1$ is fixed while $\alpha$ is varied, the translational diffusion coefficient is calculated on the interval $[2 \times 10^4, 1 \times 10^5]$ as

$$4D_{\mathrm{diff}}\Delta t \equiv \lim_{\Delta t \to \infty} \langle |\mathbf{r}(t + \Delta t) - \mathbf{r}(t)|^2 \rangle. \tag{3.9}$$

An active Brownian particle explores space with a diffusion constant proportional to the square of its velocity and inversely proportional to its reorientation rate. In this single-particle system, the self-propulsion velocity $v$ is coupled but not proportional to $\alpha$, as shown in Figure 3.1, and the reorientation according to the dynamics in Equation (3.5) occurs at rate $D_{\mathrm{pol}}^2$. Therefore we expect to $D_{\mathrm{diff}} \propto v^2 D_{\mathrm{pol}}^{-2}$.

The scaling $D_{\mathrm{diff}} \propto v^2$ holds, as illustrated in Figure 3.2 (a). However, the scaling $D_{\mathrm{diff}} \propto D_{\mathrm{pol}}^{-2}$, shown in Figure 3.2 (b), only holds for finite but sufficiently small $D_{\mathrm{pol}}$. This is because of the interplay between shape, noise and activity in the dynamics of Equations (2.1) and (3.5). Sufficiently strong noise, with $D_{\mathrm{pol}}^2 \gtrsim J_{\mathrm{pol}}\sqrt{-\det(\mathcal{D}_i)}$, causes the polarisation $\hat{\mathbf{p}}_i$ to reorient faster than it relaxes to the shape. In addition, the shape of a cell relaxes with rate $\tau_0^{-1} = \gamma h J_0 = \mathcal{O}(10^{-3})$, and if the cell's polarisation reorients faster than its shape adapts to the self-propulsion, then a long axis towards which the polarisation can relax will never be established. It is this latter competition that controls the spatial diffusion of the single cell, and Figure 3.2 (b) shows that the scaling $D_{\mathrm{diff}} \propto D_{\mathrm{pol}}^{-2}$ breaks down for $D_{\mathrm{pol}}^2 \gtrsim \tau_0^{-1}$.

We conclude that $\alpha$, which as a control parameter in the model is a useful proxy for self-propulsion velocity $v$, which determines the persistence length of a noisy walker such as a polar phase-field cell. We also find that the translational motion of a noisy polar phase-field cell is sensitive to the relationship between the rotational diffusion coefficient $D_{\mathrm{pol}}$ and the free energy relaxation rate $\tau_0^{-1} = \gamma h J_0$, which determines whether the cell is in the active Brownian regime or in the regime where the polar director aligns to the shape of the cell according to Equation (3.5), and the shape to the polar force according to Equation (2.1).

### 3.3.2 Pairwise Rotation

The phase-field cells in circular confinement either rotate or jam. Figure 3.3 illustrates the local velocity field and centre-of-mass velocity for two phase-field cells, along with their confining circle in rotating and jammed states. As a cell migrates towards the edge of the confinement, the repulsive force due to the wall guides the front of the cell around the circle and helps to realign the polar force.

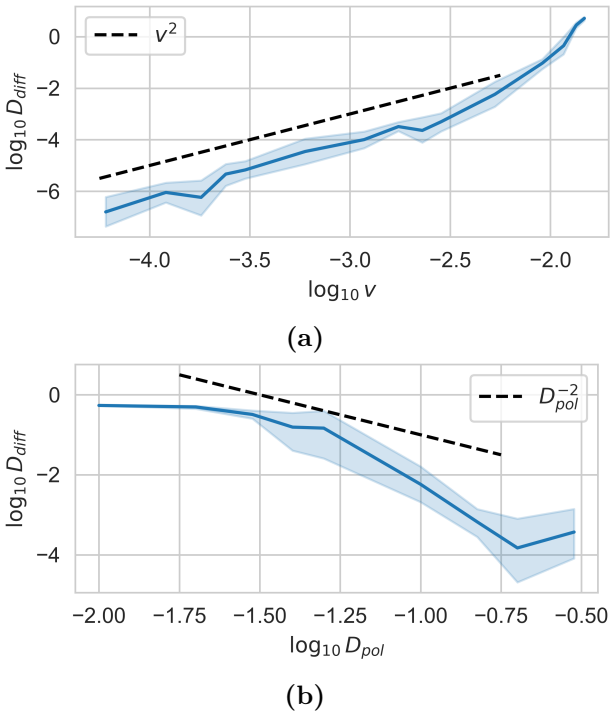


**Figure 3.2:** Translational diffusion constant $D_{\text{diff}}$ versus (a) self-propulsion velocity $v$ and (b) rotational diffusion coefficient $D_{\text{pol}}$. In (a) there is a scaling $D_{\text{diff}} \propto v^2$, indicated by the dashed black line. However, in (b), the translational diffusion coefficient drops off much more quickly than $D_{\text{pol}}^{-2}$, reflecting the fact that in the regime $D_{\text{pol}}^2 \sim \gamma h J_0$, the phase-field cell cannot be described as an active Brownian particle.

There is free space to migrate into, as in Figure 3.3 (a), if the other cell is also rotating in the same direction. If the polar directors are parallel, however, there is no room to move and the cells become jammed, as in Figure 3.3 (b).

In analysing the system's behaviour in the $\alpha$-$\omega$ phase space, the quantity of interest is the rotational order parameter

$$\Gamma = \frac{1}{N} \sum_i \hat{\mathbf{k}} \cdot \frac{(\mathbf{r}_i - \mathbf{r}_{\text{com}}) \times \Delta\mathbf{r}_i}{|(\mathbf{r}_i - \mathbf{r}_{\text{com}}) \times \Delta\mathbf{r}_i|} \tag{3.10}$$

where $N$ is the number of cells in the system, $\mathbf{r}_i$ is the centre-of-mass position of cell $i$, $\mathbf{r}_{\text{com}}$ is the centre of mass of the system of cells, and $\Delta\mathbf{r}_i$ is the displacement of cell $i$ between frames, which amounts to an average centre-of-mass velocity. The unit vector $\hat{\mathbf{k}}$ points out of the plane and serves to distinguish clockwise from anticlockwise rotation. The order parameter $\Gamma$ is equal to $\pm 1$ when all cells are rotating in the same direction around the system's centre of mass, and zero when there is no uniform large-scale rotational motion in the system, or if the system

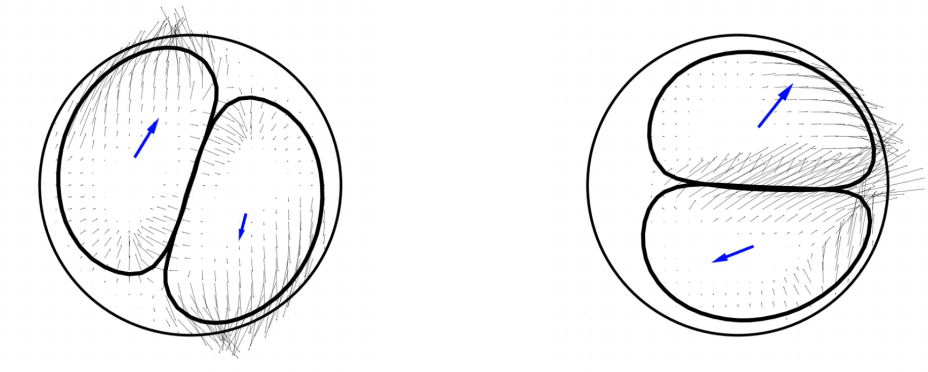

(a) (b)

**Figure 3.3:** Snapshots of two phase-field cells in (a) rotating and (b) jammed states. The black circle around the cells indicates region in which the phase-field cells are confined. The larger blue arrows indicate the centre-of-mass velocity at the previous timestep. Small black vector fields indicate the global velocity field $\mathbf{v}(\mathbf{x},t) = \sum_i \phi_i(\mathbf{x},t)\mathbf{v}_i(\mathbf{x},t)$, where the local velocity fields $\mathbf{v}_i(\mathbf{x},t)$ arise from the force balance in Equation 2.2. The bias of the velocity field towards the front of each cell reflects the distribution of the polar force of Equation 3.4, while the rear of each cell in (a) is advected in the direction of the centre-of-mass velocity. In the jammed state (b) the instantaneous centre-of-mass velocity fluctuates as the active polar force competes with the passive repulsion against the confining wall.

exhibits, for instance, azimuthal shear flow in an annulus [105]. The definition of $\Gamma$ in Equation (3.10) applies to systems with arbitrary numbers of cells, and the order parameter can therefore be measured to investigate rotational motion in large clusters of cells [37]. In system of two cells with strong confinement, jamming and persistent rotation are the only permitted behaviours.

A moving average of the rotational order parameter $\Gamma$ was computed over a twenty-frame window, corresponding to $4 \times 10^3$ simulation timesteps. We observe several contrasting rotating and jamming behaviours as we explore the $\alpha$-$\omega$ phase space, of which representative graphs of the time evolution of $\Gamma$ are illustrated in Figure 3.4. The three orders of magnitude in the interval for $\alpha$ are necessary to reveal different behavioural regimes. A threshold between $|\Gamma| = 0$ and 1 must be chosen; we determine heuristically that $|\Gamma| = 0.6$ provides an adequate threshold to distinguish rotational motion from jamming behaviour so as to include short-lived rotations as illustrated in Figure 3.4 (b) but to exclude fluctuations.

Each simulation generically resulted in several periods of rotation, indicated by

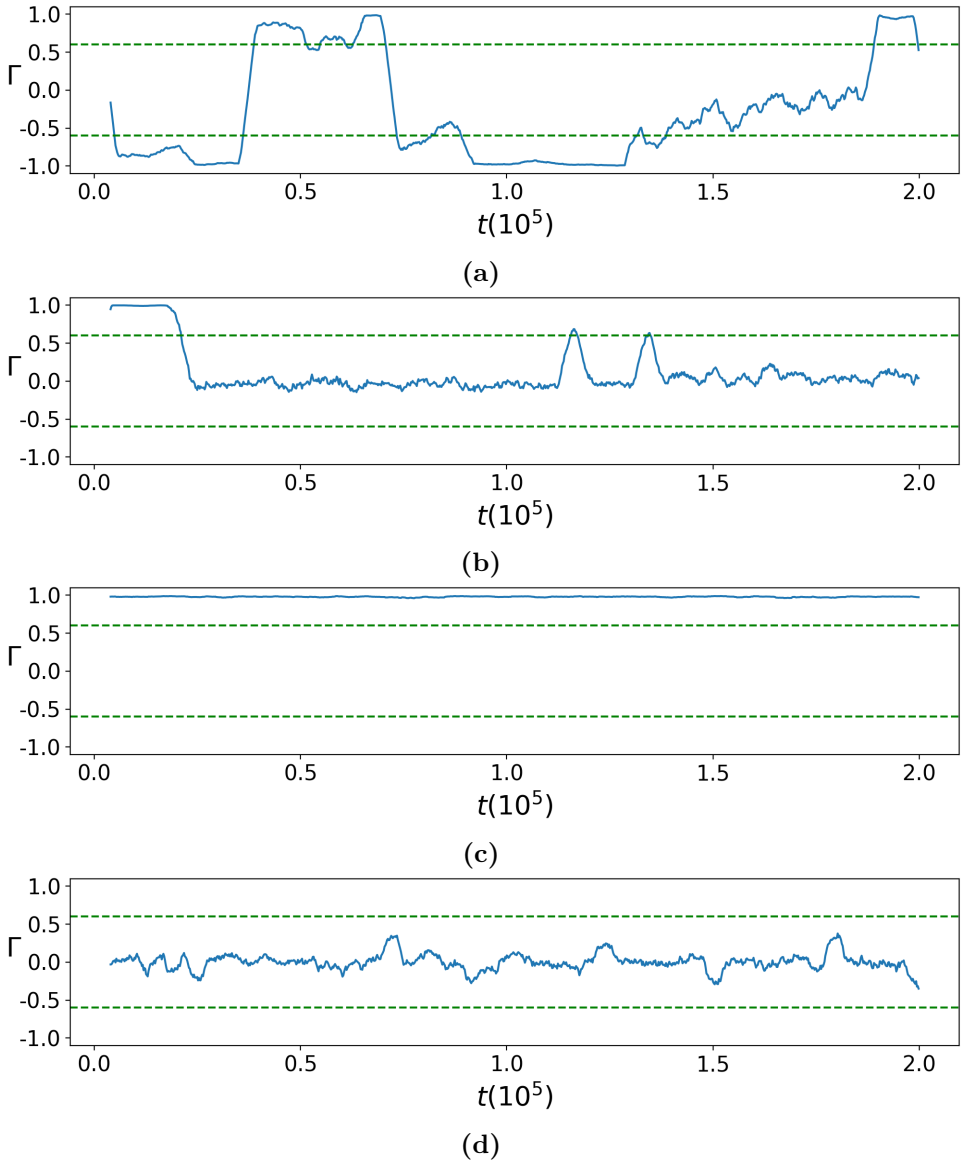


**Figure 3.4:** Summary of different regimes for the time evolution of the rotational order parameter $\Gamma$. In all cases $D_{\text{pol}} = 0.1$. The threshold $|\Gamma| = 0.6$ is illustrated as a dashed green line. (a) The case for low persistence $\alpha = 5 \times 10^{-3}$ and low adhesion $\omega = 1 \times 10^{-2}$. The noise kicks the cells between periods of rotating, both clockwise and anti-clockwise, and jamming. Statistically, these cells spend more of their time in rotation than in jamming, as shown in Figure 3.6. In (b), adhesion ($\omega = 0.4$) is strong enough to overpower self-propulsion ($\alpha = 1 \times 10^{-3}$), even when noise causes a transient period of rotation, measured by $|\Gamma| > 0.6$. Both (c) and (d) represent the regime with large $\alpha = 0.1$ and large $\omega = 0.5$, where cells' persistence is strong enough to either rotate or to jam for the entire simulation, sensitive to the initial condition.

$|\Gamma| \approx 1$, and jamming, indicated by $|\Gamma| \approx 0$, as illustrated for example in Figure 3.4 (a). Using the threshold $|\Gamma|$, we calculated the duration of each period of rotation $\tau_{r,ij}$ the *rotation time* and the duration of each period of jamming, denoted by

$\tau_{w,ij}$ the *waiting time*. The subscript $i$ indexes each of several simulations, which is split according to the threshold $\Gamma$ into several periods of rotation and jamming, which are indexed separately by the subscript $j$. Then ensemble mean rotation and waiting times were calculated as

$$\langle \tau_r \rangle \equiv \langle \tau_{r,ij} \rangle_{ij}, \langle \tau_w \rangle \equiv \langle \tau_{w,ij} \rangle_{ij} \tag{3.11}$$

over all instances of rotation and waiting $j$ over all simulations $i$. In more persistent regimes, there are fewer but longer instances of rotation and waiting and so the ensemble means may have larger error bars. In addition, the *rotation fraction* was calculated for each simulation instance $i$ as

$$\Omega_i = \frac{\sum_j \tau_{r,ij}}{\sum_j (\tau_{r,ij} + \tau_{w,ij})}. \tag{3.12}$$

When both the strength of the polar force and the cell-cell adhesion are small, as in Figure 3.4 (a), the model exhibits short persistence times for both rotation $\langle \tau_r \rangle$ and waiting $\langle \tau_w \rangle$. These durations are quantified in Figure 3.5. In this fluctuating regime, there is little self-propulsion and the cells are coupled only weakly: the noise, mediated by $D_{\text{pol}}$, is strong enough to cause the system eventually to switch between rotation and jamming. For weak polar force and strong cell-cell adhesion, as in Figure 3.4 (b), the passive adhesive attraction overpowers the active force and the noise, resulting in jamming for almost the entire simulation. The ensemble mean $\langle \tau_w \rangle$ is much larger than $\langle \tau_r \rangle$, as illustrated in the upper left-hand corners of Figure 3.5 (a) and (b).

When both the polar force and the cell-cell adhesion are strong, as in Figure 3.4 (c) and (d), the system becomes extremely persistent: due to the feedback between $\alpha$ the activity, $\mathcal{D}_i$ the shape tensor, and $\hat{\mathbf{p}}_i$ the polarisation, the noise is too weak to affect the direction of $\hat{\mathbf{p}}_i$. In addition, for large $\alpha$, the polar force is no longer overpowered by adhesion. Therefore, the long-time behaviour becomes sensitive to the initial condition, which highlights the importance of repeated simulations in this investigation. A pair of cells prepared in a rotating initial condition continue to rotate for the duration of the simulation, while a pair of cells prepared in a jammed

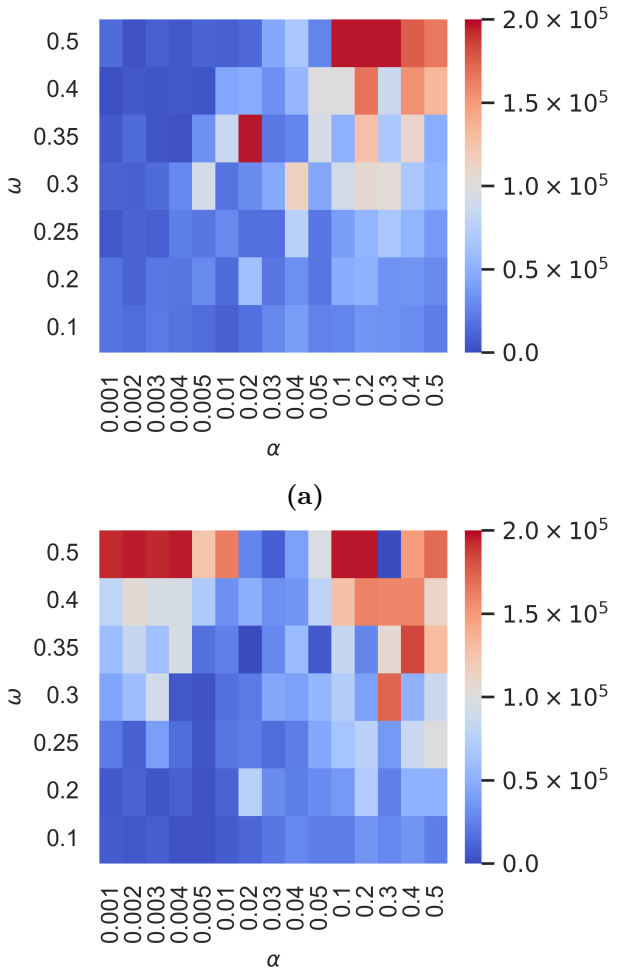


**Figure 3.5:** Heatmaps of ensemble mean (a) rotation times $\langle \tau_r \rangle$ and (b) waiting times $\langle \tau_w \rangle$ for pairs of cells in circular confinement in the $\alpha$-$\omega$ phase space. When the polar force and cell-cell adhesion are sufficiently weak, the durations of rotating and jamming behaviour are both short. When just the adhesion parameter $\omega$ is increased, the system jams for longer times, with only short excursions into rotating behaviour: only the values $\langle \tau_w \rangle$ grow longer. When both $\alpha$ and $\omega$ are large, the system enters a highly persistent regime, where the cells either rotate or jam for almost the entire duration of the simulation.

initial condition continue to jam. This is the regime where both $\langle \tau_r \rangle$ and $\langle \tau_w \rangle$ are large, as shown in the upper right-hand corners of Figure 3.5 (a) and (b).

The rotation fraction $\Omega_i$, defined in Equation (3.12), provides another tool with which to analyse the system, particularly in the regime of low $\alpha$ and low $\omega$, where due to noise the cells rotate one way and then another for short periods, and jamming is typically transitory. The mean rotation fraction $\langle \Omega \rangle \equiv \langle \Omega_i \rangle_i$ is illustrated by the heat map in Figure 3.6. This heat map recapitulates the behaviours shown in

Figures 3.4 and 3.5 and, in addition, indicate the regions of phase space in which fluctuating, jamming, and persistent behaviours occur.

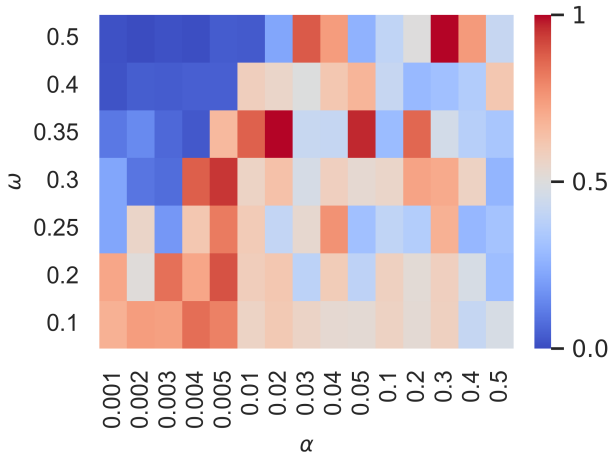


**Figure 3.6:** Heatmap of ensemble mean rotation fraction $\langle\Omega\rangle$, as defined in Equation (3.12). For small self-propulsion and small adhesion, the system rotates for a longer duration than it jams, as indicated by comparison to the threshold $|\Gamma| = 0.6$. As both $\alpha$ and $\omega$ grow larger, the rotation fraction decreases towards $1/2$ as the system becomes more persistent and different simulations either rotate or jam for the full duration of the simulation. When $\alpha$ is small and $\omega$ is large, the rotation fraction drops close to zero as adhesion jams the system to the point that persistent self-propulsion never develops.

The two regions of high $\langle\tau_w\rangle$ result from different features of the systems at hand, and this is clear from comparing the heatmaps of $\langle\tau_w\rangle$ and $\langle\Omega\rangle$. In the low-$\alpha$, high-$\omega$ region, as shown in Figure 3.5, the system waits for long times because the cells are insufficiently persistent, while in the high-$\alpha$, high-$\omega$ region, the cells are so persistent that if the system is initially jammed, it will stay jammed indefinitely. This distinction is reflected in the heatmap of rotation fractions, illustrated in Figure 3.6, which shows a rotation fraction in the latter region close to $1/2$, compared with close to zero in the former region.

These properties of $\langle\tau_r\rangle$, $\langle\tau_w\rangle$, and $\langle\Omega\rangle$ are recapitulated in Figure 3.7, which shows these three values versus $\log_{10}\alpha$ for values of $\omega$ in $[0.1, 0.5]$. Figure 3.7 (a) shows that the rotation time grows gradually with $\alpha$ for all values of $\omega$ before dropping off at the highest value of $\alpha = 0.5$. Figure 3.7 (b) indicates that for values of $\omega \gtrsim 0.3$, the waiting time drops at a threshold $\alpha$, which increases with $\omega$, before increasing again for larger values of $\alpha$. The sudden drop in $\langle\tau_w\rangle$ is concomitant with

a sharp rise in $\langle\Omega\rangle$, and it is for these values of $\alpha$ that the mean rotation fraction tends to be the highest, since in the highly persistent $\alpha = 0.5$ regime, the dependence on initial condition results in $\langle\Omega\rangle = 1/2$. Although the data shown in the figures are noisy, it is possible still to see where the values of $\langle\tau_r\rangle$ and $\langle\tau_w\rangle$ are small or large, and consequently whether the corresponding rotation fractions $\langle\Omega\rangle$ are close to $1/2$ or not and justifies the identification of three behavioural regimes in $\alpha$-$\omega$ space.

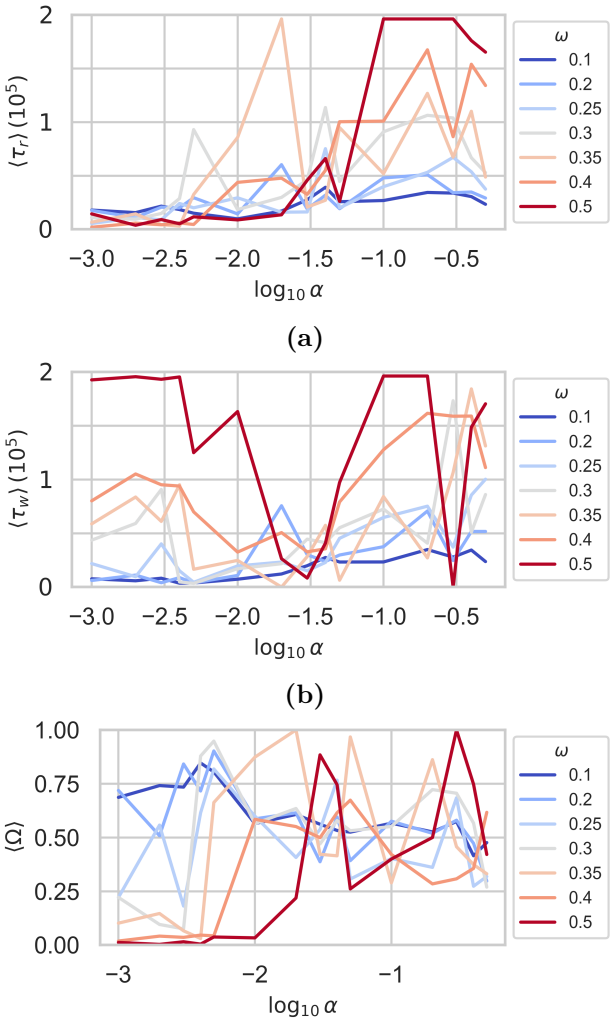


**Figure 3.7:** Graphs of (a) $\langle\tau_r\rangle$, (b) $\langle\tau_w\rangle$ and (c) $\langle\Omega\rangle$ versus $\log_{10}\alpha$ for several values of the adhesion parameter $\omega$. (a) Mean rotation time $\langle\tau_r\rangle$ initially increases with $\alpha$ for all values of $\omega$, while (b) mean waiting time $\langle\tau_w\rangle$ decreases then increases with $\alpha$ for all but the smallest values of $\omega$. (c) Values of $\langle\Omega\rangle$ approach $1/2$ in the most persistent regime $\alpha = 0.5$, while there is a region of small $\alpha$ and $\omega$ where the rotation fraction is close to 1. This region corresponds to Figure 3.4 (a).

### 3.3.3 Noise

Next we consider $D_{\text{pol}}$ as a control parameter. The diffusion constant $D_{\text{pol}}$ in Equation (3.5) is an additional way to control the persistence of the polarisation $\hat{\mathbf{p}}_i$. We vary $D_{\text{pol}} \in (0.0, 0.3]$ for two points in $\alpha$-$\omega$ space: $(\alpha, \omega) = (0.01, 0.01)$ and $(0.1, 0.4)$. The former point is in the weakly persistent regime, which flips frequently between clockwise and anticlockwise rotation, as in Figure 3.4 (a), and the latter is in the highly persistent regime and behaves as Figure 3.4 (c) and (d).

For each pair $(\alpha, \omega)$, three simulations were completed, each of $2 \times 10^5$ timesteps, and the same analysis of the rotational order parameter $\Gamma$ in terms of $\langle \tau_r \rangle$, $\langle \tau_w \rangle$ and $\langle \Omega \rangle$ was completed. Figure 3.8 depicts the three metrics versus the rotational diffusion constant $D_{\text{pol}}$, including a 95% confidence interval. In the persistent and noisy limits $D_{\text{pol}} = 0$ and $D_{\text{pol}} = 0.3$, there is no qualitative difference between the behaviours at the two points in phase space, $(\alpha, \omega) = (0.01, 0.01)$ and $(0.1, 0.4)$, because the rotational diffusion controls the behaviour of the system. For $D_{\text{pol}} = 0$ the coupling between shape and polarisation according to Equation 3.5 is perfect, and there is no requirement that $\alpha$ be sufficiently large to deform a cell so as to strengthen the feedback. In the opposite limit with large $D_{\text{pol}}$, here taken to be $D_{\text{pol}} = 0.3$, Equation 3.5 approaches rotational diffusion with reorientation rate $D_{\text{pol}}^2$. This is no surprise, as Figure 3.2 (b) indicates that for a single cell, translational diffusion is cut off sharply as $D_{\text{pol}}^2$ grows larger than the passive relaxation rate $\tau_0^{-1} = \gamma h J_0$.

For intermediate noise, however, the mean $\langle \tau_r \rangle$ illustrated in Figure 3.8 is clearly different for the two points in phase space, $(\alpha, \omega) = (0.01, 0.01)$ and $(0.1, 0.4)$. This part of the regime corresponds to the discussion in Section 3.3.2 when $D_{\text{pol}} = 0.1$. In this intermediate regime the reshaping of the cell as well as the alignment of polarisation to shape compete with noise, which requires $\tau_0^{-1} \gtrsim D_{\text{pol}}^2$ and $J_{\text{pol}} \sqrt{-\det(\mathcal{D}_i)} \gtrsim D_{\text{pol}}^2$. Indeed, as Figure 3.9 indicates, there is a local maximum of $\sqrt{-\det(\mathcal{D}_i)}$ that coincides with the maxima of $\langle \tau_r \rangle$ and $\langle \Omega \rangle$. The cells with $\alpha = 0.01$ are less strongly deformed and engage in rotational motion that is clearly less persistent than that of the cells with $\alpha = 0.1$ because their $\sqrt{-\det(\mathcal{D}_i)}$ is so small that the alignment to shape is comparatively weaker than rotational noise.

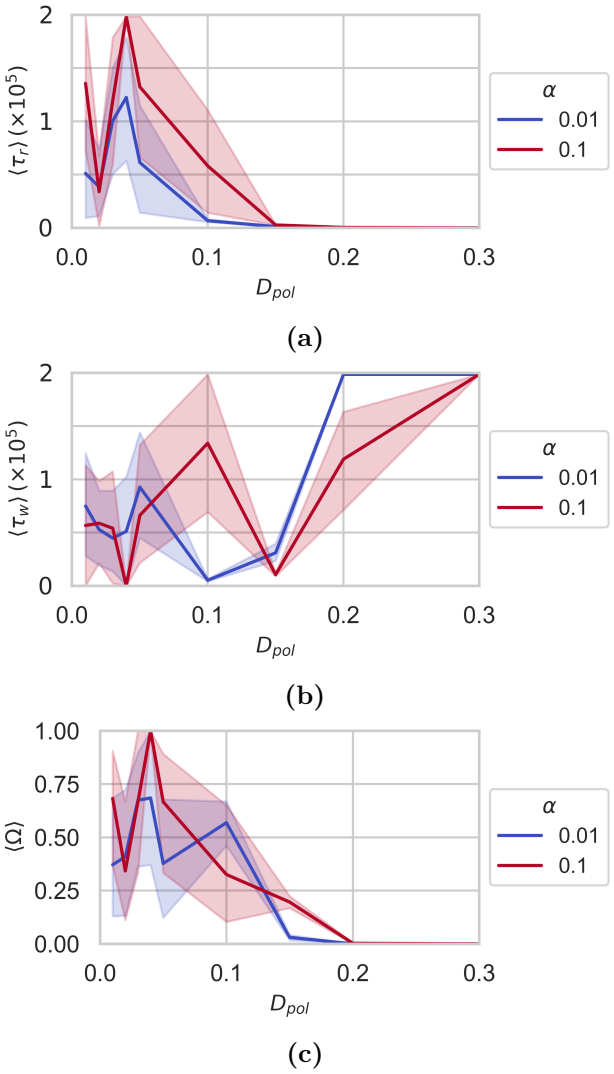


**Figure 3.8:** Graphs of $\langle\tau_r\rangle$ (a), $\langle\tau_w\rangle$ (b) and $\langle\Omega\rangle$ (c) against rotational diffusion coefficient $D_{\text{pol}}$ for two points in phase space, one with weak polar activity $\alpha = 0.01$ and one with strong polar activity $\alpha = 0.1$. In both cases, there is an optimum $D_{\text{pol}}$ that increases the mean rotation time $\langle\tau_r\rangle$ and maximises the mean rotation fraction $\langle\Omega\rangle$. As $D_{\text{pol}}$ becomes large, the polar force is no longer coupled to cell shape and the cells enter the active Brownian regime.

## 3.4 Discussion

Having investigated persistent rotation of motion in pairs of phase-field cells, we have found there is a competition between the adhesion between the cells and the strength of the polar activity that promotes or inhibits rotational motion at different points in $\alpha$-$\omega$ phase space. Furthermore, there is a feedback between the strength of polar activity $\alpha$ and magnitude of the shape $\sqrt{-\det(\mathcal{D})_i}$ that competes

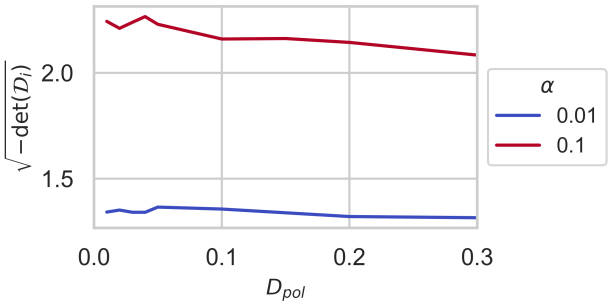


**Figure 3.9:** The value of $\sqrt{-\det(\mathcal{D})_i}$, which quantifies the deformation of a phase-field cell, versus $D_{\mathrm{pol}}$. For small but nonzero noise, there is a local maximum for both points in phase space, $(\alpha, \omega) = (0.01, 0.01)$ and $(0.1, 0.4)$, past which the shape magnitude decreases. This local maximum coincides with the peaks in $\langle \tau_r \rangle$ and $\langle \Omega \rangle$, shown in Figure 3.8 (a) and (c), respectively, because persistence competes with noise when $J_{\mathrm{pol}} \sqrt{-\det(\mathcal{D}_i)} \gtrsim D_{\mathrm{pol}}^2$.

with the strength of the noise $D_{\mathrm{pol}}$ to create persistent rotational motion, which is inhibited for sufficiently strong noise.

Next, we seek to recover rotational motion and system-scale flows for large numbers of cells, as has been observed *in vitro* [36, 37]. Furthermore, because lamelliopodia and polar activity are suppressed in confluent epithelia [11, 14], we aim to model epithelial behaviours using dipolar activity by analogy to active nematohydrodynamics [7, 38]. Therefore, Chapter 4 models a mixture of extensile and contractile cells and investigates their microphase separation, with parallels in experiment and implications for morphogenesis.

*Everything was happening so oddly that she didn't feel a bit surprised at finding the Red Queen and the White Queen sitting close to her, one on each side: she would have liked very much to ask them how they came there, but she feared it would not be quite civil.*

— Lewis Carroll [2]

# 4 Active Phase Separation

## 4.1 Introduction

Cell sorting, the separation of mixtures of different cell types into distinct domains reminiscent of phase ordering in fluids, has long been a topic of interest in the biological literature [106–108]. It is a vital component of embryogenesis and morphogenesis, relevant to how cells organise according to type prior to differentiation, and is conserved across vertebrates and invertebrates. Model systems, for example plated confluent layers, that include different types of cell also often show localised de-mixing [39, 107, 109]. A number of mechanisms have been suggested to explain cell sorting in tissues, and investigated both *in vitro* and *in silico*. These can appeal to differences in cell adhesion, line tension, or activity [110–112]. Other characteristics of a monolayer such as cell motility [43] or area and shape [113] may also play a role in cell sorting.

The Differential Adhesion Hypothesis introduced by Steinberg [107] proposes that a cell preferentially adheres to cells of the same, rather than another, type. Differential adhesion leads to variations in tissue surface tension, and results in a thermodynamic separation akin to that of oil and water. The earliest mechanism proposed to explain cell sorting, the DAH gained currency and has been investigated experimentally in cell aggregates expressing varying levels of cadherins [110]. The

hypothesis has been used to describe the sorting of heterogeneous monolayers *in vitro* [112], and *in silico* through particle-based and cellular-Potts model simulations [58–60].

Complementary to the DAH is the Differential Interfacial Tension Hypothesis, which considers the tension at cell-cell junctions. This hypothesis holds that line tension can modulate and regulate cell sorting, and even permit one tissue to completely surround another [114]. It has been shown that cell junction tension controls cell sorting in *Drosophila* [111]. In addition, fluctuations in line tension in a vertex model can result in intercalations [115] and cell sorting [54].

Experiments by Skamrahl et al. show that differences in the line tension at junctions between cells of different types, which the authors refer to as contractility, has an interplay with differential adhesion during cell sorting [112]. In this work, the authors compare cultures of wild-type Madin-Darby Canine Kidney cells to 'dKD' cells, which have a protein knockdown that enhances contractility. To analyse cell sorting, they tag wild-type cells with green fluorescent protein and mix them with either dKD cells or untagged wild-type cells. The mixture of dKD and wild-type cells separates into patches of each type. The authors also found that demixing proceeds in a two-stage process: a fast stage followed by a slow stage. They attribute the fast time scale to differential contractility, and the slow time scale to differential adhesion.

Other factors have also been implicated in cell sorting in a monolayer. Heine et al. observed the influence of the solid- or fluid-like nature of a cell culture on sorting within the differential adhesion framework [43]. There are also suggestions that the apical surface area of epithelial cells can affect sorting [112, 113].

Moreover, living systems are *active*. They continuously use chemical energy to drive motility and growth, and hence remain out of thermodynamic equilibrium. Recent work has successfully interpreted collective processes in mechanobiology in terms of the theories of active matter, and in particular of active nematics. Balasubramaniam et al. [39] observed incomplete cell sorting in a mixture of two MDCK cell strains with different strengths of inter-cellular interactions. They interpreted these results in terms of a mixture of dipolar active extensile and active

contractile cells and complemented the experimental results with simulations of a phase-field model. A two-fluid continuum model has also been used to show that fluids of different activities can undergo micro-phase separation [92].

Thus many different mechanisms can result in a degree of cell sorting, and the interplay of several may be necessary for complete, well-controlled segregation in a given biological process [43, 109]. To obtain a more complete understanding of sorting phenomena in cell monolayers and tissues, it is crucial to investigate each of the mechanisms involved. Isolating individual processes is difficult in experiment but modelling can play a useful role in this regard. Therefore here we implement a phase-field model and concentrate on asking whether active forces acting between cells, which arise from cadherin-based intercellular junctions, can result in sorting in a confluent cell monolayer.

In the next Section, we discuss the phase-field model, including both the passive dynamics of each cell and the active forces between cells. In Section 3 we present results indicating that cells of different activities undergo localised sorting. Our results are summarised and discussed in Section 4.

## 4.2 Model

The version of the multi-phase field model used in this Chapter largely matches that detailed in Chapter 2. The self-energy of each phase-field cell is described by the Cahn-Hilliard and area conservation terms in Equations (2.4). Passive interactions are modelled by the repulsive free energy density in Equation (2.6a). Any adhesion between cells according to Equation (2.6b) is neglected by setting $\omega = 0$.

Each cell has a nematic director $\mathbf{n}_i$ that relaxes towards the long axis of the cell according to

$$\frac{\mathrm{d}\mathbf{n}_i}{\mathrm{d}t} = -J_n\Big(\mathbf{n}_i - \mathrm{sgn}(\mathbf{n}_i \cdot \hat{\mathbf{d}}_{\parallel,i})\,\hat{\mathbf{d}}_{\parallel,i}\Big). \tag{4.1}$$

Equation (4.1) has a symmetry as $\hat{\mathbf{d}}_{\parallel,i} \to -\hat{\mathbf{d}}_{\parallel,i}$, so there are two fixed points: $\mathbf{n}_i = \pm\hat{\mathbf{d}}_{\parallel,i}$. Therefore the dynamics has the desired head-tail symmetry, and $\mathbf{Q}_i$

reorients towards the shape tensor $\mathcal{D}_i$, defined in Equation (2.14). Figure 4.1 shows a cartoon depicting the dynamics of $\mathbf{n}_i$.

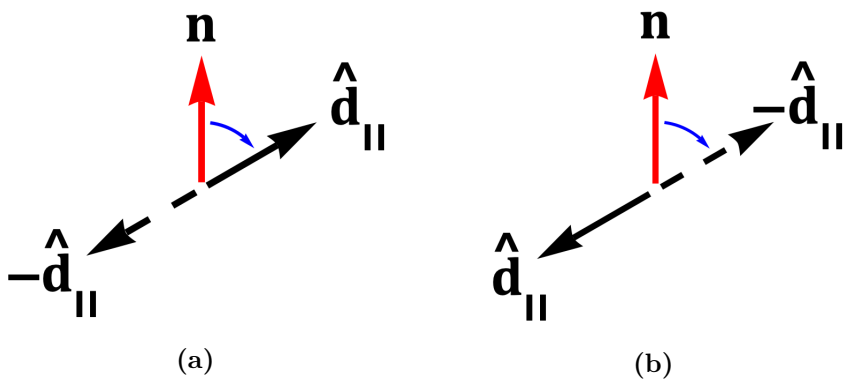


**Figure 4.1:** Cartoon of the relaxation of $\mathbf{n}_i$, in red, according to Equation (4.1). (a) When $\mathbf{n}_i \cdot \hat{\mathbf{d}}_{\parallel,i} > 0$, $\mathbf{n}_i$ relaxes towards $\hat{\mathbf{d}}_{\parallel,i}$ (solid), and (b) when $\mathbf{n}_i \cdot \hat{\mathbf{d}}_{\parallel,i} < 0$, $\mathbf{n}_i$ relaxes towards $-\hat{\mathbf{d}}_{\parallel,i}$ (dashed).

We distinguish self-induced dipolar active forces from those that arise from neighbour interactions by writing

$$\mathbf{f}_{\text{dipolar},i} = -\zeta_{\text{self},i}\mathbf{Q}_i \cdot \nabla\phi_i - \sum_{j\neq i} \zeta_{\text{inter},j}\mathbf{Q}_j \cdot \nabla\phi_j. \tag{4.2}$$

This treatment follows the $\sigma \sim \mathbf{Q}$ prescription of active nematohydrodynamics [7, 40]. We are interested in intercellular active stresses, so we choose $\zeta_{\text{self},i} = 0$. In order to compare mixtures of extensile and contractile cells, we generally choose a single $|\zeta_{\text{inter}}|$ and set $\zeta_{\text{inter},i} = \pm|\zeta_{\text{inter}}|$. The activities $\zeta_{\text{inter},i}$ can in addition be chosen to create extensile-passive and contractile-passive mixtures and, more generally, set to any arbitrary value.

This Chapter is concerned with mixtures of extensile and contractile cells in the bulk, so the system is modelled using periodic boundary conditions along both axes. There are no phase fields to model walls, and consequently no free energy densities to model interactions with walls.

To demonstrate the active phase separation, we simulate 672 phase-field cells in a square domain measuring $560 \times 560$ lattice units. Each cell is initalised in a random location with radius $R/2$ and the model epithelium is relaxed as though it were passive for $5 \times 10^3$ timesteps, after which activity is turned on and data

are collected. The simulation lasts $5 \times 10^5$ timesteps and data are recorded every $1 \times 10^3$ timesteps. In addtion, we compare different geometric configurations and choices of activity using simulations smaller in both length and timescale. These smaller simulations use 336 phase-field cells in a box measuring $280 \times 280$ lattice units and last $1 \times 10^5$ timesteps.

We choose $\gamma = 1.4$, $\lambda = 2.0$, $\mu = 120$ and $\kappa = 1.5$. The coefficient of friction is $\xi = 3.0$ and the target cell radius is $R = 8.0$. The relaxation parameters are $J_0 = 5 \times 10^{-3}$ and $J_n = 1 \times 10^{-1}$, with associated timescales $\tau_0 = (\gamma h J_0)^{-1} = \mathcal{O}(10^2)$ and $\tau_n = 10$, where $h = 1$ is the lattice spacing. Extensile cells are assigned $\zeta_{\text{inter},i} = +0.4$ and contractile cells are assigned $\zeta_{\text{inter},i} = -0.4$. We describe the target packing fraction as the total area fraction of cells divided by the area of the domain, which is $\approx 0.86$.

## 4.3 Results

To investigate whether cell sorting can be driven by differences in active inter-cellular forces, we prepared an equal mixture of cells with extensile and contractile activities, $\zeta_{\text{inter}} = 0.4$ and $\zeta_{\text{inter}} = -0.4$, respectively. All other simulation parameters were identical for both cell types. The simulation was started by placing 672 cells of each type randomly in the simulation domain which measured 560 by 560 lattice units. This number density corresponds to a cell density where the cell layer is confluent, but cell motion is still possible.

### 4.3.1 Ordering

First, we describe the microphase separation by investigating the segregation index, a measure of demixing, as well as the lengthscale of the density autocorrelation function, which characterises the size of clusters in the system. Then, we attempt to describe a mechanism for the microphase separation by characterising the differences in diffusivity between the extensile and contractile cells, and by investigating the free energy in the system before and after sorting.

Figure 4.2 (a) and (b) illustrate the configurations at $t = 1 \times 10^3$ and after $t = 5 \times 10^5$ time steps. The snapshots show evidence of partial cell sorting into elongated clusters; these clusters coalesce, break up, and re-form during the simulation. As a comparison we simulate a fully sorted state with 336 cells in a $280 \times 280$ box, with extensile and contractile cells separated into macroscopic regions as shown in Fig. 4.2 (c), (d). The cells show no tendency to mix on the time scale of the simulation (here to $t = 1 \times 10^5$), therefore both microphase and macrophase separation persist for long times.

Extensile cells are substantially deformed, while contractile cells are elongated slightly by the dipolar forces and demonstrate nematic alignment. These microphase-separated clusters show features of bulk phase-field nematics: Figure 4.3 shows the 'capped-line' state typical of extensile cells, which is not qualitatively dissimilar to the arrangement of rod-like molecules into 'disordered domains' at right angles to one another, as observed by de Gennes [73]. Figure 4.3 also shows the nematic phase of contractile cells, formed from parallel strands of cells joined end to end. In these strands, the contractile cells pull on the ends of their neighbours, causing them to elongate slightly and to have a well-defined shape tensor $\mathcal{D}_i$ along which to align the nematic director $\mathbf{n}_i$. Contractile cells organise into these nematic strands even, as shown in Figure 4.2, in mixtures with extensile cells.

Indeed, it is possible to quantify an autocorrelation function of the nematic tensor separately for the constituent parts of an extensile-contractile mixture. We define the nematic tensor $\mathbf{Q}_\zeta$ restricted to a particular activity $\zeta$ as

$$\mathbf{Q}_\zeta(\mathbf{x}, t) = \sum_{i:\zeta_{\text{inter},i}=\zeta} \mathbf{Q}_i \phi_i(\mathbf{x}, t) \tag{4.3}$$

and define the nematic correlation function $C_Q(r)$ as

$$C_Q(\mathbf{r}, t) = \langle \mathbf{Q}_\zeta(\mathbf{x}) \mathbf{Q}_\zeta(\mathbf{x}+\mathbf{r}) \rangle - \langle \mathbf{Q}_\zeta(\mathbf{x}) \rangle \langle \mathbf{Q}\zeta(\mathbf{x}+\mathbf{r}) \rangle \tag{4.4}$$

where the average is taken over positions $\mathbf{x}$ and components of the tensor $\mathbf{Q}_\zeta$. The quantity $C_Q(r)$ is then obtained by further averaging over orientations and time. Figure 4.4 shows $C_Q(r)$ separately for extensile and contractile cells in the

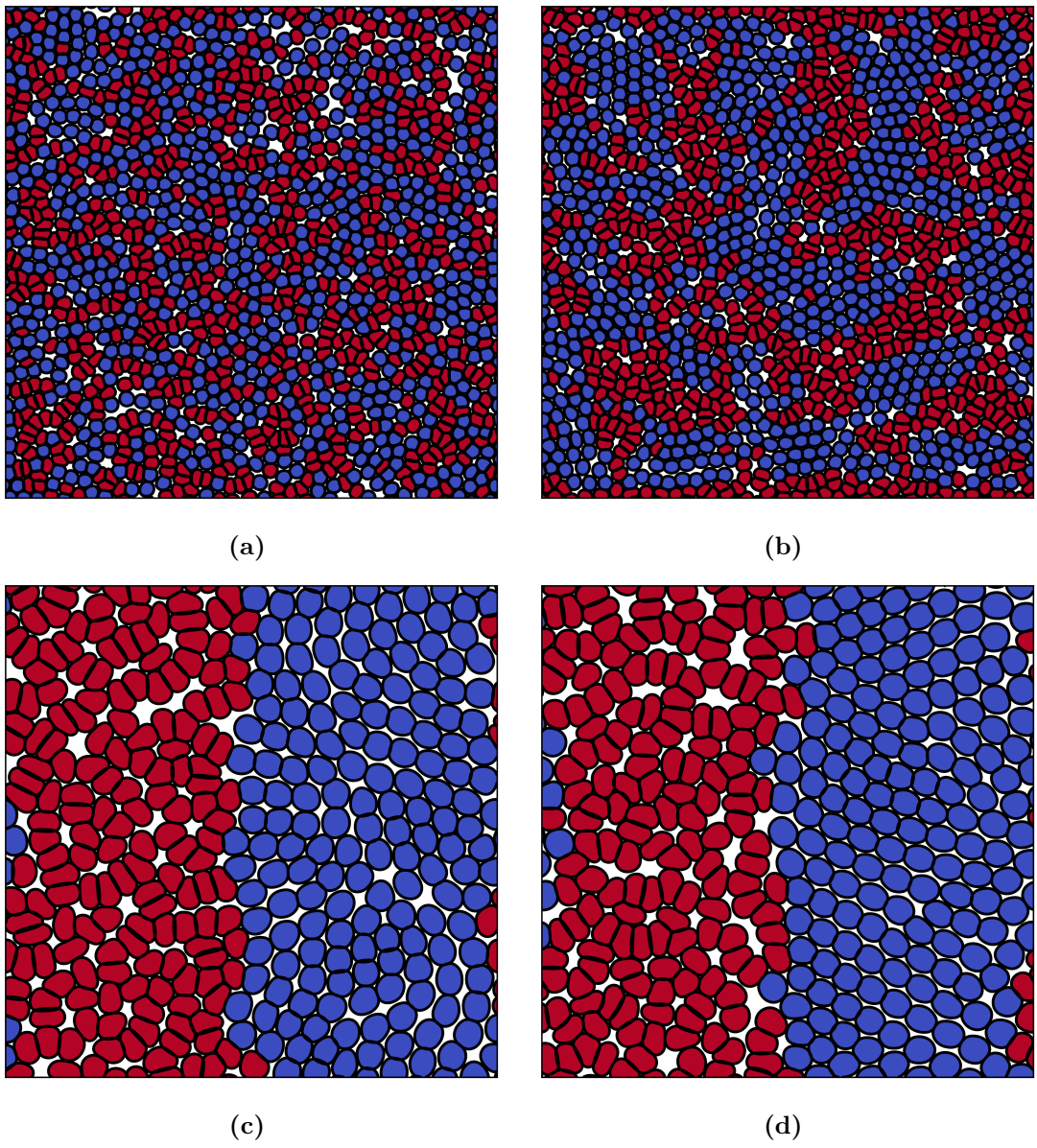


**Figure 4.2:** Segregation in a 1 : 1 mixture of extensile (red) and contractile (blue) cells. (a) $t = 1 \times 10^3$, (b) $t = 5 \times 10^5$ for a fully mixed initial condition showing microphase separation. (c) $t = 1 \times 10^3$, (d) $t = 1 \times 10^5$ for a state that is fully sorted at the beginning of the simulation and which does not mix. Note that the contractile cells develop nematic order.

mixture illustrated in Figure 4.2 (b). It is clear that nematic order decays in extensile cells on the lengthscale of a single cell, while nematic order has a much larger lengthscale for contractile cells.

We seek to quantify the phase separation of mixtures of cells and describe its mechanism. There are a number of ways to measure the segregation in a system [39,

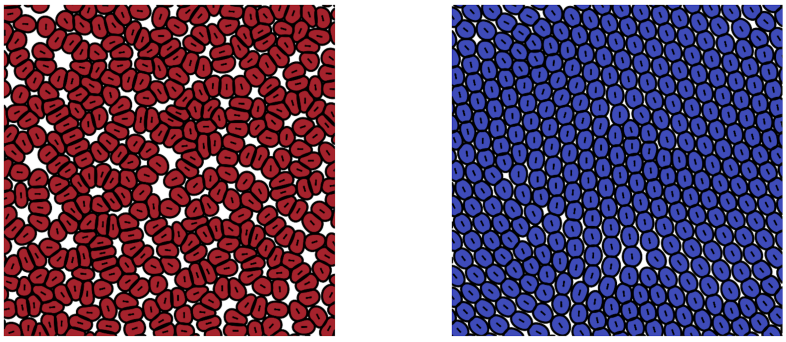

**(a)** **(b)**

**Figure 4.3:** Monolayers of $n = 336$ (a) extensile ($\zeta_{\text{inter}} = +0.4$) and (b) contractile ($\zeta_{\text{inter}} = -0.4$) cells. The headless nematic director $\mathbf{n}_i$ is indicated as a black line on each cell. The extensile system is unjammed and has free space, while the contractile system is close to jammed. Extensile cells are deformed and align into a 'capped-line' texture, while contractile cells form a nematic phase.

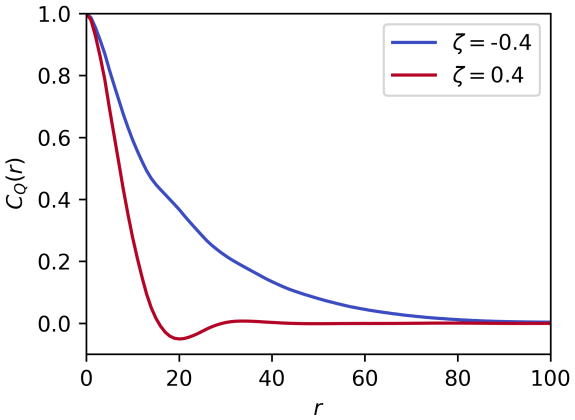


**Figure 4.4:** Nematic correlation function $C_Q(r)$, defined *via* Equations (4.3) and (4.4), for extensile and contractile cells in the system illustrated in Figure 4.2 (b). The time average is computed over the final $5 \times 10^4$ timesteps of the simulation. The lengthscale of $C_Q(r)$ for extensile cells is commensurate with the diameter of a single cell, indicating they have poor nematic order. Meanwhile, contractile cells exhibit nematic order over a much longer distance.

59, 112, 116]. Following [112], we define a segregation index by counting the neighbours of each cell. Two phase-field cells are identified as neighbours when the corresponding phase fields take a value greater than a certain threshold, set here to be 0.1, on the same lattice site. The segregation index is then defined by

$$SI = \left\langle \frac{n}{n + \bar{n}} \right\rangle, \tag{4.5}$$

where $n$ is the number of neighbours of a cell with the same activity, $\bar{n}$ is the

number of neighbours of a cell with opposite activity and the average is taken over all cells. With our choice of parameters, the phase-field cells are stable and have sharp interfaces so no spurious neighbour pairs are identified.

The segregation index for a 1:1 mixture is plotted in Figure 4.5 (a). The microphase separation proceeds quickly after the onset of dipolar activity at $t = 0$ but then slows. It is unclear from the data whether microphase separation is arrested or continues over very long time scales, since the $SI$ appears to saturate at late times.

An alternative measure of phase separation is the density autocorrelation function

$$C_\zeta(\mathbf{r}) = \langle \rho_\zeta(\mathbf{x}) \rho_\zeta(\mathbf{x}+\mathbf{r}) \rangle - \langle \rho_\zeta(\mathbf{x}) \rangle \langle \rho_\zeta(\mathbf{x}+\mathbf{r}) \rangle \tag{4.6}$$

where the density field $\rho_\zeta$ for the subset of cells in the system with $\zeta_{\text{inter}} = \zeta$ is defined by

$$\rho_\zeta(\mathbf{x}) = \sum_{i:\zeta_{\text{inter},i}=\zeta} \phi_i(\mathbf{x}). \tag{4.7}$$

Figure 4.5 (b) shows the moving average of the lengthscale of the density autocorrelation $\rho_\zeta$, taken over $10^4$ timesteps. Recalling that each cell has a nominal diameter $\sim$16 lattice units, the length scale of the density autocorrelation is initially roughly one cell, consistent with a well-mixed monolayer, while the length scale at long times increases to slightly more than 4 cells, consistent with microphase separation into clusters roughly 4 cells wide. These results demonstrate quantitatively that the mixture of extensile and contractile cells sorts according to activity. The data suggest that the cluster size saturates, but we cannot rule out a continued extremely slow growth of the clusters. Figure 4.6 provides a comparison of $SI$ and $C(r)$ for the fully sorted system illustrated in Figure 4.2 (c), (d). The segregation index remains close to 1 at all times and, although some structure develops in the nematic phase of contractile cells, the lengthscale of the clustering remains unchanged.

The segregation index and density autocorrelation indicate microphase separation but yield no information about the dynamics of the system. We next examine the mean-square displacement of the phase-field cells, comparing the fully phase-separated state in Figure 4.2 (d) to the microphase-separated state Figure 4.2 (b).

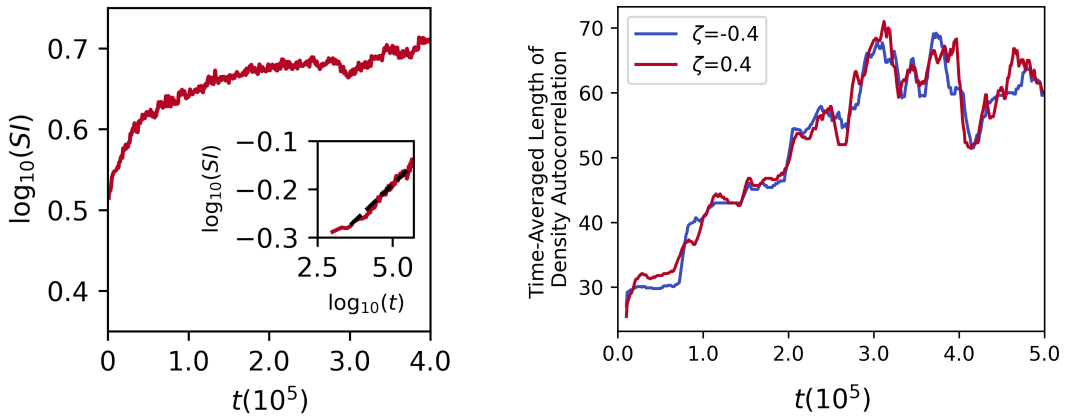


**Figure 4.5:** Segregation in a 1:1 mixture of extensile and contractile cells. (a) Segregation index $SI$ versus time. The onset of segregation is on a timescale $t = \mathcal{O}(10^3)$. The $SI$ increases past $\sim 0.7$ on the timescale of the simulation; the inset showing $SI$ on log-log axes indicates the system coarsens steadily. (b) Time-averaged correlation length of $\rho_\zeta$ for extensile and contractile cells in the simulation illustrated in Fig. 4.2 (a) and (b). The correlation length grows up to $t \approx 3 \times 10^5$, then appears to saturate on a scale commensurate with the diameter of $\sim 4$ cells.

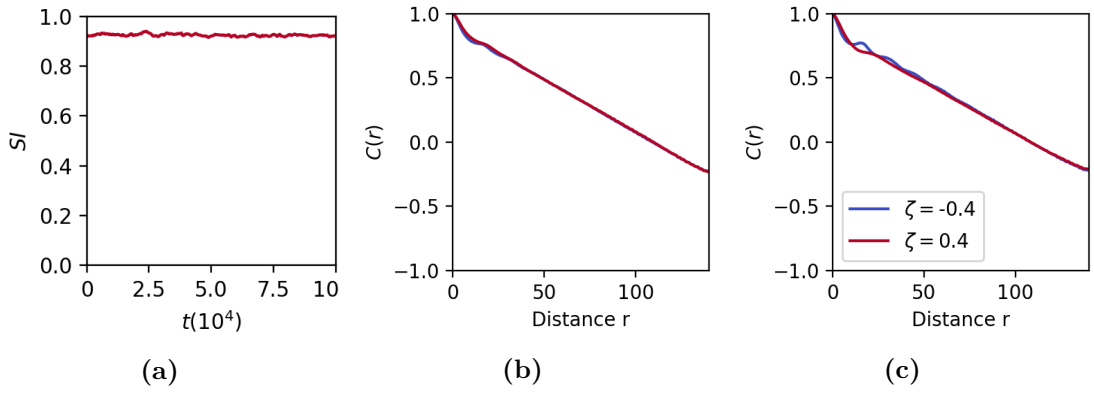


**Figure 4.6:** Order in a system prepared in a $1:1$ macrophase-separated initial condition, with $\zeta_{\text{inter}} = \pm 0.4$, illustrated in Figure 4.2 (c) and (d). (a) Segregation index $SI$. Aside from small fluctuations, the $SI$ remains high because almost all cells are entirely surrounded by neighbours of the same type. In addition, density autocorrelation function $C(r)$ at time (b) $t = 5 \times 10^2$ (c) $t = 1 \times 10^5$. The system evolves small-scale structure as the contractile cells organise into a nematic phase, but the density correlation length remains commensurate with half the system size.

Results for the phase-separated configuration shown in Figure 4.7 (a) indicate that, when surrounded by cells of the same type, the motion of the contractile cells is almost entirely arrested, while extensile cells move more freely. This is true also in pure monolayers: Figure 4.8 shows plots of mean-square displacement for homogeneous monolayers of extensile and contractile cells. This is a result of the different intercellular interactions due to the active dipolar forces. Contractile cells elongate and align to form a solid-like, nematic configuration. Extensile cells prefer to lie at right angles to one another, which leads to frustration and gives configurations that fail to form system-scale flows, as observed in Chapter 6. However, pairs of extensile cells which lie perpendicular to each other have a polarity which results in net migration [100].

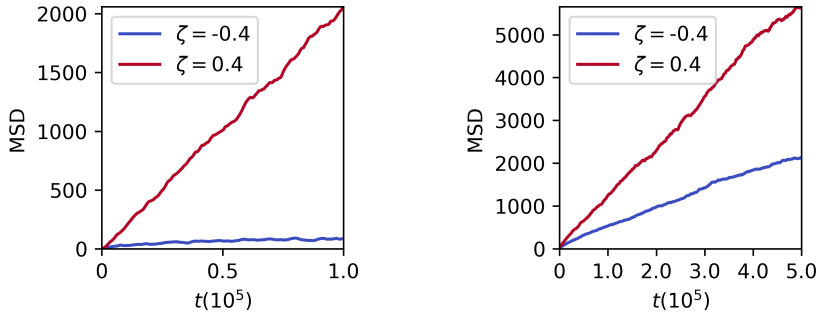


**(a)** **(b)**

**Figure 4.7:** Mean-square displacement for contractile (blue) and extensile (red) cells in (a) a 1 : 1 phase separated monolayer (Fig. 4.2 d) and (b) a 1 : 1 microphase-separated state (Fig. 4.2 b). When the cells are completely phase separated, the extensile cells rearrange freely while contractile cells do not. As a result, extensile cells diffuse three orders of magnitude as quickly as contractile cells. In the microphase-separated state, however, the presence of contractile cells slows the diffusion of extensile cells, which in turn push the contractile cells around the system. The MSD has not saturated by $t = 5 \times 10^5$, which indicates that the clusters are still evolving and rearranging.

In the microphase separated system the diffusion of contractile cells is enhanced and that of extensile cells reduced, as shown in Fig. 4.7 (b). This is because the less motile, solid-like clusters of contractile cells constrain the paths of extensile cells, while the extensile cells tend to push the contractile cells around the simulation domain. As part of the diffusion, individual extensile cells are able to squeeze between contractile clusters from one extensile cluster to another. Given the

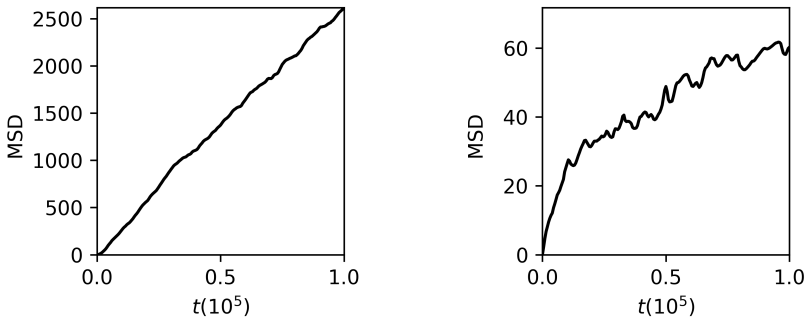


**(a)** **(b)**

**Figure 4.8:** Mean-square displacement of bulk (a) extensile cells with $\zeta_{\text{inter}} = +0.4$ and (b) contractile cells with $\zeta_{\text{inter}} = -0.4$. The extensile cells are fluidised while the motion of the contractile cells is arrested.

apparent saturation of the $SI$ and the density autocorrelation lengthscale at long times, the system may be entering a dynamic steady state. It is unclear whether the layer can sort completely, as in Figure 4.2 (d), at much longer times.

Taking the diffusion constant in the system to be that of the extensile cells, $\langle \mathbf{x}^2 \rangle_{\zeta=+0.4} = 4Dt$, the timescale associated with diffusion is $\tau_D = R^2/D \sim 10^4$. Madin-Darby Canine Kidney cells migrate on the order of 10 microns per hour [37], which is on the order of a cell diameter. The diffusion timescale in the $1:1$ mixed system suggests that $1 \times 10^5$ timesteps *in silico* corresponds to order a day of real time, which is the duration of the experiments of Balasubramaniam et al. [39].

We note that differential diffusivity has been shown to sort otherwise passive soft particles [117], even at high packing fractions [118]. Here, extensile cells are akin to hot particles and contractile cells to cold ones. Weber, Weber and Frey [117] attribute the phase separation in a mixture of particles at two different temperatures to an effective attraction between cold particles; here the active forces act to attract the contractile cells into more coherent clusters.

### 4.3.2 Free Energy

In systems that sort, there is often a thermodynamic basis for the phase separation. Consequently, we investigate whether the clustering is associated with any changes

in the total free energy of our model, Equations 2.9. For the microphase separated system (Fig. 4.2 a,b), the mean and standard deviation of the total free energy per cell from times $t = 1 \times 10^3$ to $t = 5 \times 10^5$ are listed in Table 4.1. As a comparison, data for the system with phase-separated initial condition (Fig. 4.2 c,d) from times $t = 1 \times 10^3$ to $t = 1 \times 10^5$ are also listed. In both cases, the times run from shortly after the turning on of dipolar active stresses to the end of the simulation. The free energy shows no dependence on time or, indeed, cluster size, suggesting the cell sorting is not thermodynamic in origin, and may instead be caused by the differences in diffusivity described above.

| | Microphase-Separated | | Sorted | |
|---|---|---|---|---|
| $t$ | $\bar{\mathcal{F}}_{\text{tot}}$ | $\sigma_{\mathcal{F}}$ | $\bar{\mathcal{F}}_{\text{tot}}$ | $\sigma_{\mathcal{F}}$ |
| $1 \times 10^3$ | 39.99 | 4.783 | 38.10 | 2.372 |
| $1 \times 10^4$ | 38.87 | 3.803 | 38.96 | 2.318 |
| $5 \times 10^4$ | 38.88 | 3.824 | 39.19 | 4.028 |
| $1 \times 10^5$ | 38.78 | 3.628 | 38.71 | 3.041 |
| $5 \times 10^5$ | 38.95 | 3.855 | x | x |

**Table 4.1:** Mean $\bar{\mathcal{F}}_{\text{tot}}$ and standard deviation of free energy per cell for the microphase-separated state (Fig. 4.2 a,b) and the sorted state (Fig. 4.2 c,d) over time, starting at $t = 1 \times 10^3$, shortly after activity is turned on. The clustering of the phase fields over time is not associated with a reduction in free energy at long times, in contrast to phase separation according to mechanisms such as differential adhesion.

We also characterise the effective surface tension of the phase-separated clusters. Given the total energy per cell of contractile and extensile cells in pure monolayers, we can estimate the total free energy of a monolayer comprising arbitrary numbers of contractile and extensile cells by

$$\hat{\mathcal{F}} = \bar{\mathcal{F}}_{+} n_{+} + \bar{\mathcal{F}}_{-} n_{-} \tag{4.8}$$

where $+$ and $-$ indicate extensile and contractile cells respectively, and $\mathcal{F}_{+}$ and $\mathcal{F}_{-}$ the corresponding average energy per cell $\bar{\mathcal{F}}_{\text{tot}}$ in a pure monolayer, taken from Table 4.2. We compare the estimate with the actual energy of a monolayer in a coexistence state *in silico*, yielding a difference

$$\Delta\mathcal{F} = \mathcal{F}_{\text{tot}} - \hat{\mathcal{F}}. \tag{4.9}$$

| | $\zeta$ | $\bar{\mathcal{F}}_{\text{tot}}$ | $\sigma_{\text{tot}}$ |
|---|---|---|---|
| Active | 0.4 | 40.65 | 0.144 |
| | -0.4 | 37.18 | 0.0669 |
| Passive | 0.0 | 35.37 | 0.0979 |

**Table 4.2:** Free energy per cell for active extensile and contractile cells, and passive cells, in homogeneous monolayers; the source of $\bar{\mathcal{F}}_+$ and $\bar{\mathcal{F}}_-$ used to find the effective line tension in a coexistence state. The active layers, both extensile and contractile, have higher free energy per cell than a passive monolayer. These data are used to estimate $\hat{\mathcal{F}}$ in Equation (4.8).

The effective cluster line tension is then $\Lambda = \Delta\mathcal{F}/L_{\text{interface}}$, where the interface length $L_{\text{interface}}$ depends on the size of the system and the relative number fraction of extensile or contractile cells in the system. For coexistence states prepared as a circular cluster of one extensile (contractile) cells in a contractile (extensile) background, the interface length is $L_{\text{interface}} \approx 2L\sqrt{\Phi\pi}$ where $\Phi$ is the number fraction of the minority component in the system.

Table 4.3 lists, for various number fractions of extensile cells (all in systems with $N = 336$ total cells), the estimated total monolayer free energy, $\hat{\mathcal{F}}$, the actual monolayer free energy $\mathcal{F}_{\text{tot}}$ and the difference between the two, $\Delta\mathcal{F}$. In addition, the table specifies the interface length $L_{\text{interface}}$ and the effective line tension $\Lambda$ in the system, which is shown not to be constant. Note there are two ways to make a circular cluster with a $1:1$ ratio of extensile to contractile cells: an extensile cluster inside a contractile background, and vice versa, as pictured in Figure 4.9. An extensile cluster has a larger energy than a contractile one when both are prepared in a $1:1$ system. This phenomenon results from the differences in ordering in contractile and extensile cells.

Contractile cells tend to exhibit nematic alignment. When contractile cells form a cluster, the nematic alignment results in an effective attraction between the contractile cells that stabilises their cluster. Similarly, when contractile cells form the bulk of a system, the nematic alignment wraps around the edge of the periodic boundary condition, as illustrated in Figure 4.9 (a); this system-scale order results in a line tension along the line of contractile cells that balances against any active

| Extensile fraction $\Phi$ | $\hat{\mathcal{F}}$ | $\mathcal{F}_{\text{tot}}$ | $\Delta\mathcal{F}$ | $L_{\text{interface}}$ | $\Lambda$ |
|---|---|---|---|---|---|
| 0 | 12492.48 | 12492.48 | 0 | x | x |
| ≈0.1 | 12610.46 | 12632.92 | 22.46 | 315.74 | 0.071 |
| 0.25 | 12783.96 | 12936.34 | 152.38 | 496.29 | 0.31 |
| 0.5 | 13075.44 | 13336.80 | 261.36 | 701.86 | 0.37 |
| 0.5 | 13075.44 | 13049.08 | -26.36 | 701.856 | -0.038 |
| 0.75 | 13366.92 | 13368.61 | 1.688 | 496.29 | 0.0034 |
| ≈0.9 | 13540.42 | 13560.74 | 20.32 | 315.74 | 0.064 |
| 1.0 | 13658.40 | 13658.40 | 0 | x | x |

**Table 4.3:** Effective line tension $\Lambda$ for circular extensile clusters in contractile background ($\Phi = 0, \ldots, 0.5$) and contractile clusters in an extensile background ($\Phi = 0.5, \ldots, 1.0$). As the extensile cluster grows, the effective line tension grows; however, as the contractile cluster grows, the effective line tension decreases. Compared to the estimated monolayer energy $\hat{\mathcal{F}}$, contractile clusters are more stable than extensile clusters. Both these effects result from the active contractile stress along a connected line of contractile cells.

pressure due to an extensile cluster in the system. On the other hand, the more diffusive extensile cells, which exhibit order on much shorter length scales, create an active pressure against the contractile cells, which constrain them.

The fact the purported line energy $\Lambda$ is not constant with the size of the clusters, and that the free energy does not decrease as extensile clusters grow, shows that line tension does not provide a thermodynamic basis for sorting an active mixture. This is not surprising, as surface tension has been shown previously not to be well defined, and even to depend on interface curvature, in active systems [119]. These results do show, however, that contractile cells cluster while extensile cells do not; any 'clustering' that extensile cells exhibit is to occupy space in the domain that is left over by the solid-like domains of contractile cells.

### 4.3.3 Failure to Order

Thus far, we have considered mixtures of extensile and contractile cells, with $\zeta_{\text{inter}} = +0.4, -0.4$. It is possible, in addition, to examine active-passive systems. An extensile-passive system, with $\zeta_{\text{inter}} = +0.8, 0.0$, fails to phase separate. Such a system is pictured in Figure 4.10, while the SI and density autocorrelation are pictured in Figure 4.11. Unlike contractile cells, which form a solid-like phase,

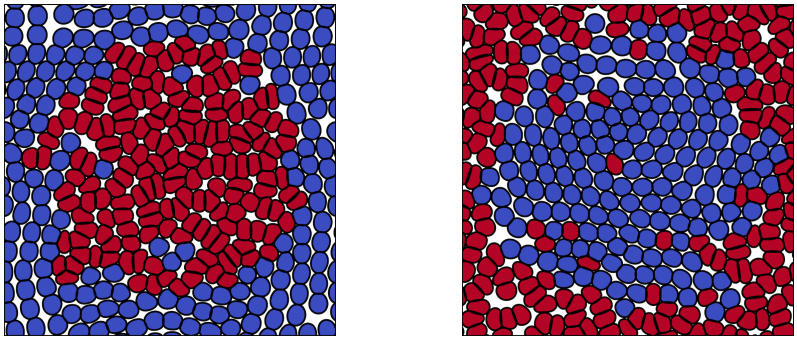

**(a)** **(b)**

**Figure 4.9:** Two ways to form a sorted 1 : 1 cluster using a circular geometry. (a) An extensile cluster (red) in a contractile background (blue), with a large difference $\Delta\mathcal{F}$ between the system free energy $\mathcal{F}_{\text{tot}}$ and the estimate $\hat{\mathcal{F}}$. (b) A contractile cluster (blue) in an extensile background (red) with a small negative $\Delta\mathcal{F}$. Note contractile cells organise in parallel lines, while extensile cells make small groups that are isotropic on long lengthscales. The higher-energy configuration in (a) results from the higher diffusivity of extensile cells creating an active pressure, along with the long chains of contractile cells creating a line tension on the edge of the extensile cluster.

passive cells by definition have no active interactions *via* which to coalesce, and therefore do not cluster: observe the empty space in Figure 4.10 (b) compared to Figure 4.2 (b) and (d). Because the passive cells do not cluster, the extensile cells are able to invade groups of passive cells and there is no complementarity between one species of cells forming a solid-like background and the other species migrating around the remaining free space.

In addition, a contractile-passive system, with $\zeta_{\text{inter}} = -0.8, 0.0$, fails to phase separate. In this system, pictured in Figures 4.12 with SI and density autocorrelation graphed in Figure 4.13, contractile cells are not able substantially to deform each other and the geometry remains frustrated. Also, there is no differential diffusivity between contractile and passive cells. In this system, any randomly-initialised patches of contractile cells adopt a nematic configuration, while any passive cells not subject to contractile stresses remain isotropic. The failure of a mixture of active and passive cells to phase separate is consistent with simulations of active Brownian particles mixed with passive particles [120].

Finally we mention intracellular dipolar activity $\zeta_{\text{self}} \neq 0$. The evolution of a system with $\zeta_{\text{self}} = \pm 0.4$ is shown in Figure 4.14, and the extensile cells are

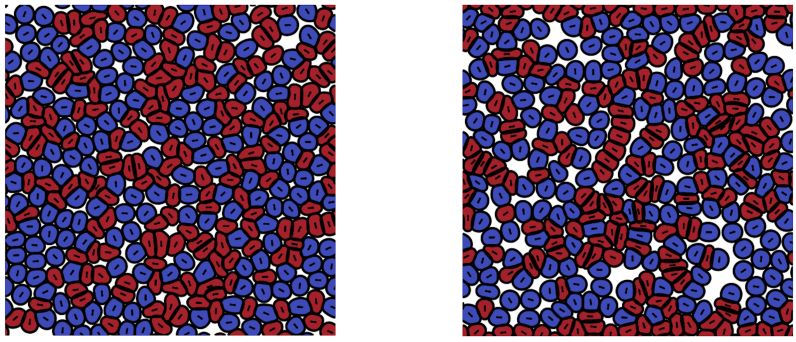

(a) (b)

**Figure 4.10:** Evolution of a 1 : 1 mixture of extensile (red, $\zeta_{\text{inter}} = +0.8$) and passive (blue, $\zeta_{\text{inter}} = 0.0$) cells. In this simulation, the difference in $\zeta_{\text{inter}}$ between the constituents of the mixture is the same as in the main text, which concerns $\zeta_{\text{inter}} = +0.4, -0.4$. System visualised at (a) $t = 5 \times 10^2$, (b) $t = 1 \times 10^5$ for a fully mixed initial condition showing no microphase separation. The system remains mixed for the duration of the simulation, although some transient structures of order one cell width do emerge.

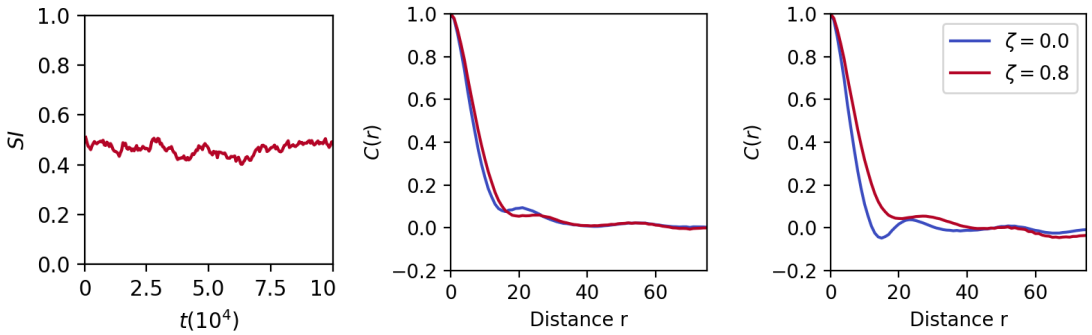


(a) (b) (c)

**Figure 4.11:** Failure to order in a 1 : 1 mixture of extensile ($\zeta_{\text{inter}} = +0.8$) and passive ($\zeta_{\text{inter}} = 0.0$) cells. (a) Segregation index $SI$. Over time, the $SI$ fluctuates around a value close to 1/2. Also, density autocorrelation $C(r)$ at time (b) $t = 5 \times 10^2$ and (c) $t = 1 \times 10^5$. Over the course of the simulation, the locations of the minima do not change although they do get more pronounced. These metrics do not resolve transient chains of extensile and contractile cells that form and re-form during the simulation.

clearly deformed into elliptical spindle shapes. In addition, as observed in [100], values of $\zeta_{\text{self}}$ and $\zeta_{\text{inter}}$ with the same sign tend to cancel. This reduction in effective activity reduces the diffusivity of the active phase-field cells and slows sorting, as shown in Figure 4.15.

There is no bulk thermodynamic effect that results in sorting, and in particular there is no sorting induced by a line tension between contractile and extensile clusters. We observe the tendency of contractile cells to align nematically, which

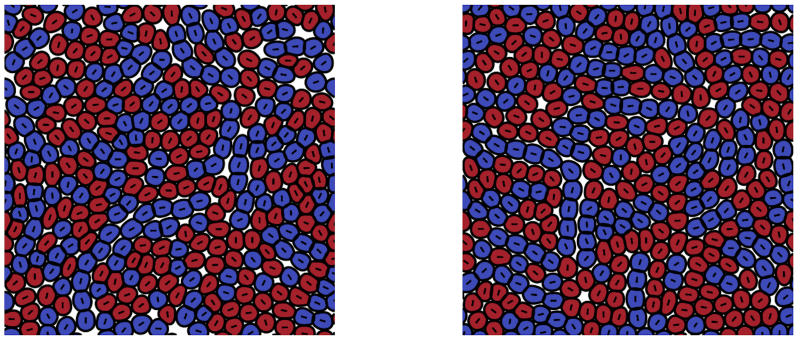

**(a)** **(b)**

**Figure 4.12:** Evolution of a $1:1$ mixture of passive (red, $\zeta_{\text{inter}} = 0.0$) and contractile (blue, $\zeta_{\text{inter}} = -0.8$) cells. In this simulation, the difference in $\zeta_{\text{inter}}$ between the constituents of the mixture is the same as in the main text, which concerns $\zeta_{\text{inter}} = +0.4, -0.4$. System visualised at (a) $t = 5 \times 10^2$, (b) $t = 1 \times 10^5$ for a fully mixed initial condition showing no microphase separation. The system remains mixed for the duration of the simulation.

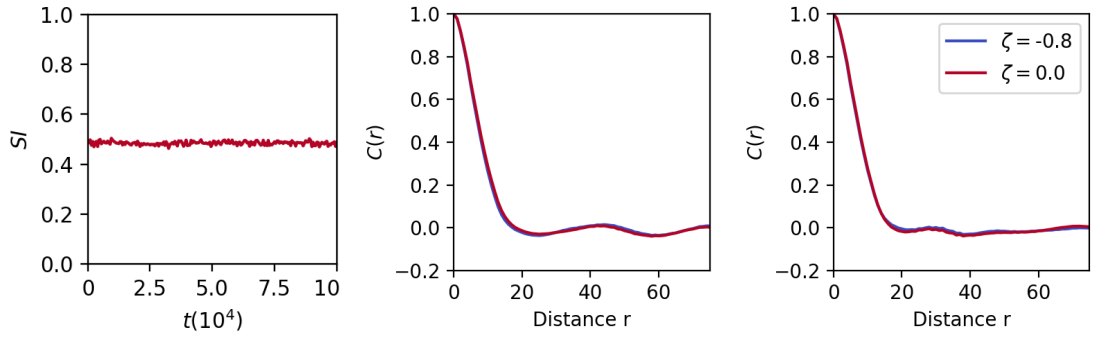


**(a)** **(b)** **(c)**

**Figure 4.13:** Failure to order in a $1:1$ mixture of passive ($\zeta_{\text{inter}} = 0.0$) and contractile ($\zeta_{\text{inter}} = -0.8$) cells. (a) Segregation index $SI$. Over time, the $SI$ fluctuates around a value close to $1/2$. Density autocorrelation $C(r)$ at times (b) $t = 5 \times 10^2$ and (c) $t = 1 \times 10^5$. The length scale of the system in fact *shrinks* slightly: the disordered initial condition evolved into a packing that is close to ordered, although the system does not demix.

results in an active stress that stabilises their clusters. In addition, this system exhibits hallmarks of differential diffusion, which has been shown by Weber, Weber and Frey [117] and McCarthy et al. [118] to result in active phase separation via an effective attraction between cold particles.

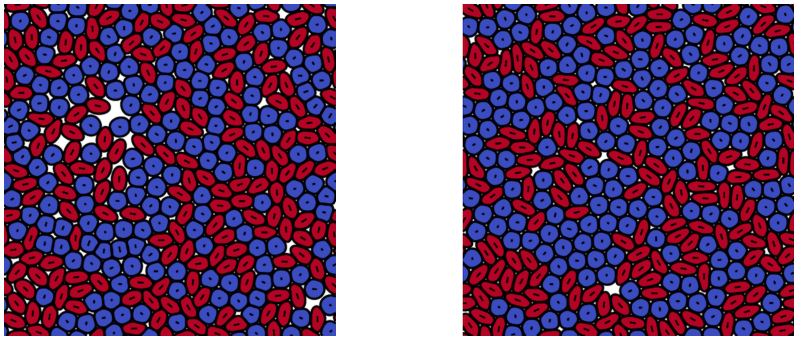

(a) (b)

**Figure 4.14:** Evolution of a 1 : 1 mixture of extensile and contractile cells with $\zeta_{\text{self}} = \zeta_{\text{inter}} = \pm 0.4$. System visualised at (a) $t = 5 \times 10^2$, (b) $t = 1 \times 10^5$ for a fully mixed initial condition. The extensile cells become spindle-shaped, and the self-induced activity competes with the intercellular activity.

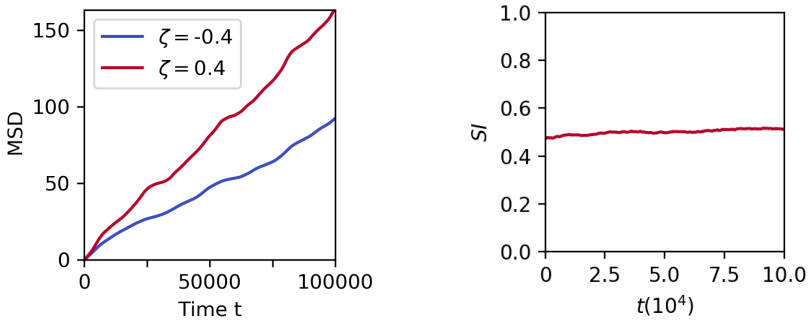


(a) (b)

**Figure 4.15:** Mean-square displacement (a) and segregation index (b) for a 1 : 1 mixture of extensile and contractile cells, with $\zeta_{\text{self}} = \zeta_{\text{inter}} = \pm 0.4$. The diffusion is slowed down by a factor of five compared to Figure 4.7, and there is a concomitant slowing-down in the segregation index, because active dipolar forces where $\zeta_{\text{self}}$ and $\zeta_{\text{inter}}$ have the same sign tend to cancel out.

## 4.4 Discussion

There is considerable experimental evidence of sorting of different cell types both *in vitro*, in confluent cell layers [39, 106, 107, 112, 116] or cellular spheriods [109], and in vivo, for example during morphogenesis [11, 111]. Many different physical factors are candidates for driving the sorting. Without doubt equilibrium effects, such as the dependence of cell-cell adhesion or line tension of cell-cell junctions on different cell neighbours, can lead to ordering akin to thermodynamically-driven phase ordering in liquid-liquid mixtures [54, 110, 114]. However, biological systems

are naturally out of equilibrium, and it has also been suggested that different forms of activity can result in the sorting of different cell types [39, 121]. Balasubramaniam et al. in particular showed that cells with a mixture of extensile and contractile force dipoles are able to phase separate on short length scales [39].

Isolating the different contributions to cell sorting is difficult in experiments, but easier in the context of computational models of cell motility. Therefore in this Chapter we use a multi-phase field model of a confluent cell layer to study the influence of dipolar active interactions between neighbouring cells on cell sorting. We demonstrate that a mixture of extensile and contractile active dipolar cells, which are otherwise identical, can undergo partial sorting. We interpret this as an out-of-equilibrium effect resulting from the different dynamics of the two cell populations. Extensile cells are smaller and more motile whereas contractile cells tend to elongate and form static, solid-like nematic patches. The differential diffusivity is insufficient to explain the phase separation, as mixtures of extensile and passive cells fail to phase separate. We suggest that the solid-like active clustering of the contractile cells is essential to the microphase separation. We caution, however, that both the microphase separated state and a fully sorted state are stable on the timescale of the simulations, and it is unclear whether further coarsening will occur on times we cannot access.

Any model of cell mechanics must still be viewed with caution as there are still many questions about the model details needed to faithfully reproduce the cells' interactions and dynamics. Here we have focussed on forces, mediated by adherens junctions between cell cortices, that act across cell-cell boundaries, which we have modelled as balanced dipolar forces. However, fluctuating polar forces [122] or active forces which act along cell-cell junctions [115] may be relevant, as may apical-basal asymmetry if a monolayer is modelled in three dimensions [123]. The fact that contractile cells in the bulk, as well as in the clusters in this Chapter, are unable to intercalate prompts us to consider how to fluidise an epithelial monolayer. In the next Chapter, we implement fluctuations in the adhesions at junctions between cells to drive the monolayer, and thereby recover T1 topological transitions.

*'Twas brillig, and the slithy toves*
*Did gyre and gimble in the wade;*
*All mimsy were the borogroves,*
*And the mome raths outgrabe*

— Lewis Carroll [2]

# 5 Monolayer Fluidisation by Adhesion Fluctuations

## 5.1 Introduction

The membranes of epithelial cells are joined together by cadherin proteins at adherens junctions [21, 27]. These membrane proteins are embedded in the actomyosin cortex that provides a substructure to stabilise the lipid bilayer membrane, while continuously turning over and remodelling. Adherens junctions fluctuate in number and type, as junctions are created when the protein $\alpha$-catenin binds cadherin to the actomyosin cortex [124], and cells can modulate which of several types of cadherin they prefentially express [125]. Cadherin switching is implicated in the epithelial-mesenchymcal transition (EMT) and cancer metastasis [125], and changes in adherens junctions permit the rearrangement of cells within a monolayer [8]. These changes, including the recruitment of actomyosin to adherens junctions and number fluctuations of those junctions, can fluidise an epithelial monolayer by promoting neighbour exchange via T1 topological transitions, or else anneal topological defects in a tissue [126]. Membrane processes therefore have implications for tissue fluidisation and, consequently, processes that rely on tissue migration, such as morphogenesis and tumour invasion, and this motivates our focus on fluctuating adherens junctions.

The cellular vertex model has previously been used to demonstrate tissue fluidisation through junctional tension fluctuations and such fluctuations have even been implicated in sorting [54, 127]. In this work we seek to model junctional fluctuations in a multi-phase field model in order to fluidise an epithelial monolayer.

## 5.2 Model

The phase-field model used in this chapter closely matches that detailed in Chapter 2. The dynamics are given by Equation (2.1) in conjunction with the overdamped force balance of Equation (2.2). The passive dynamics are controlled by four free energy densities: the Cahn-Hilliard and area conservation terms in Equation (2.4), and the repulsion term in Equation (2.6a). We model junctional fluctuations using a driven adhesion free energy functional, wherein lies the largest difference between this version of the model and the description in Chapter 2. The functional form of this adhesion free energy is

$$\mathcal{F}_{\text{adh}} = \sum_i \sum_{j \in N_i(t)} \lambda \int \mathrm{d}\mathbf{x}\, \omega_{ij} \nabla \varphi_i^2(\mathbf{x}) \cdot \nabla \varphi_j^2(\mathbf{x}), \tag{5.1}$$

which follows the form in Equation (2.6b), with two modifications. The sum over $j$ includes only those cells $j$ that are current neighbours of cell $i$; that is, they are in the set of neighbours $N_i$ at time t. Also, the adhesion parameter $\omega$ is promoted from a single constant to a pairwise $\omega_{ij}$ for interactions between neighbouring cells $i$ and $j$, which permits different pairs of cells to adhere more or less strongly than others. A positive sign for $\omega_{ij}$ will favour lengthening the interface between membranes, whereas a negative sign will favour shortening said interface. This is because the gradients of the squares of neighbouring phase fields necessarily point in opposite directions; that is, their inner product is negative. Negative values of $\omega_{ij}$ are analogous to the line tension of cellular vertex models, although junctional line tension is less well-defined a concept in phase-field models.

This formulation of the adhesion free energy functional differs from those of other works [67, 128] in two key ways. Firstly, here we calculate the free energy using the gradients of the *squares* of the phase fields to ensure the theory is local:

at each lattice site, the functional derivative of $\mathcal{F}_{\text{adh}}$ that appears on the right-hand side of Equation (2.1) is proportional to $\varphi_i(\mathbf{x})$ so that phase-field material cannot emerge spontaneously at a distance from the bulk of a cell. This aids the model's stability when adhesion is large. Secondly, other works have considered a single energy scale $\omega$ for all adhesive interactions, while here we have a set of pairwise $\omega_{ij}$.

The pairwise adhesion energy scales $\omega_{ij}$ are the avenue through which we introduce neighbour-neighbour fluctuations to the model in order to fluidise a layer of phase-field cells. The adhesion free energy becomes a functional not only of the $\varphi_i$ but also of the $\omega_{ij}$. We demand symmetry in the energy scales, $\omega_{ij} = \omega_{ji}$, so that the pairwise interactions of neighbour cells are reciprocal. A simple model for fluctuations, previously used in vertex models [54, 126, 129], is a resetting Ornstein-Uhlenbeck process:

$$\frac{\mathrm{d}\omega_{ij}}{\mathrm{d}t} = -\frac{1}{\tau_\omega}(\omega_{ij} - \bar{\omega}) + \sqrt{\frac{2\sigma_\omega^2}{\tau_\omega}}\eta_{ij}; \tag{5.2a}$$

$$j \notin N_i(t) \implies \omega_{ij}(t) = 0 \tag{5.2b}$$

where the $\eta_{ij}$ are uncorrelated white noise with zero mean and unit variance, $\langle \eta_{ij}(t) \rangle = 0$, $\langle \eta_{ij}(t)\eta_{kl}(t') \rangle = \delta_{ik}\delta_{jl}\delta(t - t')$. Each pairwise $\omega_{ij}(t)$ then evolves as an Ornstein-Uhlenbeck process while the $i, j$ neighbour pair exists and is set to zero otherwise. Setting $\omega_{ij} = 0$ models the absence of cadherin proteins between the respective cells, since no junction exists.

At long times, then, the pairwise energy scales $\omega_{ij}(t)$ form an equilibrium distribution with mean $\bar{\omega}$ and variance $\sigma_\omega^2$. The persistence time $\tau_\omega$ and the standard deviation $\sigma_\omega$ are the key control parameters for the driven free energy landscape given by $\mathcal{F}_{\text{adh}}[\{\omega_{ij}\}]$, which consequently is sampled from an equilibrium distribution, and cause a multi-phase-field monolayer to evolve in search of local free energy minima. There are no active polar or dipolar forces whatsoever in this version of the multi-phase field model.

The parameters assigned to the free energy terms in Equations (2.4) and (2.6a) are $\gamma = 1.4$, $\lambda = 2.0$, $\mu = 120$, and $\kappa = 1.5$. The mean value of the adhesion parameter in Equation (5.2) is $\bar{\omega} = 0$. The coefficient of friction at the substrate is

$\xi = 3.0$ and the target cell area is given by radius $R = 8.0$. Relaxation according to Equation (2.1) is controlled by the parameter $J_0 = 1 \times 10^{-2}$ and occurs with a timescale $\tau_0 = (\gamma h J_0)^{-1} = \mathcal{O}(10^2)$.

We simulate twenty-five phase-field cells for $T = 2 \times 10^5$ timesteps. The cells are initalised in a hexagonal lattice on a rectangular domain with side lengths $L_x = 75$ and $L_y = 65$ lattice units. The multi-phase field model is implemented with periodic boundary conditions. The system is initiated by placing cells in the hexgonal lattice and then relaxing them without fluctuations ($\omega_{ij} = 0$) up to time $t = 5 \times 10^3$, at which point the adhesion fluctuations are turned on and data recorded. The dynamical equations are solved using a one-step predictor-corrector scheme. The unit of time is 1, and each step is divided into five substeps.

## 5.3 Results

### 5.3.1 Monolayer Fluidisation

An epithelial monolayer can change its topology through several processes, such as cell division and extrusions [32, 123, 130, 131]. Fluidisation of a tissue through fluctuating tensions or adhesions at cell-cell junctions relies on cell intercalations (i.e., T1 transitions) that are able to modify neighbour-neighbour contacts [115, 130, 132]. During a T1 transition, the junction between one pair of cells shrinks and a new junction forms between another previously unconnected pair of cells. Each of the two cells that were neighbours before the transition loses one neighbour, while each of the two cells that are neighbours after the transition gains one.

This process is illustated in Figure 5.1, which highlights four cells in an adhesive background. In (a), the cells outlined in red are stuck together by a large positive $\omega_{ij} = +1.0$, while all other pairwise adhesions are given by $\omega_{ij} = 0.4$. The adhesion parameter for the red cells is then set to $\omega_{ij} = -10$ so that the cells are pushed apart in (b). The cells transition through the equivalent of a fourfold vertex until the cell intercalation is completed in (c). Note that the topological transition of the coloured cells is accompanied by additional neighbour rearrangements in the wider monolayer. This initial assay shows that in our model, assuming a

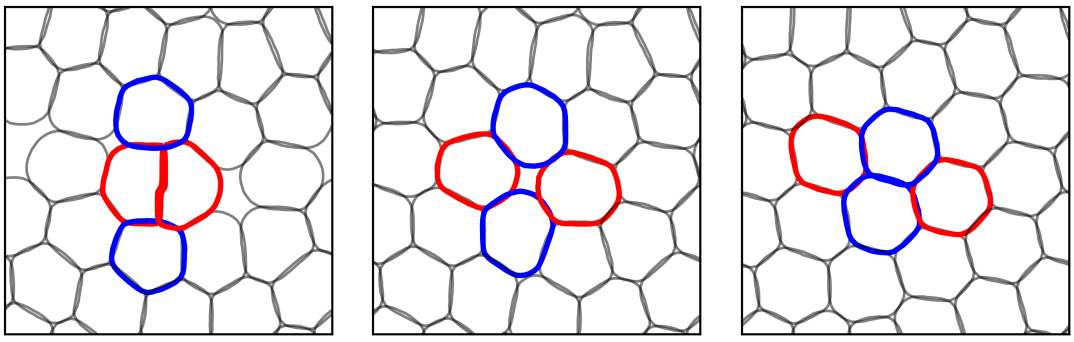

(a) (b) (c)

**Figure 5.1:** A quartet of cells (a) before, (b) during, and (c) after a T1 topological transition in an adhesive background. The red cells at first attract with $\omega_{ij} > 0$ (a) and then repel with $\omega_{ij} < 0$ (b), while the blue cells attract with $\omega_{ij} > 0$ to complete the transition (c). Each cell outlined in red loses a neighbour and each cell outlined in blue gains a neighbour, for a neighbour change quantity of 4. This process requires a change in $\omega_{ij} = \mathcal{O}(10^1)$ and takes $\mathcal{O}(10^4)$ timesteps to complete, setting a scale for $\sigma_\omega^2$ and $\tau_\omega$ in the Ornstein-Uhlenbeck process (5.2). The change in monolayer geometry due to the highlighted T1 transition is accommodated by the presence of additional rearrangements in the monolayer.

monolayer with otherwise uniform $\omega_{ij}$, a quartet of cells requires a local difference $\Delta\omega_{ij} = \mathcal{O}(10^1)$ to effect a T1 transition. This estimate sets an approximate variance $\sigma_\omega^2$ for the random process in Equation (5.2). In addition, it takes $\mathcal{O}(10^4)$ timesteps for the T1 transition illustrated in Figure 5.1 to occur, setting an approximate relaxation timescale $\tau_\omega$ for Equation (5.2).

It has been observed that the migration of cells in dense monolayers requires coordination between neighbouring cells and the subcellular processes of protrusion, adhesion, contraction, and retraction that control individual cell motility [19, 133]. It is clear that in order to minimise geometric frustration in the layer, the rearrangement of cells through the fourfold vertex in Figure 5.1 requires cell rearrangements in the larger monolayer, via coordination with another T1 transition at an additional fourfold vertex or vertices. The parameter $J_0$ certainly affects the rate at which the layer geometry can relax *via* multiple topological transitions, as $J_0$ acts to rescale time in the model: the larger its value, the faster any T1 transitions occur.

The parameters $\gamma$ and $\kappa$, meanwhile, control the cell line tension and cell-cell repulsion, respectively, and appear to have an effect on the timescale of a T1

transition in the monolayer. The relative values of these parameters control whether cells tend to overlap or to deform, and are intimately connected with a rigidity transition or unjamming in the layer in conjunction with polar activity [67, 134, 135]. However, the absolute values of these parameters also control the behaviour of the layer: $\gamma$ and $\kappa$ are increased together, the cells become both harder and more rigid. In this limit, the layer approaches a random close packing of circles and questions of initial condition and geometry have implications for the possibility of cell rearrangements, and whether the system is jammed [136].

In addition, the adhesion difference $\Delta\omega_{ij}$ used in the assay to obtain a large negative $\omega_{ij}$ effects a repulsion that competes not only with $\kappa$ but also with adhesion mediated by the background $\omega$. A larger value of $\Delta\omega_{ij}$, as well as a larger background $\omega$, tends to form a larger gap between cells, such as between those indicated in red in Figure 5.1. In addition, a smaller $\kappa$ can promote T1 transitions not only by making it easier to open up the gap between cells, but also by allowing cells to overlap to fill the gap more easily. However, it is possible, especially with a sufficiently large value of $\omega$ compared to $\gamma$, for the layer to relax to a configuration in which the T1 transition is not resolved.

It is not guaranteed that a given layer geometry can relax at all, and this observation is connected to the notion of a rigidity transition [67, 134], jamming [136], and glassy behaviour in epithelial monolayers [133]. However, an investigation into these topics is beyond the scope of the present Chapter. We use a hexagonal lattice of cells as an initial condition to control for any possible effects due to randomly seeding the domain with cells and we set $\omega = 0$ to control for the effects of background adhesion.

We simulate a model tissue with $\sigma_\omega = 0.1$ and $\tau_\omega = 10^3$, below our estimate for a T1 transition. The resulting monolayer is shown in Figure 5.2 (a): the system, despite fluctuations in $\omega_{ij}$, is solid and remains in a hexagonal lattice. Increasing $\sigma_\omega$ while keeping $\tau_\omega$ fixed reveals a crossover from a solid to a fluid state, whereby noise in the adhesion free energy functional causes phase-field cells to rearrange. Figure 5.2 (b) shows a model tissue with $\sigma_\omega = 1.0$ with $\tau_\omega = 10^3$, which allows for

sufficiently large fluctuations in adhesion to overcome the energy barriers associated with neighbour exchanges and enables cells to escape from their local neighbourhood through a series of T1 transition and become motile, resulting in a fluid-like state.

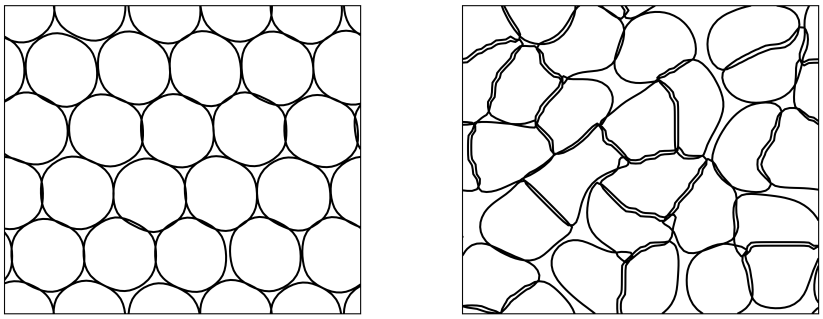

**(a)** **(b)**

**Figure 5.2:** Snapshots of model tissues with (a) $\sigma_\omega = 0.1$, $\tau_\omega = 1 \times 10^3$ and (b) $\sigma_\omega = 1.0$, $\tau_\omega = 1 \times 10^3$. The larger amplitude of adhesion fluctuations in (b) permits greater differences in $\omega_{ij}$ between different pairs of cells that result in intercalations and diffusive behaviour.

To quantify the difference in motility between the two cases, we measure the mean-square displacement averaged over cells

$$\mathrm{MSD}(t) = \frac{1}{N}\sum_{i=1}^{N} \left|\mathbf{r}_i(t+t_0) - \mathbf{r}_i(t_0)\right|^2, \tag{5.3}$$

where $N$ is the number of cells and $\mathbf{r}^{(i)}$ is the centre-of-mass position of cell $i$ at time $t$. The initial time is chosen as $t_0 = 2 \times 10^4$ to permit the onset of a dynamical steady state before measuring MSD. As expected, in the solid-like model tissue, MSD saturates at a small value, as shown in Figure 5.3 (a). In a fluidised layer, however, the MSD grows linearly in time, as pictured in Figure 5.3 (b).

Moreover, the total number of changes $N_n(t)$ in neighbour relations (a proxy for T1 transitions, which are otherwise difficult to count in the phase-field model), which is shown in Figure 5.4, also exhibits differences between layers in the solid-like and fluid-like regimes. Each cell has a set of neighbours $N_i(t)$ as implemented in Equation (5.1), which is identified as outlined in Subsection 2.2.4. For every time $t$, the cumulative number of neighbour changes is incremented by the size of the union of set differences $(N_i(t+\Delta t) - N_i(t)) \cup (N_i(t) - N_i(t+\Delta t))$. That is,

if between two points in time $t$ and $t + \Delta t$, cell $j$ either becomes or stops being a neighbour of cell $i$, then it contributes to the count of neighbour changes. The neighbour change remains zero in the solid-like tissue but grows linearly in the fluid-like tissue, revealing a constant rate of neighbour exchange. The presence of neighbour changes, in conjunction with the diffusive MSD, excludes flocking [67] as the origin of the measured cell motility.

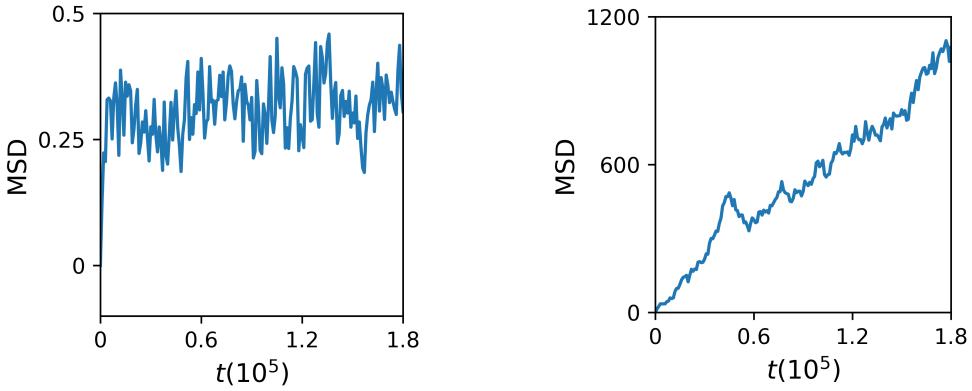


**(a)** **(b)**

**Figure 5.3:** Mean-square displacement as defined in Equation (5.3) with offset $t_0 = 2 \times 10^4$. (a) The solid phase with Cumulative neighbour changes plotted against time for the systems has an MSD that saturates around a small value, with flucuations arising from the changes in $\omega_{ij}$. Meanwhile, (b) the fluid phase with $\sigma_\omega = 1.0$, $\tau_\omega = 1 \times 10^4$ is in a diffusive regime, where changes in $\omega_{ij}$ and neighbour exchanges induce cells to migrate around the domain.

We perform a scan of phase space, varying $\tau_\omega$ logarithmically from $10^1$ to $10^5$ and varying $\sigma_\omega$ linearly from 0.1 to 1.5, which accounts for three orders of magnitude in the variance. Three metrics are calculated to characterise the solid-fluid crossover due to adhesion fluctuations, which are illustrated in Figure 5.5 in the $\tau_\omega$-$\sigma_\omega$ phase space: the translational diffusion coefficient $D_{\text{diff}}$, neighbour change rate $\tau_{\text{n}}^{-1}$, and the sixfold bond-orientational order parameter $\psi_6$.

The translational diffusion coefficient is calculated as $D_{\text{diff}} \equiv \text{MSD}(T)/(4T)$ where $T = 2 \times 10^5 - t_0$ is the duration of the simulation minus the offset $t_0 = 2 \times 10^4$, as defined in Equation (5.3). The translational diffusion coefficient exhibits two trends as we scan through phase space: as illustrated in Figure 5.5(a), although

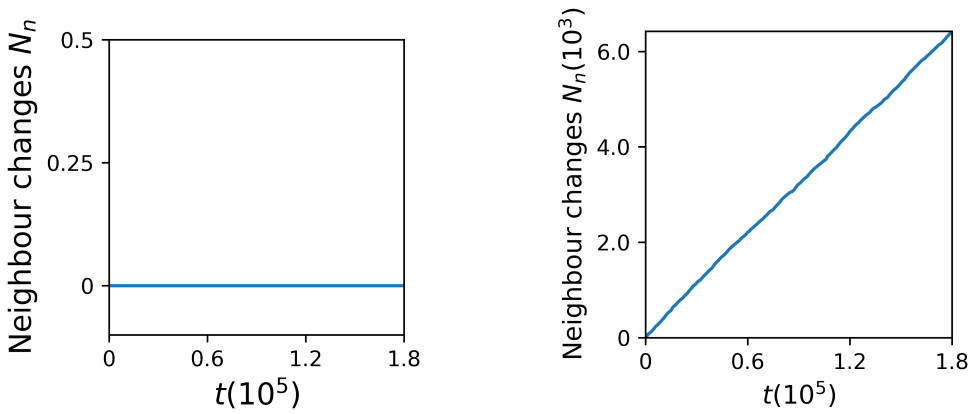


**Figure 5.4:** Cumulative neighbour changes $N_n(t)$ plotted against time for systems with (a) $\sigma_\omega = 1.0$, $\tau_\omega = 1 \times 10^3$ and (b) $\sigma_\omega = 0.1$, $\tau_\omega = 1 \times 10^3$, with the same offset $t_0 = 2 \times 10^4$ that is used to calculate the MSD in Figure 5.3. The solid phase sees no neighbour changes at all, while there is a constant rate of neighbour changes in the fluid phase.

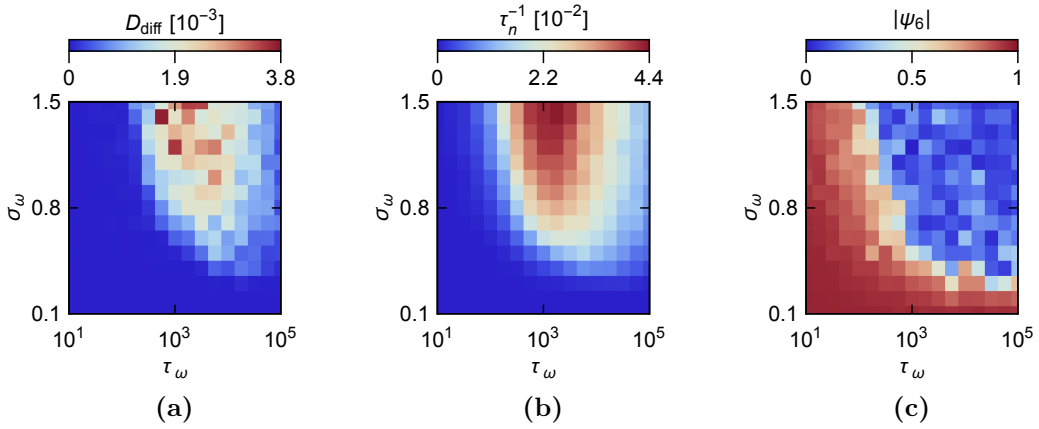


**Figure 5.5:** Heatmaps of (a) the translational diffusion coefficient $D_{\text{diff}}$, (b) neighbour change rate, and (c) final $|\psi_6|$ in $\tau_\omega$-$\sigma_\omega$ phase space. There is clearly an optimal region for cell diffusion and neighbour exchanges: the variance of the random process Equation (5.2) driving the adhesion free energy functional Equation (5.1) is not the only parameter controlling the fluidisation of the monolayer, owing to the finite time it takes for a quartet of cells to rearrange. The transition from high to low $|\psi_6|$, indicating a change from a hexagonal close-pack to a disordered state, matches the region of cell diffusion and neighbour changes (i.e., tissue fluidisation).

for every $\tau_\omega$, $D_{\text{diff}}$ increases with $\sigma_\omega$, the dependence on $\tau_\omega$ is non-monotonic and there is an optimum $\tau_\omega$ that maximises translational diffusion at each $\sigma_\omega$. This is in agreement with what Yamamoto et al. observed in the vertex model [127]. Similarly, we calculate average neighbour change rate as $\tau_n^{-1} = N_n(T)/T$. A

solid phase exhibits no neighbour rearrangements following the initial annealing of imperfections, while particles in a fluid phase change neighbours regularly. The average rate $\tau_n^{-1}$ is plotted as a heatmap in Figure 5.5(b). We observe that for sufficiently large $\tau_\omega$ and $\sigma_\omega$, neighbour changes occur at finite rate. Just as for the diffusion coefficient, the dependence on $\tau_\omega$ is non-monotonic, so that there is an optimal region in $\tau_\omega$-$\sigma_\omega$ space that maximises neighbour exchange rate.

Next, the hexatic order of the model tissue is quantified using the sixfold bond-orientational order parameter $\psi_6$, famously a feature of the KTHNY theory of crystal melting in two dimensions [137, 138] that has previously been used to characterise structure in systems of particles both active and passive [117, 131, 139]. Its magnitude goes from 1 for a hexagonal close-packing to 0 for a disordered system. It is calculated as

$$\psi_{6j} = \frac{1}{N_j} \sum_{k \in N_j} \exp(6i\theta_{k,j}) \tag{5.4}$$

where $j, k$ index cells, $N_j$ denotes both the set of neighbours of cell $j$ and the size of said set, and $i = \sqrt{-1}$ is the imaginary unit. The angle $\theta_{k,j}$ measures the azimuthal position of the centre of mass of cell $j$ with respect to that of cell $k$. We measure $|\psi_6| \equiv |\langle \psi_{6j} \rangle_j|$ the magnitude of the hexatic structure across all cells in a layer. The ground state of the passive phase-field model is a two-dimensional hexagonal close pack; the value of $|\psi_6|$ should go from 1 to 0 as the system crosses over from a solid to a fluid state. A heatmap of final $|\psi_6|$ is shown in Figure 5.5(c). As expected, the mean bond-orientational order parameter changes from 1 to 0 as $\tau_\omega$ and $\sigma_\omega$ become large, indicative of a crossover from a hexagonal close-packing to a disordered state. This crossover occurs at approximately the same $\sigma_\omega$ and $\tau_\omega$ as for the diffusion coefficient $D_{\text{diff}}$ and the neighbour change rate. Unlike the other metrics, however, there is no return to hexatic order as $\tau_\omega$ grows sufficiently large.

These results taken together confirm the importance of the variance of Equation (5.2) while emphasising the importance of fluctuation persistence time in the fluidisation of the phase-field monolayer. As $\tau_\omega$ increases, variations in $\omega_{ij}$ are persistent enough to enable neighbour rearrangements, but as $\tau_\omega$ gets bigger the

dynamics slows down while the geometry remains disordered. This is because the dynamics of $\omega_{ij}$ given by Equation (5.2) approaches a Wiener process as $\tau_\omega$ grows ever larger. The one-dimensional Wiener process is recurrent: after a sufficiently long time, any large positive or negative value of $\omega_{ij}$ will return to zero. However, the probability distribution of first-passage times is fat-tailed, with $f(t) \sim t^{-3/2}$: it takes very long times for $\omega_{ij}$ to return to the mean $\bar{\omega}$ without the drift term [140]. Consequently, the monolayer has pairs of cells that are stuck together and repelled from one another with large positive and negative values of $\omega_{ij}$, which last for a very long time and prevent translational diffusion and cell intercalations while remaining spatially disordered.

### 5.3.2 Velocity Correlations

Finally, we consider the nature of flow in this model. This is achieved by computing the velocity-velocity correlation and determining its length. Any hydrodynamic effects will manifest [6, 7] as long-range velocity correlations. The velocity-velocity correlation is defined as

$$C(\mathbf{r}) = \frac{\langle v_x(\mathbf{x}+\mathbf{r})v_x(\mathbf{x}) + v_y(\mathbf{x}+\mathbf{r})v_y(\mathbf{x})\rangle_{\mathbf{x},t}}{\langle\, |\mathbf{v}(\mathbf{x},t)|^2\rangle_{\mathbf{x},t}} \tag{5.5}$$

This function with vectorial argument is further averaged over orientation to obtain $C_v(r) \equiv \langle C_v(\mathbf{r})\rangle_{\arg(\mathbf{r})}$. The correlation $C_v(r)$ is shown in Figure 5.6, and decays to zero in both the solid and the fluid monolayer on a lengthscale commensurate with a cell diameter, where the cell radius is $R = 8$. Although the monolayer is fluidised by the adhesion fluctuations, the layer does not show any hydrodynamic behaviour.

## 5.4 Discussion

We studied a multi-phase field model for an epithelium [67, 68] augmented with fluctuating pairwise adhesions following an Ornstein-Uhlenbeck process. We show that adhesion fluctuations result in T1 transition leading to diffusive motion of cells in the model monolayer. This provides another fluidisation mechanism for

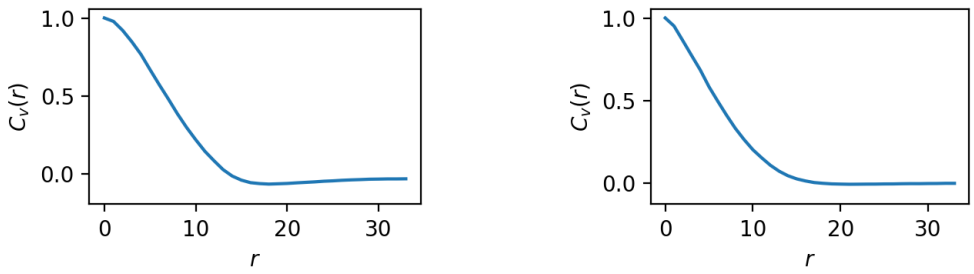


**(a)** **(b)**

**Figure 5.6:** Velocity-velocity correlation function $C_v(r)$ for (a) the solid phase and (b) the fluid phase. In both cases, the correlation decays to zero on the lengthscale of a cell diameter. There are no long-range velocity correlations, and therefore no hydrodynamics, in this system.

phase-field models that does not invoke cell-level polar [67, 139] or nematic [68, 100] activity, which may not be applicable to all epithelia.

Such Ornstein-Uhlenbeck fluctuations have previously been studied as a fluidisation mechanism in cellular vertex models [54, 126, 127, 132]. Our work validates these results for a different type of discrete cell-level model and we found the cell diffusion coefficient to have a non-monotonic dependence on persistence time in adhesion fluctuation, in agreement with what was reported in vertex models [127].

Fluctuating tensions have proven a useful paradigm in studies of, e.g., budding in three dimensions [56, 141] and nematic forces with a global direction [129]. In addition, changes in adherens junctions and the solid-fluid crossover have been implicated in wound healing and other collective behaviours of epithelia [142, 143]. We, therefore, hope the model proposed here will be a useful starting point in further studies using phase-field models. In future work, pairwise adhesion terms could be modified to, for example, also account for catch-bond interactions between cadherins and the cytoskeleton [14], the length of cell-cell interfaces [144, 145], respond to local tensions [115], or depend on cell shape [55].

*"Why," said the Dodo, "the best way to explain it is to do it."*

— Lewis Carroll [1]

# 6 Spontaneous Shear Flow in Channel

## 6.1 Introduction

Chapter 3 discusses the persistent rotational motion of pairs of epithelial cells in confinement, and Chapters 4 and 5 discuss bulk features of epithelial tissues. These treatments are well-motivated by results in the literature, but present only a starting point for investigations into the collective behaviours of bulk epithelia, which experience different interactions and exhibit different behaviours than individuals or pairs, and therefore must be described by new physics [27].

Epithelial cells frequently organise in monolayers [12], adhering to each other through E-cadherin junctions and to the extracellular matrix (ECM) through integrin proteins. These junctions crosslink an internal cytoskeleton composed of microtubules and the actomyosin cortex, which distributes stresses across the entire cell layer [13]. Fluctuations in these junctions are introduced in Chapter 5 to enable neighbour rearrangements in the monolayer. The cytoskeleton is responsible for several other behaviours and causes epithelia to migrate collectively, both in vivo and in vitro [14]. In particular, epithelia confined to a circle break rotational symmetry to rotate in groups that number $\mathcal{O}(10^1)$ to $\mathcal{O}(10^2)$ cells [36, 37]. Also, epithelia confined to a channel can exhibit a spontaneous shear flow [38] that has been described by active nematohydrodynamics.

Active nematic theories have proven a successful description of epithelial monolayers precisely because epithelial sheets have nematic properties. Cells of various types, from human melanocytes to Madin-Darby Canine Kidney cells and bacteria, display nematic order [6, 7]. Although individual epithelial cells migrate as polar agents [13, 19], polar behaviour is suppressed in the bulk and dipolar behaviour emerges. Contact inhibition of locomotion hinders polar motility [11, 28] and lamellipodia, protrusions of the actomyosin cortex at the front of a cell, are much smaller in the bulk than in free cells [14]. The formation of supracellular microtubule and actomyosin structures supports the creation of system-sized active stresses [13, 14], and the suppression of focal adhesions by adherens junctions is another mechanism by which polar activity is diminished [13]. We hypothesise therefore in this Chapter that the collective behaviours of epithelia are controlled by dipolar activity.

We are interested in the flow of epithelia in confinement, and this Chapter discusses the flow of an epithelium in a channel in the presence of an active nematic stress. Two key features that affect epithelial flow in a channel are the width of the channel and the anchoring of individual cells at an angle to the boundary [7]. In a sufficiently small channel, epithelia exhibit unidirectional flow [146], while cell sheets in wider channels display shear and oscillatory flow [38, 90]. Confined monolayers even exhibit vortex chains [146], which give way to active turbulence in sufficiently large systems [29, 89]. In larger active nematics, the size of vortices is given by an active length scale $\sim \sqrt{K/|\zeta|}$, the square root of the ratio of the elastic constant to activity in a nematic [7, 87, 147].

In addition, cells have been shown to anchor at an angle to the confining boundary in experiment. When plated on a fibronectin annulus, cells including fibroblasts, epithelial cells and endothelial cells, spontaneously break symmetry to preferentially anchor at an angle with respect to the boundaries of the annulus. This symmetry-breaking results in an azimuthal shear flow [105]. The spontaneous shear flow discussed by Duclos et al. is also associated with the anchoring of cells at the edge of the channel [38].

A third key feature that affects the fluid behaviour of an epithelial monolayer, and the focus of this Chapter, is its internal friction. The greatest challenge to bridging the gap from the cell scale to the continuum has been the formulation of cell-cell friction in the monolayer; that is, the implementation of bulk and shear viscosity in agent-based models. Previous work has included viscosity as cell-cell friction in a different multi-phase field model [148]. Monolayer viscosity has also been implemented as a frictional force between vertices in the cellular vertex model [50], and has resulted in flow along a channel [51, 52].

In this Chapter, we seek to obtain flow in a channel of phase-field cells. Thus far, the multi-phase field model in the overdamped limit has failed to recover system-scale flow. We choose to simplify the geometry to that of a channel with periodic boundary conditions along the long axis to investigate the behaviour of phase-field cells. The system is endowed with with a dipolar stress field in accordance with the hypothesis that the epithelium is a nematic liquid crystal dominated by dipolar stresses. Active anchoring is a feature of epithelial nematics, and is a result of the flow in the system [38, 105]. Therefore in this Chapter we work backwards. First we impose anchoring by hand in a dynamical regime dominated by substrate friction. The choice of anchoring results in a plug flow, the velocity of which depends on the width of the channel. In the second part of this Chapter, we formulate a dynamics with a Stokesian viscosity term, which when discretised on a lattice manifests as an internal friction in the monolayer. We dispense entirely with anchoring by hand and find that for a sufficiently strong internal friction compared to substrate friction, active anchoring emerges spontaneously along with a persistent shear flow.

## 6.2 Model with Substrate Friction

The model for the channel follows the development in Chapter 2. The equation of motion is (2.1). For now, we assume the dynamics are dominated by substrate friction with the force balance given by Equation (2.2). The passive dynamics are controlled by four free energy functionals. Three are the same as in Chapter 2: the Cahn-Hilliard phase separation term (2.4a), the area conservation term (2.4b)

and the overlap term (2.6a). The adhesion free energy, however, differs, and is given by Equation (3.1) in Chapter 3.

The description of the dipolar stress density in this channel model is specialised from the more general description in Subsection 2.1.5 of Chapter 2 through the choice of $\hat{\mathbf{u}}$ in the director dynamics and in the choice of $\zeta_{\text{self}}$ and $\zeta_{\text{inter}}$ that control the self-induced and neighbour-neighbour active forces. The cell-level nematic tensor $\mathbf{Q}_i$ is constructed according to Equation (2.17) and the active dipolar forces are defined as in Equation 2.20. In this implementation, we are concerned only with inter-cellular dipolar forces, so we set $\zeta_{\text{self},i} = 0$ and $\zeta_{\text{inter},i} = \zeta$ with $\mathbf{f}_{\text{dipolar},i} = \mathbf{f}_{\text{inter},i} = -\sum_{j\neq i} \zeta \mathbf{Q} \cdot \nabla \phi_j$. The dynamics of $\mathbf{n}_i$ is defined as in Equation (2.18), with a specialised choice of $\hat{\mathbf{u}}$ so that $\mathbf{n}_i$ relaxes towards the long axis of cell $i$ with timescale $J_n^{-1}$ according to Equation (4.1). As described in Chapter 4 and illustrated in Figure 4.1, the use of the signum of $\mathbf{n}_i \cdot \hat{\mathbf{d}}_{\parallel,i}$ allows $\mathbf{n}_i$ to relax to the closer of $\hat{\mathbf{d}}_{\parallel,i}$ and $-\hat{\mathbf{d}}_{\parallel,i}$, so that the reorientation of the nematic director has the desired head-tail symmetry.

The channel has confining walls at the top and bottom, and periodic boundary conditions along the $x$-axis. The walls are implemented using static phase fields

$$\phi_{\text{wall}}(\mathbf{x}) = \exp(-y/\lambda_{\text{wall}}) + \exp(-(L_y - y)/\lambda_{\text{wall}}), \tag{6.1}$$

with an exponential decay at the top and bottom of the channel, which the cells are not able to cross due to a repulsive interaction with the walls. These interactions are given by a free energy density

$$\mathcal{F}_{\text{rep, wall}} = \sum_i \sum_{j\neq i} \frac{\kappa_{\text{wall}}}{\lambda} \int \mathrm{d}\mathbf{x}\, \phi_i^2 \phi_{\text{wall}}^2. \tag{6.2}$$

There are no frictional or adhesive interactions with walls, so cells in contact with the wall are free to slip against it. The model as it stands is unable to flow spontaneously. Therefore, we include an additional interaction with walls to explicitly reproduce the anchoring observed in experiment [38, 105].

The key new feature, and difference between this model and that in Chapter 2, is the anchoring at walls, which has been shown in a continuum model to control

the nature of steady-state flows in a polar fluid [149]. This is achieved by setting $\mathbf{n}_i$ by hand to $\mathbf{n}_i = (\cos\theta, \sin\theta)$ when the centre of mass of cell $i$ is sufficiently close to a wall. This distance threshold is set at $2.5R$, which implements anchoring in a single layer of cells nearest to each wall. At the upper wall of the channel, $\theta$ was set to $2\pi/3$, while at the lower wall of the channel $\theta$ was set to $\pi/3$. This geometry is consistent with both bend and splay director profiles, both of which can result in flow according to $\mathbf{f}_{\text{dipolar},i} = -\sum_{j\neq i} \zeta \mathbf{Q}_j \cdot \nabla\phi_j$.

The simulations run for $2 \times 10^4$ timesteps. The control parameters for this model are the width of the channel $L_y \in [52, 104]$, and the strength of the dipolar activity $\zeta \in [-0.8, 0.8]$. The width of the channel was chosen to enable the formation of two to six rows of cells, each of which has $R = 8$. The choices of value for $\zeta$ take the system from strongly contractile, to passive, and then to strongly extensile. The coefficient of substrate friction is $\xi = 3.0$. The free energy densities have parameters $\gamma = 1.4$, $\lambda = 2.0$, $\mu = 120$, $\kappa = 1.5$ and $\omega = 0.4$, and the relaxation in Equation (2.1) is controlled by $J_0 = 5 \times 10^{-3}$. The lengthscale of the wall is $\lambda_{\text{wall}} = 3.0$ and the line energy of repulsive interactions with the wall is $\kappa_{\text{wall}} = 4.0$. There is no adhesion to the wall; that is, $\omega_{\text{wall}} = 0.0$.

## 6.3 Results with Substrate Friction

The behaviour of phase-field cells in the channel exhibits differences in flow and orientational order according to whether they are extensile or contractile. Variations in flow and the velocity-velocity correlation length scale for different channel widths are due to differences in the active length scale for extensile and contractile cells.

### 6.3.1 Flow

Flow in the channel is quantified by analysing cell displacements. Data are not recorded for every timestep, but rather on regular intervals $\Delta t$. The average velocity for each cell is calculated using the centre-of-mass displacement on these intervals

$$\bar{\mathbf{v}}_i(t) = \frac{1}{\Delta t}\Big(\mathbf{r}_{\text{COM}}(t) - \mathbf{r}_{\text{COM}}(t - \Delta t)\Big). \tag{6.3}$$

The value of $\Delta t$ is typically $\Delta t = 250$, although for large systems (that is, with $L_y \gtrsim 100$ units) it is set at $\Delta t = 500$. A global velocity field $\mathbf{v}(\mathbf{x})$, is constructed as a weighted average of the cell mean velocity fields as

$$\mathbf{v}(\mathbf{x}, t) = \sum_i \bar{\mathbf{v}}_i(t)\phi_i(\mathbf{x}, t) \equiv v_x(\mathbf{x}, t)\hat{\mathbf{i}} + v_y(\mathbf{x}, t)\hat{\mathbf{j}}. \tag{6.4}$$

Data are analysed for the second half of the simulation, between $t = 10^4$ and $t = 2 \times 10^4$. This is so that the system can evolve from a random initial condition to a dynamic steady state, which may or may not have a well-defined flow profile. The global velocity field is used to compute the average of the $x$-component of velocity over both time and space:

$$\langle v_x(y) \rangle = \langle v_x(\mathbf{x}, t) \rangle_{x,t} \tag{6.5}$$

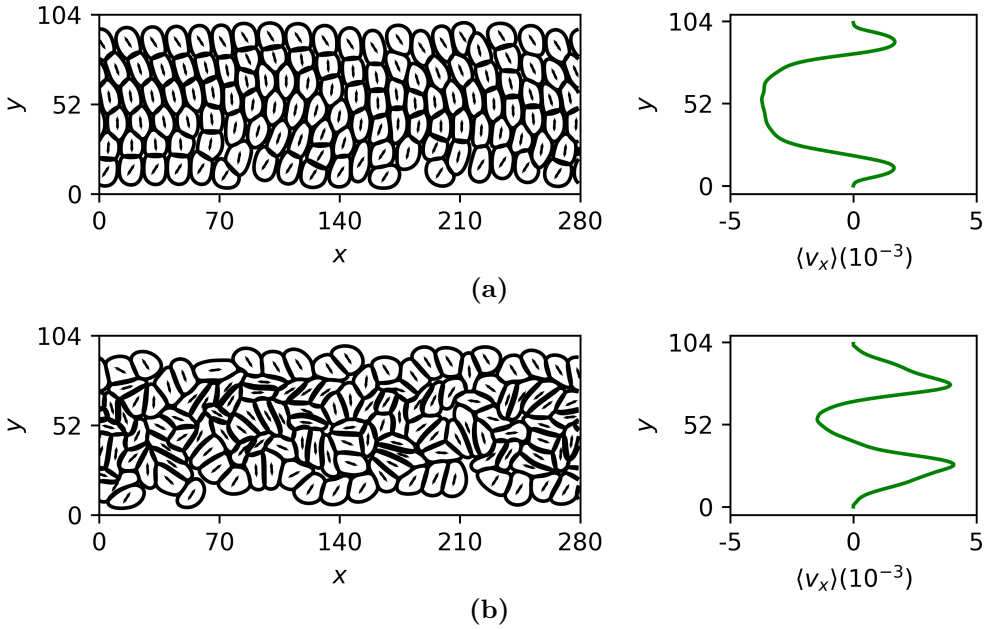


**Figure 6.1:** Snapshots at time $t = 2 \times 10^5$ of the monolayer in a channel of width $L_y = 104$, for dipolar activities (a) $\zeta = -0.8$ and (b) $\zeta = +0.8$, as well as profiles of $\langle v_x \rangle$ for each. The cells are marked with rods to indicate their nematic directors $\mathbf{n}_i$. (a) The contractile system exhibits a bend profile across the width of the channel and an associated plug flow profile in the mean velocity along the channel, $\langle v_x \rangle$. (b) In contrast, the extensile system displays only small patches of nematic order, as well as a 'capped-line' state in which neighbouring cells differ in orientation by $\pi/2$. Flow at the centre of the channel is weak, and flow at the edges is induced by the anchoring boundary conditions.

The mean velocity along the channel $\langle v_x(y) \rangle$ reveals that contractile cells flow due to a bend profile that is stabilised by the anchoring, while extensile cells adopt

local perpendicular ordering and fail to flow. Figure 6.1 depicts representative snapshots of epithelia in the channel, as well as the average $x$-velocity $\langle v_x \rangle$, for two values of activity $\zeta = \pm 0.8$ in a channel of width $L_y = 104$. The contractile layer with $\zeta = -0.8$ adopts a bend profile across the channel and exhibits a plug flow commensurate with the sign of $\nabla \cdot \mathbf{Q}$, similar to that sketched in Figure 1.4 (a) in Chapter 1. A bend perturbation decays in a bulk contractile active nematic, but the bend persists in this system because it is enforced by the anchoring. There is a velocity to the right at the edge of the channel as the first row of cells in the bulk slips past the cells on the boundary.

In contrast, the extensile layer with $\zeta = +0.6$ does not show any system scale nematic profile, bend, splay or otherwise. There are local patches of nematic order separated by 'capped line' features, where neighbouring cells differ in orientation by $\pi/2$. There is no appreciable flow in the centre of the channel, and the strongest flow in the system is that induced by the enforced anchoring at the walls.

The presence of flow along the channel prompts investigation into the dependence of the flow speed on the channel width, as shown in experiment [29, 38, 87, 146]. In addition, the system-scale orientational order exhibited by the contractile cells permits a scaling argument for flow velocity in terms of channel width. The flow velocity is defined as the mean of $v_x$ in the centre of the channel:

$$v_{\text{flow}} = \langle v_x(L_y/2) \rangle \tag{6.6}$$

and is signed. The flow velocity at the centre of the channel as a function of activity $\zeta$ for different values of channel width $L_y$ is shown in Figure 6.2. For contractile cells, with $\zeta < 0$, the magnitude of $v_{\text{flow}}$ increases as a function of $|\zeta|$ and decreases as $L_y$ grows. Extensile cells, however, display different behaviour to contractile cells. The narrowest channels, with $L_y = 52$, are small enough to force extensile cells into a splay configuration, which results in flow. However, as shown in Figure 6.2, the direction of the flow shifts for sufficiently wide channels. In addition, any nematic order or texture disappears into the 'capped-line' state illustrated in Figure 6.1 (b).

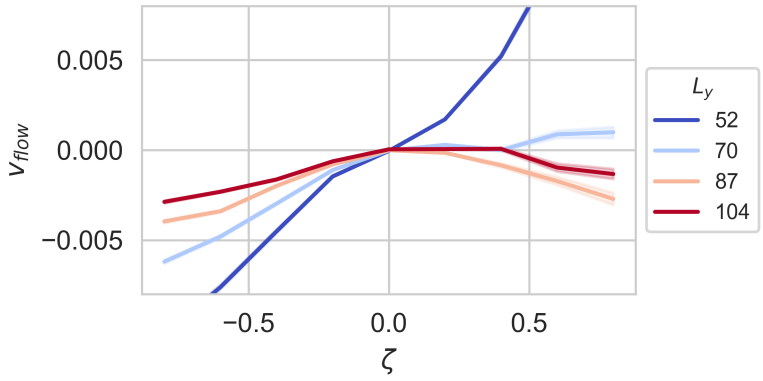


**Figure 6.2:** Flow velocity in the channel centre $v_{\text{flow}}$ graphed as a function of $\zeta$, for channel widths between 52 and 104. For contractile cells, the flow is stronger for higher activity $|\zeta|$ and narrower channels. Flow is stronger for the narrowest channels when the cells are extensile, but is very weak and even changes direction for sufficiently wide channels. This suggests that the widest channels are larger than the active length scale $\sqrt{K/|\zeta|}$ when cells are extensile.

Given a nematic texture with anchoring enforced by hand at the walls of the channel, as is the case for the contractile systems in this Section, it is straightforward to rationalise the dependence of the flow velocity on channel width. We treat the cells in the channel as having a translational symmetry in the $x$ direction. Then, adopting temporarily the language of active nematohydrodynamics, the free energy density due to bending in director field $\mathbf{n} = (\cos\theta_Q, \sin\theta_Q)$ is

$$\mathcal{F} = \frac{K}{2}\Big((\partial_y n_x)^2 + (\partial_y n_y)^2\Big) \propto \left(\frac{\mathrm{d}\theta_Q}{\mathrm{d}y}\right)^2, \tag{6.7}$$

which is minimised by $\mathrm{d}\theta_Q/\mathrm{d}y = \text{constant}$; that is, the director angle has a linear profile from $\theta_Q = \pi/3$ at $y = 0$ to $\theta_Q = 2\pi/3$ at $y = L_y$. The $x$-component of the active force is

$$f_{\text{active},x} = -\zeta\partial_y \mathbf{Q}_{yx} = -\zeta\partial_y \sin(2\theta_Q) = -2\zeta\frac{\partial\theta_Q}{\partial y}\cos(2\theta_Q). \tag{6.8}$$

For director angles $\theta_Q \in (\pi/4, 3\pi/4)$, we find $\cos(2\theta_Q) < 0$. In conjunction with $\zeta < 0$ and a linear profile $\partial\theta_Q/\partial y \propto L_y^{-1}$, we obtain a scaling

$$f_{\text{active},x} \propto \zeta^1 L_y^{-1}. \tag{6.9}$$

resulting also in $v_{\text{flow}} \propto \zeta^1 L_y^{-1}$ due to the overdamped force balance in Equation (2.2). The scaling is only approximate, and relies on a linear dependence of $\theta_Q$ on $y$, which

is clearly not always true, as illustrated in Figure 6.1 (a), but helps to explain the results for $\zeta < 0$ as shown in Figure 6.2.

Although this model with anchoring implemented by hand results in a unidirectional flow, there is no suggestion of a transition to bidirectional flows or other behaviour as the channel width grows [7, 87, 89, 147]. This represents a qualitative difference between this multi-phase field model and both experimental epithelial monolayers and numerical active nematohydrodynamic systems. We attribute this distinction to the lack of any dynamic viscosity, such as appears in the Stokes equation and in active nematohydrodynamics, in the present formulation of the multi-phase field model. We account for such a term in the remainder of this Chapter and obtain a spontaneous shear flow without recourse to artificial anchoring at the edge of the channel.

## 6.4 Continuum Dynamics

The very object of using the multi-phase field model is to determine what physics at the agent level is required to reproduce the results of biological experiments, and how these phenomena relate to continuum theories. Thus far, the multi-phase field model has not accounted for viscosity, which appears as a term in active nematohydrodynamics, and we would like to include it in an improved description of the dynamics of the phase-field model, with the hope of recovering spontaneous flow. It is instructive, therefore, to examine how viscosity manifests in continuum dynamics, is described by other models for epithelia, and is evident in experiment. A generic feature of the Navier-Stokes equations is the presence of a viscous stress [73, 74]

$$\sigma_{\text{visc}} = \mu(\nabla \mathbf{u} + (\nabla \mathbf{u})^{\top}) + \nu \nabla \cdot \mathbf{u}\, \mathbb{1} \tag{6.10}$$

up to redefinition of the bulk viscosity $\nu$. In an incompressible fluid, the viscous stress can be written simply as [7]

$$\sigma_{\text{visc}} = \mu(\nabla \mathbf{u} + (\nabla \mathbf{u})^{\top}). \tag{6.11}$$

In the incompressible limit, then, the viscous force is proportional to the Laplacian of the flow

$$\mathbf{f}_{\text{visc}} = \mu \nabla^2 \mathbf{u} \tag{6.12}$$

and serves to dissipate velocity gradients by exchanging momentum within the flow. Although viscosity has on occasion been neglected in order to elucidate the nature of active nematic stresses and instabilities [40], the viscous stress is a necessary component of fluid systems, especially in the low-Reynolds-number, Stokesian limit. In addition, viscosity and effective friction due to fluid depth have been shown to control the behaviour of active flows in the continuum [7, 150].

The multi-phase field model was originally formulated using a force balance at the substrate enforced for every cell at every lattice site, given by

$$\xi \mathbf{v}_i(\mathbf{x}, t) = \mathbf{f}_{\text{passive},i}(\mathbf{x}, t) + \mathbf{f}_{\text{active},i}(\mathbf{x}, t). \tag{6.13}$$

There is no acceleration term here because this is the overdamped limit, in which dissipation at the substrate dominates inertia. We now extend the force balance of Equation (6.13) by including a term analogous to that in Equation (6.12) to put the phase-field dynamics in a viscosity-dominated, low-Reynolds-number limit. In this case, dissipation still dominates inertia, but now it is dissipation internal to the monolayer, rather than against the substrate.

## 6.5 Model with Internal Friction

A starting place for defining cell-cell friction is to write down a schematic Stokesian force balance with a viscous stress [6, 7]

$$0 = -\xi \mathbf{v}_i(\mathbf{x}, t) + \xi_{\text{cell}} \nabla^2 \mathbf{v}_i(\mathbf{x}, t) + \mathbf{f}_{\text{passive},i}(\mathbf{x}, t) + \mathbf{f}_{\text{active},i}(\mathbf{x}, t) \tag{6.14}$$

where it remains to describe the interactions between different cells $i$ and $j$. The coefficient $\xi_{\text{cell}}$ is here the viscosity of the cytoplasm within each cell, and will turn out also to be the viscosity associated with cell-cell interactions. Following

the lead of Chiang et al. [148, 151], we write a normalised mean velocity field for the monolayer as

$$\mathbf{V}(\mathbf{x},t) = \frac{\sum_i \phi_i(\mathbf{x},t)\mathbf{v}_i(\mathbf{x},t)}{\sum_i \phi_i(\mathbf{x},t)}. \tag{6.15}$$

We must choose some way to distribute the viscous dissipation of the mean velocity field $\mathbf{V}$ onto the cell-level viscosity fields $\{\mathbf{v}_i(\mathbf{x},t)\}$. Therefore we write an approximate discrete Laplacian on a square lattice using

$$\nabla^2\mathbf{v}_i(\mathbf{x},t) \approx \frac{1}{h^2}\sum_{\mathbf{x}'\in N(\mathbf{x})}\Big(\mathbf{V}(\mathbf{x}',t) - \mathbf{v}_i(\mathbf{x},t)\Big). \tag{6.16}$$

where the notation $\mathbf{x}' \in N(\mathbf{x})$ denotes the four sites neighbouring site $\mathbf{x}$ on the square lattice, although in the implementation of CELADRO, lattice sites are indexed by integers rather than coordinates, as described in Subsection 2.2.2 of Chapter 2. Equation (6.16) has the property that

$$\frac{\sum_i \phi_i(\mathbf{x},t)\nabla^2\mathbf{v}_i(\mathbf{x},t)}{\sum_i \phi_i(\mathbf{x},t)} \approx \nabla^2\mathbf{V}(\mathbf{x},t) \tag{6.17}$$

in the sense of the five-point discrete Laplacian. It is through differences with the mean flow, in Equation (6.16), that the velocity fields of different cells interact with each other, as well as with themselves. Inserting the approximation of Equation (6.16) into the Stokesian force balance in Equation (6.14), we obtain

$$\xi\mathbf{v}_i(\mathbf{x},t) + \frac{\xi_{\text{cell}}}{h^2}\sum_{\mathbf{x}'\in N(\mathbf{x})}\left[\mathbf{v}_i(\mathbf{x},t) - \frac{\sum_j \phi_j(\mathbf{x}',t)\mathbf{v}_j(\mathbf{x}',t)}{\sum_j \phi_j(\mathbf{x}',t)}\right] = \mathbf{f}_{\text{passive},i}(\mathbf{x},t) + \mathbf{f}_{\text{active},i}(\mathbf{x},t) \equiv \mathbf{f}_{\text{body},i}(\mathbf{x},t), \tag{6.18}$$

which is a sparse linear system of rank $N \times N_{\text{patch}}$. Solving this system yields the full set of velocity fields $\{\mathbf{v}_i(\mathbf{x},t)\}$ that are correlated by their frictional interactions.

The system is solved using the Jacobi method [152]. Equation (6.18) is rewritten as

$$\left(\xi + \frac{4\xi_{\text{cell}}}{h^2}\right)\mathbf{v}_i(\mathbf{x},t) = \mathbf{f}_{\text{body},i}(\mathbf{x},t) + \frac{\xi_{\text{cell}}}{h^2}\sum_{\mathbf{x}'\in N(\mathbf{x})}\mathbf{V}(\mathbf{x}',t) \tag{6.19}$$

and the solution is found iteratively as

$$\mathbf{v}_i^{(k+1)}(\mathbf{x},t) = \left(\xi + \frac{4\xi_{\text{cell}}}{h^2}\right)^{-1} \mathbf{f}_{\text{body},i}(\mathbf{x},t) + \left(\xi + \frac{4\xi_{\text{cell}}}{h^2}\right)^{-1} \frac{\xi_{\text{cell}}}{h^2} \sum_{\mathbf{x}' \in N(\mathbf{x})} \frac{\sum_j \phi_j(\mathbf{x},t)\mathbf{v}_j^{(k)}(\mathbf{x},t)}{\sum_j \phi_j(\mathbf{x},t)} \tag{6.20}$$

where the viscosity $\xi_{\text{cell}}$ of the Stokes equation (6.14) manifests as a coefficient of dynamic friction for the interactions between different cell-level velocity fields $\{\mathbf{v}_i(\mathbf{x},t)\}$, as well as for the interaction of each velocity field $\mathbf{v}_i(\mathbf{x},t)$ with itself. Equations (6.18) and (6.20) can be cast as matrix equations

$$\mathbf{M}\mathbf{v}_\alpha = \mathbf{f}_\alpha \tag{6.21a}$$

$$\mathbf{v}_\alpha^{(k+1)} = \mathbf{G}\mathbf{v}_\alpha^{(k)} + \mathbf{b} \tag{6.21b}$$

where $\alpha \in x, y$. The matrix $\mathbf{G}$ is related to $\mathbf{M}$ by $\mathbf{G} = \mathbf{D}^{-1}(\mathbf{M} - \mathbf{D})$ where $\mathbf{D} = \text{diag}(\xi + 4\xi_{\text{cell}}/h^2)$ contains the diagonal entries of $\mathbf{M}$. The iterative scheme converges because the matrix $\mathbf{M}$ is strictly diagonally dominant by row. A matrix $\mathbf{A}$ is strictly diagonally dominant by row iff

$$|a_{ii}| > \sum_{j \neq i} |a_{ij}|. \tag{6.22}$$

The diagonal entries of $\mathbf{M}$ have

$$|m_{ii}| = \xi + \frac{4\xi_{\text{cell}}}{h^2}, \tag{6.23}$$

while the sums of the absolute values of the off-diagonal entries in row $i$ are

$$\sum_{j \neq i} |m_{ij}| = \frac{\xi_{\text{cell}}}{h^2} \sum_{\mathbf{x}' \in N(\mathbf{x})} \frac{\sum_j \phi_j(\mathbf{x}',t)}{\sum_j \phi_j(\mathbf{x}',t)} = \frac{4\xi_{\text{cell}}}{h^2}. \tag{6.24}$$

The matrix $\mathbf{M}$ has the desired property when $\xi$, the substrate friction, is finite. This implies all the eigenvalues of $\mathbf{G}$ have magnitude less than one. In particular, the eigenvalues $\lambda_G$ of $\mathbf{G}$ are bounded by [152]

$$|\lambda_G| \leq \sum_{j \neq i} \frac{|m_{ij}|}{|m_{ii}|} = \frac{1}{1 + \frac{h^2}{4}\frac{\xi}{\xi_{\text{cell}}}} \tag{6.25}$$

Therefore, the iterative scheme to solve Equation (6.18) converges given finite substrate friction.

We use the full Stokesian viscous force calculation of Equation (6.18) to solve for the flow in a channel, with the aim of recovering shear and other channel-wide flows. The key control parameter in this problem is $\xi_{\text{cell}}$ the cell viscosity, which is set to values ranging from 0.0 to 3.0. The coefficient of substrate friction remains $\xi = 3.0$ and the dipolar activity is set to $\zeta = -1.0$. The parameter controlling cell-cell adhesion remains $\omega = 0.4$, as in Section 6.2. It must be remarked that the presence of cell-cell adhesions does not amount to a fluid viscosity. This is because adhesion is modelled by a free energy functional that only favours the overlap of cells' interfaces and does not depend on the velocity of one or more interfaces.

In this implementation, the channel has $L_x = 140$ and $L_y = 70$, and the system contains 42 phase-field cells, each of which is defined on a patch of size $L_{\text{patch}} = 31$. The free energy relaxation parameter is changed to $J_0 = 1 \times 10^{-3}$ to aid numerical stability. All other parameters are identical to those in Section 6.2. These simulations are run for $1 \times 10^5$ timesteps, and data were collected every $\Delta t = 1000$ timesteps.

## 6.6 Results with Internal Friction

In this Section, we are interested in the possibility of the emergence of spontaneous flow using the Stokesian force balance in Equation (6.18), which motivates our focus on the control parameter $\xi_{\text{cell}}$. Therefore we leave investigation into the effect of activity $\zeta$ or channel width $L_y$ to future work, although these parameters individually and together have also been shown to control the nature of active nematic flows in a channel [87, 89, 147]. Cell-cell friction mediated by $\xi_{\text{cell}}$ recovers diagonal alignment and spontaneous shear flow in the multi-phase field model similar to that described by Duclos et al. in an epithelial monolayer confined to a channel [38]. The persistence in time, that is, the duration during which the flow moves in one direction before reversing, depends on the value of the viscosity $\xi_{\text{cell}}$. As in Section 6.3, we create snapshots of the phase-field monolayer and provide graphs of $\langle v_x \rangle$ as a function of $y$. In addition, we create kymographs of the flow along the channel over

time, and quantify the mean nematic director angle $\theta$ as a function of $y$. Here, all time-averaged quantities are calculated using the full duration of each simulation.

### 6.6.1 Flow

In a system of dipolar multi-phase field cells with contractile activity $\zeta = -1.0$, the onset of symmetry-breaking and shear flow depends on the value of the viscosity $\xi_{\text{cell}}$. When there is no viscosity, $\xi_{\text{cell}}$, there is no flow, but shear flow sets in above a threshold $\xi_{\text{cell}}$. An average flow field is constructed as a weighted average of the cells' centre-of-mass displacements according to Equations (6.3), (6.4), and (6.5), with $\Delta t = 1000$. Note that the average flow field $\mathbf{v}(\mathbf{x}, t)$ constructed from the centre-of-mass displacements is distinct from the normalised mean velocity field $\mathbf{V}(\mathbf{x}, t)$ as defined in Equation (6.15). The components $v_x(\mathbf{x}, t)$ and $v_y(\mathbf{x}, t)$ can then be averaged over position, time, or both.

The behaviour of contractile cells in the channel depends on the value of the internal friction parameter $\xi_{\text{cell}}$, and this dependence is illustrated in Figure 6.3 with snapshots of the dynamic steady state as well as kymographs of $\langle v_x(y, t)\rangle \equiv \langle v_x(\mathbf{x}, t)\rangle_x$. When the viscosity $\xi_{\text{cell}}$ is zero, the steady state exhibits no flow, and as $\xi_{\text{cell}}$ grows, an oscillatory shear state emerges and then becomes more persistent.

An active system with no internal friction, $\xi_{\text{cell}} = 0$, has a dynamic steady state that aligns with the channel, as shown in Figure 6.3 (a). The system evolves to the steady state via a transient, illustrated in Figure 6.3 (b), but eventually there is no flow, despite the monolayer's contractile activity. This system with no internal friction matches the substrate-friction-dominated model of Section 6.2, with the difference that here there is no anchoring enforced by hadn at the channel walls. For small $\xi_{\text{cell}} = 1.0$, pictured in Figure 6.3 (c) and (d), an oscillatory state emerges in which a shear flow is established but changes direction on the order of $\mathcal{O}(10^3)$ timesteps, and is associated with a reorientaton of the cells around $\theta_Q = \pi/2$. Most strikingly, as the internal friction increases to $\xi_{\text{cell}} = 3.0$, the shear flow behaviour becomes more persistent, on the order of $\mathcal{O}(10^4)$ timesteps. This is the regime where $\xi_{\text{cell}} = \xi$, so that internal friction competes with substrate friction. The flow

is reflected by the kymograph in Figure 6.3 (f). In the dynamic steady state of the viscous system with persistent shear flow, illustrated in Figure 6.3 (e), the cells orient at an angle to the channel, as observed in experiment. A difference between this work and previous experiment, however, is the sign of the shear flow relative to the orientation of cells in the channel [38, 153].

The kymographs in Figure 6.3 indicate the time evolution of flow along the channel at different locations $y$. Moreover, we also quantify the mean velocity along the channel as a function of $y$ position, exactly as in Section 6.3. Figure 6.4 shows graphs of $\langle v_x(y) \rangle$ for the three cases $\xi_{\text{cell}} = 0.0, 1.0, 3.0$, corresponding to the dynamic steady states and kymographs illustrated in Figure 6.3. The case with no internal friction, $\xi_{\text{cell}} = 0.0$, shown in Figure 6.4 (a), clearly exhibits no mean flow, in accord with the lack of flow despite activity, because all the cells align in the same direction. The oscillating shear flow for the system with $\xi_{\text{cell}} = 1.0$ averages over time into a weak flow along the channel, as pictured in Figure 6.4 (b). Lastly, the persistent shear flow for the system with $\xi_{\text{cell}} = \xi = 3.0$ manifests clearly in the mean velocity $\langle v_x \rangle(y)$, shown in Figure 6.4 (c), with cells at the top of the channel travelling to the left and those at the bottom travelling to the right.

### 6.6.2 Orientation

As formulated in Chapter 2, each cell has a traceless nematic tensor $\mathbf{Q}_i$, which is defined by a director $\mathbf{n}_i = |\mathbf{n}_i| (\cos\theta_i, \sin\theta_i)$. The tissue-level nematic tensor is constructed as $\mathbf{Q}(\mathbf{x}, t) = \sum_i \mathbf{Q}_i \phi_i(\mathbf{x}, t)$ and, equally, the components of $\mathbf{Q}(\mathbf{x}, t)$ can be interpreted locally as having a director angle $\theta(\mathbf{x}, t)$. The mean director angle is calculated as

$$\theta_Q(y, t) = \frac{1}{2} \tan^{-1} \left( \frac{\langle Q_{xy} \rangle_x}{\langle Q_{xx} \rangle_x} \right) \tag{6.26}$$

where the inverse tangent is computed using the function `arctan2`, which is sensitive to the signs of its arguments and has a range of all four quadrants. Care must be taken to consider the branch cut of the inverse tangent: when the cells are oriented along the $x$-axis, we choose the branch cut as $\theta = \pi$, while when the cells

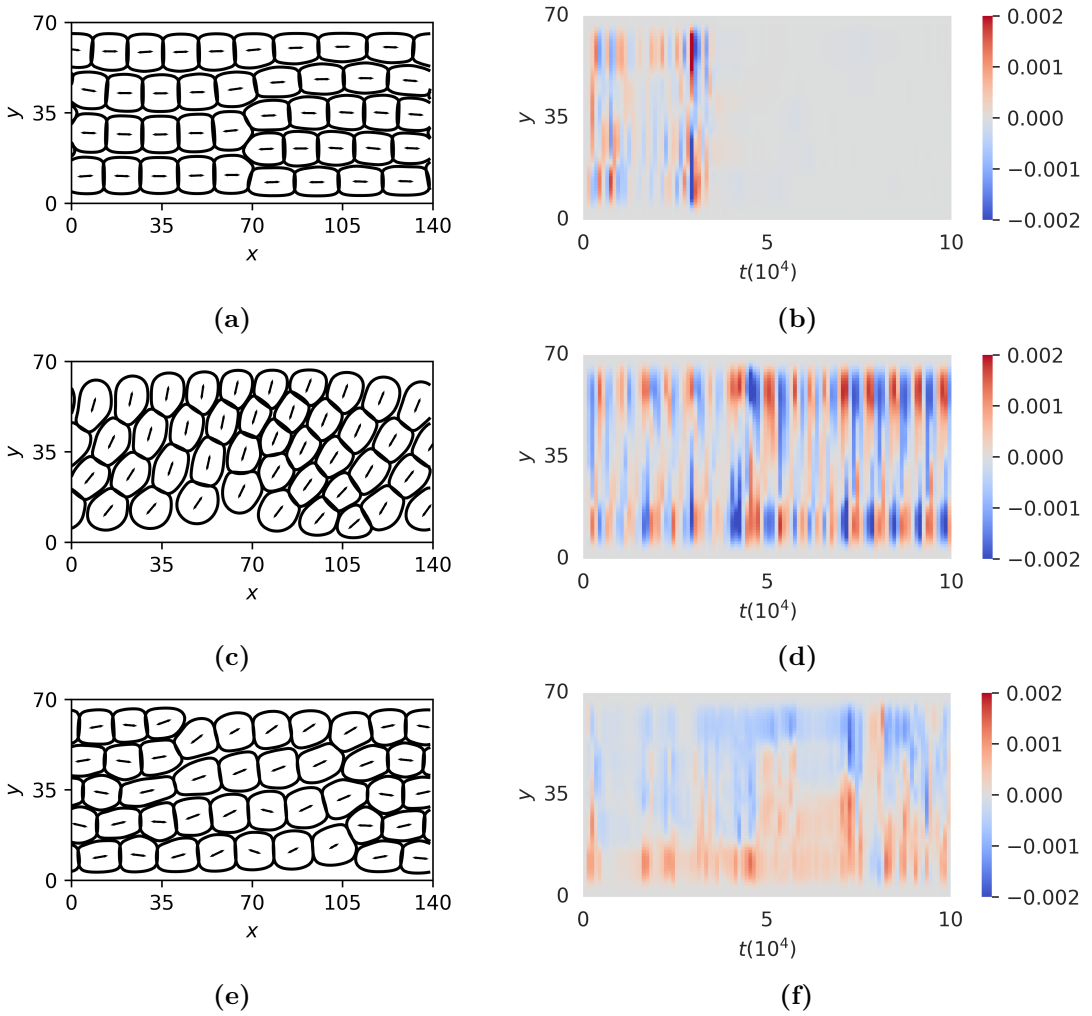


**Figure 6.3:** Snapshots of the dynamic steady state and kymographs of $\langle v_x(y,t)\rangle_x$ for contractile cells in a channel, with $\zeta = -1.0$, for several values of the internal friction coefficient $\xi_{\text{cell}}$. (a), (b) When there is no internal friction, $\xi_{\text{cell}} = 0$, a transient evolves into a quiescent steady state in which the cells orient along the channel. This case is mathematically identical to the model dominated by substrate friction discussed in Section 6.2, absent anchoring enforced at the channel walls. (c), (d) For finite $\xi_{\text{cell}} = 1.0$, an oscillatory state emerges in which a shear flow reverses direction on the order of $\mathcal{O}(10^3)$ timesteps, with associated reorientation of the contractile cells. (e), (f) Finally, for large $\xi_{\text{cell}} = 3.0$, the initial shear flow persists on a timescale $\mathcal{O}(10^4)$ timesteps, although it does reverse direction near $t = 8 \times 10^4$ for a short time. The dynamic steady state of this system is associated with cell orientations at an angle to the channel, which qualitatively matches experimental results up to the sign of the activity [38].

are oriented along the $y$-axis, we set the branch cut at $\theta = 0$. The director angle is then averaged over time for the dynamic steady state:

$$\theta_Q(y) = \langle \theta_Q(y,t) \rangle_t. \tag{6.27}$$

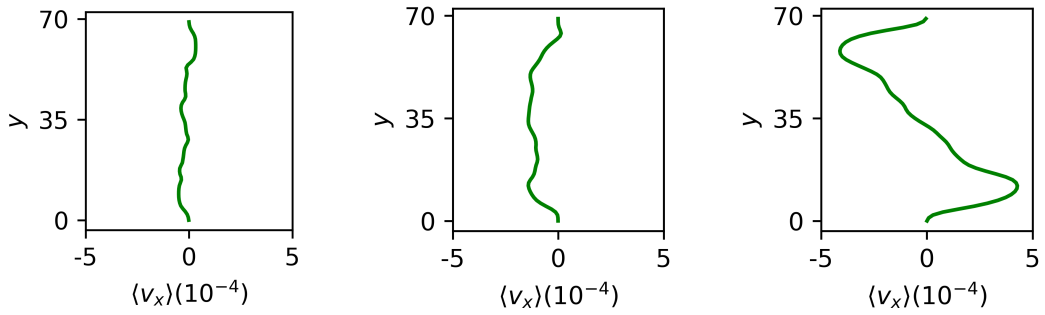


**Figure 6.4:** Mean flow along the channel $\langle v_x(y)\rangle \equiv \langle v_x(\mathbf{x},t)\rangle_{x,t}$. (a) In the absence of friction internal to the monolayer, there is no overall flow. (b) When internal friction is small, $\xi_{\text{cell}} = 1.0$, the oscillating shear flows average out to a small flow along the channel. (c) However, when internal friction is larger, $\xi_{\text{cell}}$, there is a clear mean shear flow in the channel. This is qualitatively similar to experimental results for epithelial cells in confinement [38].

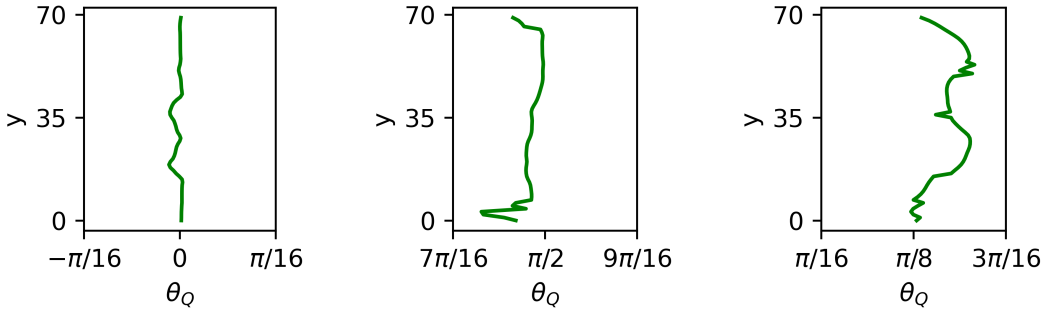


**Figure 6.5:** Mean director angle $\theta_Q(y) \equiv \langle\theta_Q(y,t)\rangle_t$. (a) The quiescent, zero-flow state dominates the mean orientation for $\xi_{\text{cell}} = 0.0$, in which cells align along the channel. (b) Oscillations around the vertical result in a mean $\theta_Q \approx \pi/2$ for cells with $\xi_{\text{cell}} = 1.0$. (c) Finally, the persistent shear flow for cells with $\xi_{\text{cell}} = 3.0$ is reflected in a mean orientation at a finite angle $\theta_Q \approx \pi/8$ to the channel. The variation in $\theta_Q$ around this mean value results in the shear flow.

Figure 6.5 shows $\theta_Q(y)$ for the three systems, with $\xi_{\text{cell}} = 0.0, 1.0$, and 3.0. The cells with no internal friction align on average along the channel, with no variations in $\theta_Q(y)$ that can initiate flow. Similarly, when $\xi_{\text{cell}} = 1.0$, the cells align largely around $\pi/2$, although $\theta_Q$ is on average slightly smaller than $\pi/2$ at $y = 0$ and $y = L_y$, consistent with a bend configuration resulting in a weak flow along the channel, as shown in Figure 6.4 (b) and discussed in Section 6.3. The most striking case is that with $\xi_{\text{cell}} = 3.0$, which shows a clear sinusoidal variation of

$\theta_Q(y)$ across the channel. Interestingly, the profile of $\theta_Q$ appears to vary on a length scale incompatible with the channel, as just less than 2 wavelengths of $\theta_Q$ fit in the channel, and appears to vary as $-\cos\left(\frac{7\pi}{2}\frac{y}{L_y}\right)$. The variation in the director angle sets up a splay profile at the bottom of the channel and a bend profile at the top, and is possibly analogous to the splay instability in a contractile active nematic. Per Chapter 2, these director profiles create flow in opposite directions. We can see this also with a calculation similar to that in Section 6.3. Treating the system as having a continuous translational symmetry along the channel, the net active force in the $x$ direction is given by

$$\mathbf{f}_{\text{active},x} = -\zeta(\nabla \cdot \mathbf{Q})_x = -\zeta \partial_y Q_{yx} = -2\zeta \cos(2\theta_Q)\frac{\partial \theta_Q}{\partial y}. \tag{6.28}$$

The director profile in Figure 6.5 (c) indicates that $\cos(2\theta_Q) > 0$. In conjunction with $\zeta < 0$, this means the sign of the net force in the $x$ direction matches the sign of $\partial\theta_Q/\partial y$. When the internal friction is $\xi_{\text{cell}} = 3.0$, $\theta_Q$ is increasing with $y$ at the bottom of the channel, whereas at the top of the channel, it is decreasing. We expect a shear flow.

There is still variation of $\theta_Q$ in the centre of the channel, but here the resulting net forces compete within individual cells — we can expect flow in one direction or the other as a result of the competition, but passive forces, particularly those arising from the Cahn-Hilliard and area conservation free energies, prevent a single cell from shearing the same way a patch of continuum fluid can [154, 155]. The sign of the shear flow is opposite that shown by Duclos et al. for epithelial cells confined to a channel [38]. The shear flow arises from the variation in $\theta_Q$ and indeed the varation in $\theta_Q$ seen here is different to that observed by Duclos et al. However, the director orientation and flow profile together suggest that the latter experiment uses extensile epithelial cells [38, 153], which naturally flow in the opposite direction to contractile cells because of their different sign of $\zeta$. This prompts a question about the sign of the activity: therefore we comment on extensile cells in a viscous monolayer confined to a channel.

### 6.6.3 Extensile Activity

For a point of comparison, we also run a short simulation for extensile cells with $\zeta = +0.5$. A snapshot of the layer, as well as a kymograph of $\langle v_x(y,t)\rangle$, are shown in Figure 6.6. The extensile cells intercalate readily, as do the extensile cells in Chapter 4, and form capped-line configurations with a strip of cells parallel to the channel at the centre of the channel, but it is unclear whether there is a persistent flow. The time evolution of the system does not exhibit any clear pattern, unlike the case of contractile cells creating an oscillatory shear flow. It is possible that the capped-line state amounts to a bend profile, since it appears there are two regions of nonzero velocity in the negative $x$-direction, which coincide with the locations of the nematic patches. Also, the kymograph in Figure 6.6 shows that these two regions last for the second half of the simulation. It is unclear whether this is a persistent flow, and to clarify the nature of extensile cells in a viscous monolayer requires further study with longer simulations.

In any case, the extensile layer also qualitatively fails to match the results of Duclos et al., particularly because the cells do not align on a diagonal to the channel axis [38]. The phase-field cells may align more readily with one another if they were deformed into spindle shapes, as has been observed in wild-type cells [38, 156]. This could be achieved by implementing extensile intracellular stresses, or through an additional free energy term that deforms the cells into ellipsoidal shapes [102]. A further possibility, and one left to further investigation, is that an extensile activity $\zeta = +0.5$ puts the monolayer already in the active-turbulent regime [7, 87, 147].

## 6.7 Discussion

The work in this chapter is motivated by spontaneous rotation, laminar and shear flow as observed in epithelial monolayers [36–38, 105]. Flow along sufficiently narrow channels, akin to directed migration on micropatterns, is established in monolayers of contractile phase-field cells by implementing anchoring at the confining walls

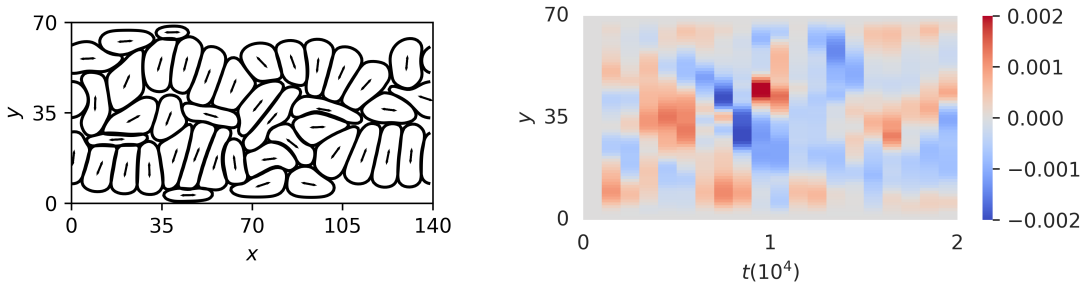


**(a)** **(b)**

**Figure 6.6:** (a) Snapshot of a monolayer with $\zeta = +0.5$ and $\xi_{\text{cell}} = 3.0$, and (b) kymograph of $\langle v_x(y,t)\rangle$ for extensile cells with $\zeta = +0.5$ and $\xi_{\text{cell}} = 3.0$. Although the layer has nonzero viscosity, no clear flow pattern emerges. The cells arrange in small nematic regions with other cells oriented perpendicularly, forming a capped-line state. It is unclear whether the regions of $\langle v_x(y)\rangle < 0$ in the second half of the simulation represent a persistent or transient behaviour. To investigate this issue requires further study with longer simulations.

of the channel, and the magnitude of the velocity is rationalised by scalings with the magnitude of the activity and the width of the channel.

A substantial drawback of the model in the first half of this chapter is that to obtain the flow requires the enforcement of anchoring by hand. In the presence of anchoring, contractile cells exhibit stable orientational order, a bend nematic texture, and flow. However, the aim is to obtain those behaviours spontaneously. Therefore, the multi-phase field model is extended to include a Stokesian force balance in Equation (6.14) that results in a spontaneous shear flow, which becomes more persistent as the viscosity increases. One drawback of the new approach is that the results of this model disagree in sign with experimental results, although the retinal pigment epithelial cells to which we compare are reported to have extensile activity [38, 153].

Running this improved model with internal friction is computationally expensive. Any future work will require thresholding to ensure convergence of the Jacobi scheme. This will necessarily incur additional computing costs, especially for systems with larger internal friction. This is because the magnitudes of the eigenvalues of the iteration matrix $\mathbf{G}$ are controlled by the ratio $\xi/\xi_{\text{cell}}$ as shown in Equation (6.25), and when the eigenvalues $\lambda_G$ have magnitudes closer to unity, the update in Equation (6.21) will take more iterations to converge.

Nevertheless, this improvement to the multi-phase field model opens new avenues for investigation. Firstly, the proof-of-concept nature of the above results must be extended to describe wider channels and channels with ratios of substrate to internal friction $\xi/\xi_{\text{cell}} \ll 1$. Then, equipped with the full Stokesian force balance, the model could be implemented on an annulus in order to model the results of Wan et al. [105]. In addition, the model could be implemented in a box in an attempt to recover vortices, which are a feature of active nematohydrodynamics.

This Chapter has considered only interactions between cells in this improved model with internal friction, and not the effects of self-induced stresses on cell shape or nematic ordering, or flow. Intracellular extensile stresses deform cells into elliptical shapes, as noted in Chapter 4, which could act in this viscous model to promote the nematic ordering of epithelial cells, whether they interact via extensile or contractile neighbour-neighbour stresses. Such elongation, whether arising from intracellular active stresses or an additional free energy term [102], could improve the correspondence between this model and experiments that use spindle-shaped cells in the nematic phase, and could enhance the observed flow [38, 156].

Also, a tissue patterned with a region of active contractile cells, in conjunction with internal friction, could recover primitive streak formation as demonstrated previously in a continuum model for gastrulation [30, 31]. Finally, the oscillatory shear flow in this model is reminiscent to an extent of other oscillatory phenomena observed in epithelia [90] and warrants further investigation, particularly as to how a combination of activity $\zeta$ and viscosity $\xi_{\text{cell}}$ may define a phase space boundary between oscillatory and persistent shear flow.

*"The time has come" the Walrus said,*
*"to talk of many things:*
*Of shoes—and ships—and sealing-wax—*
*Of cabbages—and kings—*
*And why the sea is boiling hot—*
*And whether pigs have wings"*

— Lewis Carroll [2]

# 7 Discussion

'Active matter' is a wide-ranging topic in physics [3] and epithelial monolayers are but a small subclass thereof, yet these two-dimensional systems of interacting agents have a rich and varied phenomenology [8, 9, 12–14]. In Chapter 1, we summarise the individual and collective behaviours of epithelial cells, from persistent random walks [22] to wound healing [12–14] and morphogenesis [11] and contextualise the subsequent Chapters of this thesis. Furthermore, we discuss continuum and agent-based models of active fluids and epithelia, and introduce the notion of the multi-phase field model, which is elaborated on in Chapter 2. In this concluding chapter, we summarise results obtained using a multi-phase field model for epithelia, and provide an outlook for future research to build on the work in this thesis.

## 7.1 Summary of Results

In Chapter 3, we present the simplest cases of a multi-phase field model: the description of a single cell with a rotationally-diffusive active polar force, and the confinement of two such cells to a circular geometry. The main control parameters in this study are the strength $\alpha$ of the polar activity and the energy scale $\omega$ of the intercellular adhesion. We find three behavioural regimes in $\alpha$-$\omega$ phase space: one in which the rotational diffusion of the polar force causes the system to switch

regularly between clockwise and anti-clockwise rotation, another in which noise almost entirely prevents any rotational motion in the system, and a third in which high $\alpha$ and $\omega$ cause rotation and jamming to persist for all time. The ultimate behaviour of the system in this regime depends on whether the initial condition is compatible with rotation or not. With this result in hand, we then suppress polar activity and study the effects of dipolar stresses in the multi-phase field model.

We find in Chapter 4 that phase-field cells with a mixture of extensile and contractile particles tend to microphase separate. This phenomenon has also been observed in experiment [39]. The microphase separation is attributed to differences in diffusivity between extensile and contractile cells. We also find that a mixture of extensile and contractile is required for phase separation: extensile-passive and contractile-passive systems fail to phase separate. Investigation into the energetics of the system suggests that the microphase separation is not thermodynamic in origin. This supports the notion that differential diffusion results in the observed microphase separation, which has also been noted in the literature [117]. A large part of this Chapter was published as 'Cell sorting by active forces in a phase-field model of cell monolayers' [157]. This work has led to additional research using the cellular vertex model to understand active phase separation [158].

Although the contractile clusters in Chapter 4 are active, they are not fluid. This is observed also in the bulk contractile system illustrated in Figure 4.3 (b), which exhibits nematic alignment but not the splay instability expected of a continuum active nematic [40, 81]. We seek therefore to recover fluid behaviour in the multi-phase field model. In Chapter 5, we find that fluctuations in the parameter controlling pairwise cell-cell adhesion cause an epithelial monolayer to exhibit diffusive behaviour in the absence of any polar or dipolar active forces. Although the fluctuations cause diffusion, the lengthscale of the velocity-velocity correlation remains one cell: there are no long-range correlations that are the hallmark of fluid behaviour in the continuum. This Chapter is in preparation for publication as 'Adhesion-Fluctuation-Mediated Fluidisation of Phase-Field Epithelial Monolayers' [159].

Chapter 6 integrates two projects to investigate the flow of epithelial cells along a channel. The first part of the Chapter enforces cell orientation at the wall of the channel to create a stable bend configuration [40]. Although in continuum active nematics, flow results in anchoring [7], here we enforce anchoring to generate a flow. The flow velocity scales with the activity $\zeta$ and the channel width $L_y$ as $\zeta^1 L_y^{-1}$. The implementation of anchoring results in a flow that is intrinsically artificial, so we seek to dispense with anchoring and instead develop a description of viscosity to bring the dynamics of the agent-based multi-phase field model closer to that of a Stokesian fluid in the low-Reynolds-number regime. In the second part of Chapter 6 we implement a viscosity that manifests as an internal friction and solve the resulting Stokes equation using the Jacobi method [152]. In narrow channels with internal friction, a shear flow emerges and becomes more persistent for sufficiently strong friction. This is the sought-after spontaneous shear flow, which has parallels in experiment [38]. Results from the first half of this Chapter were presented as the poster 'Modelling Motility in Confined Epithelia: From Single-Cell to Collective Behaviours' at the summer school Nicolás Cabrera and the conference PhysCell 2022.

## 7.2 Research Outlook

There are several possibilities to further develop the research in this thesis. The model for adhesion fluctuations in Chapter 5 could be enhanced to account for additional features of epithelia, such as catch-bond interactions between membrane proteins and components of the cytoskeleton. Another clear extension of this work is to introduce the adhesion fluctuations, discussed in Chapter 5, into systems with dipolar activity. These fluctuations promote neighbour rearrangements and translational diffusion, and may have implications for the microphase separation seen in Chapter 4. As microphase separation between extensile and contractile cells requires the latter to form solid clusters and to diffuse very slowly, adhesion fluctuations may destroy the cell sorting. On the other hand, mixtures of contractile and passive cells fail to sort because there is no diffusion at all, and the promotion of

neighbour rearrangments *via* adhesion fluctuations may aid microphase separation in such mixtures.

The spontaneous shear flow discussed in Chapter 6 has exciting implications for future research. Not only do the results in the Chapter resemble existing experimental data in a qualitative sense [38], but the implementation of internal friction raises the prospect of more closely matching this agent-based multi-phase field model to active nematohydrodynamics in bulk systems. Additional numerics should investigate the effects of much larger internal frictions. These simulations could be used to recover of vortical flows in circular or rectangular confinement, or the formation of a vortex lattice in yet wider and longer channels [7, 87]. In Chapter 6 we also observe an oscillatory shear flow for intermediate internal friction. It is possible that the short period of the oscillation is a result of the finite size of the system, and that larger systems may exhibit longer-lived oscillations akin to those observed in cellular nematics [90]. Another straightforward extension of the model to better match to continuum theory and experiment is to include intracellular dipolar stresses, which can extend the phase-field cells into spindle shapes and could enhance the nematic ordering in the model tissue.

There are also rich possibilities also to equip the viscous system of Chapter 6 with a pattern of contractile activity. The patterning of activity in a continuum system has been shown to form primitive streak and blastopore structures matching those in chick, and frog gastrulation [30, 31]. It is possible that the multi-phase field system in a circular geometry with a patch of contractile activity could recapitulate primitive streak formation and provide a comparison to experimental systems. The active phase separation observed in Chapter 4 could also have implications for activity patterning in embryogenesis.

In short, the mechanical phenomena described in this thesis using a multi-phase field model for epithelia have rich and varied behaviours. These provide a strong foundation for further research into the collective behaviours of epithelia and can help to understand morphogenesis and embryogenesis.

# References


1. Carroll, L. Alice's Adventures in Wonderland (Macmillan, 1865).
2. Carroll, L. Through the Looking-Glass, and What Alice Found There (Macmillan, 1871).
3. Ramaswamy, S. The Mechanics and Statistics of Active Matter. Annual Review of Condensed Matter Physics **1,** 323–345 (2010).
4. Ramaswamy, S. Active Matter. Journal of Statistical Mechanics (2017).
5. Maass, C. C., Krüger, C., Herminghaus, S. & Bahr, C. Swimming Droplets. Annual review of condensed matter physics **7,** 171–193 (2016).
6. Marchetti, M., Joanny, J., Ramaswamy, S., Liverpool, T., Prost, J., Rao, M. & Simha, R. A. Hydrodynamics of soft active matter. Reviews of Modern Physics **85,** 1143–1189 (2013).
7. Doostmohammadi, A., Ignés-Mullol, J., Yeomans, J. M. & Sagués, F. Active nematics. Nature Communications (2018).
8. Friedl, P. & Gilmour, D. Collective cell migration in morphogenesis, regeneration and cancer. Nature Reviews Molecular Cell Biology **10,** 445–457 (2009).
9. Anderson, P. W. More Is Different. Science **177,** 393–396 (1972).
10. Gilbert, S. F. & Barresi, M. J. F. Developmental biology Eleventh edition. (Sinauer Associates, Inc., Publishers, Sunderland, Massachusetts, U.S.A, 2016).
11. Carmona-Fontaine, C., Matthews, H. K., Kuriyama, S., Moreno, M., Dunn, G. A., Parsons, M., Stern, C. D. & Mayor, R. Contact inhibition of motion *in vivo* controls neural crest directional migration. Nature **456,** 957–961 (2008).
12. Rørth, P. Collective cell migration. Annual review of cell and developmental biology **25,** 407–429 (2009).
13. Mayor, R. & Etienne-Manneville, S. The front and rear of collective cell migration. Nature Reviews Molecular Cell Biology **17,** 97–109 (2016).
14. Ladoux, B. & Mège, R.-M. Mechanobiology of collective cell behaviours. Nat Rev Mol Cell Biol **18,** 743–757 (2017).
15. Cooper, G. M. & Adams, K. W. The cell : a molecular approach. International ninth edition / Geoffrey M. Cooper, Kenneth W. Adams. (Oxford University Press, New York, 2023).
16. Sanchez, T., Chen, D. T. N., DeCamp, S. J., Heymann, M. & Dogic, Z. Spontaneous motion in hierarchically assembled active matter. Nature **491,** 431–434 (2012).

17. Bendix, P. M., Koenderink, G. H., Cuvelier, D., Dogic, Z., Koeleman, B. N., Brieher, W. M., Field, C. M., Mahadevan, L. & Weitz, D. A. A Quantitative Analysis of Contractility in Active Cytoskeletal Protein Networks. Biophysical Journal **94,** 3126–3136 (2008).

18. Murrell, M., Oakes, P. W., Lenz, M. & Gardel, M. L. Forcing cells into shape: the mechanics of actomyosin contractility. Nature Reviews Molecular Cell Biology **16,** 486–498 (2015).

19. Etienne-Manneville, S. Microtubules in Cell Migration. Annual review of cell and developmental biology **29,** 471–499 (2013).

20. Howard, J. & Hyman, A. A. Dynamics and mechanics of the microtubule plus end. Nature (London) **422,** 753–758 (2003).

21. Charras, G. & Sahai, E. Physical influences of the extracellular environment on cell migration. Nature Reviews Molecular Cell Biology **15,** 813–824 (2014).

22. Maiuri, P., Rupprecht, J.-F., Wieser, S., Ruprecht, V., Bénichou, O., Carpi, N., Coppey, M., Beco, S. D., Heisenberg, C.-P., Crespo, C. L., Lautenschlaeger, F., Berre, M. L., Lennon-Dumenil, A.-M., Raab, M., Thiam, H.-R., Piel, M., Sixt, M. & Voituriez, R. Actin Flows Mediate a Universal Coupling between Cell Speed and Cell Persistence. Cell **161,** 374–386 (2015).

23. Theveneau, E., Marchant, L., Kuriyama, S., Gull, M., Moepps, B., Parsons, M. & Mayor, R. Collective Chemotaxis Requires Contact-Dependent Cell Polarity. Developmental Cell **19,** 39–53 (2010).

24. Käfer, J., Hogeweg, P. & Marée, A. F. M. Moving Forward Moving Backward: Directional Sorting of Chemotactic Cells due to Size and Adhesion Differences. PLoS Computational Biology **2,** 518–529 (2006).

25. Levine, H., Kessler, D. & Rappel, W.-J. Directional sensing in eukaryotic chemotaxis: A balanced inactivation model. PNAS **103,** 9761–9766 (2006).

26. Sunyer, R. & Trepat, X. Durotaxis. Current Biology **30,** R371–R392 (2020).

27. Alert, R. & Trepat, X. Physical Models of Collective Cell Migration. Annu. Rev. Condens. Matter Phys. **11,** 77–101 (2020).

28. Abercrombie, M. & Heaysman, J. E. M. Observations on the Social Behaviour of Cells in Tissue Culture: II. “Monolayering" of Fibroblasts. Experimental Cell Research **6,** 293–306 (1954).

29. Blanch-Mercader, C., Yashunsky, V., Garcia, S., Duclos, G., Giomi, L. & Silberzan, P. Turbulent Dynamics of Epithelial Cell Cultures. Physical Review Letters **120,** 208101 (2018).

30. Serra, M., Nájera, G. S., Chuai, M., Plum, A. M., Santhosh, S., Spandan, V., Weijer, C. J. & Mahadevan, L. A mechanochemical model recapitulates distinct vertebrate gastrulation modes. Science Advances **9,** eadh8152 (2023).

31. Chuai, M., Nájera, G. S., Serra, M., Mahadevan, L. & Weijer, C. J. Reconstruction of distinct vertebrate gastrulation modes via modulation of key cell behaviors in the chick embryo. Science Advances **9,** eabn5429 (2023).

32. Saw, T. B., Doostmohammadi, A., Nier, V., Kocgozlu, L., Thampi, S., Toyama, Y., Mercq, P., Lim, C. T., Yeomans, J. M. & Ladoux, B. Topological defects in epithelia govern cell death and extrusion. Nature **544,** 212–216 (2017).

33. Li, D. & li Wang, Y. Coordination of cell migration mediated by site-dependent cell-cell contact. Proceedings of the National Academy of Sciences (2018).

34. Brangwynne, C., Huang, S., Parker, K. K. & Ingber, D. E. Symmetry Breaking in Cultured Mammalian Cells.
In Vitro Cellular & Developmental Biology — Animal **36,** 563–565 (2000).

35. Huang, S., Brangwynne, C., Parker, K. & Ingber, D. Symmetry-Breaking in Mammalian Cell Cohort Migration During Tissue Pattern Formation: Role of Random-Walk Persistence. Cell Motility and the Cytoskeleton **61,** 201–213 (2005).

36. Segerer, F. J., Thüroff, F., Alberola, A. P., Frey, E. & Rädler, J. O. Emergence and Persistence of Collective Cell Migration on Small Circular Micropatterns. Physical Review Letters **114** (2015).

37. Doxzen, K., Vedula, S. R. K., Leong, M. C., Hirata, K., Gov, N. S., Kabla, A. J., Ladoux, B. & Lim, C. T. Guidance of collective cell migration by substrate geometry. Integrative Biology **5,** 1026–1035 (2013).

38. Duclos, G., Blanch-Mercader, C., Yashunsky, V., Salbreux, G., Joanny, J.-F., Prost, J. & Silberzan, P. Spontaneous shear flow in confined cellular nematics. Nature Physics **14,** 728–732 (2018).

39. Balasubramaniam, L., Doostmohammadi, A., Saw, T. B., Narayana, G. H.N. S., Mueller, R., Dang, T., Thomas, M., Gupta, S., Sonam, S., Yap, A. S., Toyama, Y., Mège, R.-M., Yeomans, J. M. & Ladoux, B. Investigating the nature of active forces in tissues reveals how contractile cells can form extensile monolayers. Nature Materials **20,** 1156–1169 (2021).

40. Simha, R. A. & Ramaswamy, S. Hydrodynamic Fluctuations and Instabilities in Ordered Suspensions of Self-Propelled Particles. Physical Review Letters **89,** 058101 (2002).

41. Zhang, J., Yang, N., Kreeger, P. K. & Notbohm, J. Topological defects in the mesothelium suppress ovarian cancer cell clearance. APL Bioengineering **5,** 036103 (2021).

42. Comba, A., Faisal, S. M., Dunn, P. J., Argento, A. E., Hollon, T. C., Al-Holou, W. N., Zamler, M. L.V.D. B., Quass, G. L., Apostolides, P. F., II, C. A., Brown, C. E., Kish, P. E., Kahana, A., Kleer, C. G., Motsch, S., Castro, M. G. & Lowenstein, P. R. Spatiotemporal analysis of glioma heterogeneity reveals COL1A1 as an actionable target to disrupt tumor progression. Nature Communications **13,** 3606 (2022).

43. Heine, P., Lippoldt, J., Reddy, G. A., Katira, P. & Käs, J. A. Anomalous cell sorting behavior in mixed monolayers discloses hidden system complexities. New Journal of Physics, 043034 (2021).

44. Honda, H. Description of Cellular Patterns by Dirichlet Domains : The Two-Dimensional Case. Journal of Theoretical Biology **72,** 523–543 (1978).

45. Honda, H., Yamanaka, H. & Dan-Sohkawa, M. A Computer Simluation of Geometrical Configurations During Cell Division. Journal of Theoretical Biology **106,** 423–435 (1984).

46. Nagai, T. & Honda, H. A dynamic cell model for the formation of epithelial tissues. Philosophical Magazine B **81,** 699–719 (2001).

47. Farhadifar, R., Röper, J.-C., Aigouy, B., Eaton, S. & Jülicher, F. The Influence of Cell Mechanics, Cell-Cell Interactions, and Proliferation on Epithelial Packing. Current Biology **17,** 2095–2104 (2007).

48. Alt, S., Ganguly, P. & Salbreux, G. Vertex models: from cell mechanics to tissue morphogenesis. Philosophical Transactions of the Royal Society B **372,** 20150520 (2016).

49. Bi, D., Lopez, J. H., Schwarz, J. M. & Manning, M. L. A density-independent rigidity transition in biological tissues. Nature Physics **11,** 1074–1079 (2015).

50. Okuda, S., Inoue, Y., Eiraku, M., Adachi, T. & Sasai, Y. Vertex dynamics simulations of viscosity-dependent deformation during tissue morphogenesis. Biomechanics and Modeling in Mechanobiology **14,** 413–425 (2014).

51. Fu, C., Dilasser, F., Lin, S.-Z., Karnat, M., Arora, A., Rajendiran, H., Ong, H. T., Brenda, N. M. H., Phow, S. W., Hirashima, T., Sheetz, M., Rupprecht, J.-F., Tlili, S. & Viasnoff, V. Regulation of intercellular viscosity by E-cadherin-dependent phosphorylation of EGFR in collective cell migration. PNAS **121,** e2405560121 (2024).

52. Rozman, J., Chaithanya, K. V. S., Yeomans, J. M. & Sknepnek, R. From Substrate Dissipation to Internal Dissipation Vertex Model Dynamics: Generating Sustained Flows. arXiv: `2312.11756 [cond-mat.soft]` (2024).

53. Bi, D., Yang, X., Marchetti, M. C. & Manning, M. L. Motility-Driven Glass and Jamming Transitions in Biological Tissues. Physical Review X **6,** 021011 (2016).

54. Krajnc, M. Solid-fluid transition and cell sorting in epithelia with junctional tension fluctuations. Soft Matter **16,** 3209–3215 (2020).

55. Rozman, J., Yeomans, J. M. & Sknepnek, R. Shape-Tension Coupling Produces Nematic Order in an Epithelium Vertex Model. Physical Review Letters **131,** 228301 (2023).

56. Rozman, J., Krajnc, M. & Ziherl, P. Collective cell mechanics of epithelial shells with organoid-like morphologies. Nature Communications **11,** 3805 (2020).

57. Camley, B. A. & Rappel, W.-J. Physical models of collective cell motility: from cell to tissue. J. Phys. D: Appl. Phys. **50,** 113002 (2017).

58. Graner, F. & Glazier, J. A. Simulation of Biological Cell Sorting Using a Two-Dimensional Extended Potts Model. Physical Review Letters **69,** 2013–2016 (1992).

59. Taylor, W. R., Morley, R., Krasavin, A., Gregory, L., Wilkinson, D. G. & Poliakov, A. A Mechanical Model of Cell Segregation Driven by Differential Adhesion. PLoS ONE **7,** e43226 (2012).

60. Durand, M. Large-scale simulations of biological cell sorting driven by differential adhesion follow diffusion-limited domain coalescence regime. PLoS Computational Biology **17,** e1008576 (2021).

61. Bresler, Y., Palmieri, B. & Grant, M. Sharp interface model for elastic motile cells. European Physics Journal E **42** (2019).

62. Saito, N. & Ishihara, S. Active Deformable Cells Undergo Cell Shape Transition Associated with Percolation of Topological Defects. arXiv: 2303.03580 [q-bio.TO] (2023).

63. Mozos, J.-L. & Guo, H. Dendritic Growth at Very Low Undercoolings. Europhysics Letters **32,** 61–66 (1995).

64. Folch, R., Casademunt, J., Hernández-Machado, A. & Ramírez-Piscina, L. Phase-field model for Hele-Shaw flows with arbitrary viscosity contrast. I. Theoretical approach. Physical Review E **60,** 1724–1733 (1999).

65. Nestler, B., Garcke, H. & Stinner, B. Multicomponent alloy solidification: Phase-field modeling and simulations. Physical Review E **71,** 041609 (2005).

66. Nonomura, M. Study on Multicellular Systems Using a Phase Field Model. PLoS ONE **7,** e33501 (2012).

67. Zhang, G., Mueller, R., Doostmohammadi, A. & Yeomans, J. M. Active inter-cellular forces in collective cell motility. Journal of the Royal Society Interface **17,** 20200312 (2020).

68. Mueller, R., Yeomans, J. M. & Doostmohammadi, A. Emergence of Active Nematic Behavior in Monolayers of Isotropic Cells. Physical Review Letters **122,** 048004 (2019).

69. Moure, A. & Gomez, H. Dual role of the nucleus in cell migration on planar substrates. Biomechanics and Model in Mechanobiology **19,** 1491–1508 (2020).

70. Najem, S. & Grant, M. Phase-field model for collective cell migration. Phys. Rev. E **93,** 052405 (2016).

71. Blow, M. L., Thampi, S. P. & Yeomans, J. M. Biphasic, Lyotropic, Active Nematics. Physical Review Letters **113,** 248303 (2014).

72. Ophaus, L., Knobloch, E., Gurevich, S. V. & Thiele, U. Two-dimensional localized states in an active phase-field-crystal model. Physical Review E. **103** (2021).

73. Gennes, P.-G. d. & Prost, J. The Physics of Liquid Crystals 2nd ed. Paperback (Clarendon Press, Oxford, 1995).

74. Beris, A. N. & Edwards, B. J. Thermodynamics of Flowing Systems with Internal Microstructure (Oxford University Press, 1994).

75. Armengol-Collado, J.-M., Carenza, L. N., Eckert, J., Krommydas, D. & Giomi, L. Epithelia are multiscale active liquid crystals 2023.

76. Armengol-Collado, J.-M., Carenza, L. N. & Giomi, L. Hydrodynamics and multiscale order in confluent epithelia

77. Giomi, L. Geometry and Topology of Turbulence in Active Nematics. Physical Review X **3,** 031003 (2015).

78. Shankar, S. & Marchetti, M. C. Hydrodynamics of Active Defects: From Order to Chaos to Defect Ordering. Physical Review X, 041047 (2019).

79. Ramaswamy, S, Simha, R. A. & Toner, J. Active nematics on a substrate: Giant number fluctuations and long-time tails. Europhysics letters **62,** 196–202 (2003).

80. Thampi, S. P. & Yeomans, J. M. Active turbulence in active nematics. European Physical Journal Special Topics **225,** 651–662 (2016).

81. Voituriez, R., Joanny, J. F. & Prost, J. Spontaneous flow transition in active polar gels. Europhysics Letters **70,** 404–410 (2005).

82. Edwards, S. A. & Yeomans, J. M. Spontaneous flow states in active nematics: A unified picture. Europhysics Letters **85,** 18008 (2009).

83. Thampi, S. P., Golestanian, R. & Yeomans, J. M. Instabilities and Topological Defects in Active Nematics. Europhysics Letters **105,** 18001 (2014).

84. Thampi, S. P., Golestanian, R. & Yeomans, J. M. Vorticity, defects and correlations in active turbulence. Philosophical Transactions of the Royal Society A **372,** 20130366 (2014).

85. Hardoüin, J., Hughes, R., Doostmohamadi, A., Laurent, J., Lopez-Leon, T., Yeomans, J. M., Ignés-Mullol, J. & Sagués, F. Reconfigurable flows and defect landscape of confined active nematics. Communications Physics **2** (2019).

86. Giomi, L., Bowick, M. J., Ma, X. & Marchetti, M. C. Defect Annihilation and Proliferation in Active Nematics. Physical Review Letters **110,** 228101 (2013).

87. Shendruk, T. N., Doostmohammadi, A., Thijssen, K. & Yeomans, J. M. Dancing disinclinations in confined active nematics. Soft Matter **13,** 3853 (2017).

88. Giomi, L., Mahadevan, L., Chakraborty, B. & Hagan, M. F. Banding, excitability and chaos in active nematic suspensions. Nonlinearity **25,** 2245–2269 (2012).

89. Samui, A., Yeomans, J. M. & Thampi, S. P. Flow transitions and length scales of a channel-confined active nematic. Soft Matter **17,** 10640–10648 (2021).

90. Peyret, G., Mueller, R., d'Alessandro, J., Begnaud, S., Marcq, P., Mège, R.-M., Yeomans, J. M., Doostmohammadi, A. & Ladoux, B. Sustained Oscillations of Epithelial Cell Sheets. Biophysical Journal **117,** 464–478 (2019).

91. Hughes, R. & Yeomans, J. M. Collective chemotaxis of active nematic droplets. Physical Review E **102** (2020).

92. Bhattacharyya, S. & Yeomans, J. M. Phase Separation Driven by Active Flows. Physical Review Letters **130,** 238201 (2023).

93. Shao, D., Rappel, W.-J. & Levine, H. Computational Model for Cell Morphodynamics. Physical Review Letters **105** (2010).

94. Moure, A. & Gomez, H. Phase-Field Modeling of Individual and Collective Cell Migration. Archives of Computational Methods in Engineering **28,** 311–344 (2019).

95. Camley, B. A., Zhang, Y., Zhao, Y., Li, B., Ben-Jacob, E., Levine, H. & Rappel, W.-J. Polarity mechanisms such as contact inhibition of locomotion regulate persistent rotational motion of mammalian cells on micropatterns. Proceedings of the National Academy of Sciences **111,** 14770–14775 (2014).

96. Bigün, J. Optimal Orientation Direction of Linear Symmetry. Proc. of the IEEE First International Conference on Computer Vision, 433–438 (1987).

97. Szabó, B., Szöllösi, G. J., Gönci, B., Jurányi, Z., Selmeczi, D. & Viczek, T. Phase transition in the collective migration of tissue cells: Experiment and Model. Physical Review E **74** (2006).

98. Giavazzi, F., Paoluzzi, M., Macchi, M., Bi, D., Scita, G., Manning, M. L., Cerbino, R. & Marchetti, M. C. Flocking transitions in confluent tissues. Soft Matter **2014,** 3471–3477 (2018).

99. Toner, J. & Tu, Y. Long-Range Order in a Two-Dimensional Dynamical XY Model: How Birds Fly Together. Phys. Rev. Lett. **75,** 4326–4329 (23 1995).

100. Zhang, G. & Yeomans, J. M. Active forces in confluent cell monolayers. Physical Review Letters **130,** 038202 (2023).

101. Senju, Y. & Tsai, F.-C. A biophysical perspective of the regulatory mechanisms of ezrin/radixin/moesin proteins. Biophysical Reviews **14,** 199–208 (2022).

102. Zhang, G. Polar and dipolar contributions to collective cell motility DPhil thesis. 2022.

103. Viczek, T., Czirók, A., Ben-Jacob, E., Cohen, I. & Shochet, O. Novel Type of Phase Transition in a System of Self-Driven Particles. Physical Review Letters **75** (1995).

104. Löwen, H. Inertial effects of self-propelled particles: From active Brownian to active Langevin motion. The Journal of Chemical Physics **152,** 040901 (2020).

105. Wan, L. Q., Ronaldson, K., Park, M., Taylor, G., Zhang, Y., Gimble, J. M. & Vunjak-Novakovic, G. Micropatterned mammalian cells exhibit phenotype-specific left-right asymmetry. Proceedings of the National Academy of Sciences **108,** 12295–12300 (2011).

106. Moscona, A. & Moscona, H. The Dissociation and Aggregation of Cells from Organ Rudiments of the Early Chick Embryo. Journal of Anatomy **86,** 287–301 (1952).

107. Steinberg, M. S. On the Mechanism of Tissue Reconstruction by Dissociated Cells, I. Population Kinetics, Differential Adhesiveness, and the Absence of Directed Migration. PNAS **48,** 1577–1582 (1962).

108. Krens, S. F. G. & Heisenberg, C.-P. in Forces and Tension in Development (ed Labouesse, M.) 189–213 (Academic Press, 2011).

109. Suzuki, S., Omori, I., Kuraishi, R. & Kaneko, H. Cell sorting and germ layer formation in reconstructed starfish embryos. Development, Growth & Differentiation **63,** 343–353 (2021).

110. Foty, R. A. & Steinberg, M. S. The differential adhesion hypothesis: a direct evaluation. Developmental Biology **278,** 255–263 (2005).

111. Landsberg, K. P., Farhadifar, R., Ranft, J., Umetsu, D., Widmann, T. J., Bittig, T., Said, A., Jülicher, F. & Dahmann, C. Increased Cell Bond Tension Governs Cell Sorting at the *Drosophila* Anteroposterior Compartment Boundary. Current Biology **19,** 1950–1955 (2009).

112. Skamrahl, M., Schünemann, J., Mukenhirn, M., Pang, H., Gottwald, J., Jipp, M., Ferle, M., Rübeling, A., Oswald, T. A., Honigmann, A. & Janshoff, A. Cellular segregation in cocultures driven by differential adhesion and contractility on distinct timescales. Proceedings of the National Academy of Sciences **120,** e2213186120 (2023).

113. Sahu, P., Sussman, D. M., Rübsam, M., Mertz, A. F., Horsley, V., Dufresne, E. R., Niessen, C. M., Marchetti, M. C., Manning, M. L. & Schwarz, J. M. Small-scale demixing in confluent biological tissues. Soft Matter **16,** 3325–3337 (2020).

114. Brodland, G. W. The Differential Interfacial Tension Hypothesis (DITH): A Comprehensive Theory for the Self-Rearrangement of Embryonic Cells and Tissues. Journal of Biomechanical Engineering **124,** 188–197 (2002).

115. Sknepnek, R., Djafer-Cherif, I., Chuai, M., Weijer, C. J. & Henkes, S. Generating active T1 transitions through mechanochemical feedback. eLife **12,** e7986 (2023).

116. Méhes, E., Mones, E., Németh, V. & Vicsek, T. Collective Motion of Cells Mediates Segregation and Pattern Formation in Co-Cultures. PLoS ONE **7,** e31711 (2012).

117. Weber, S. N., Weber, C. A. & Frey, E. Binary Mixtures of Particles with Different Diffusivities Demix. Physical Review Letters **116,** 058301 (2016).

118. McCarthy, E., Damavandi, O., Manna, R. K. & Manning, M. L. Demixing in binary mixtures with differential diffusivity at high density. Physical Review Letters **123,** 098301 (2023).

119. Patch, A., Sussman, D. M., Yllanes, D. & Marchetti, M. C. Curvature-dependent tension and tangential flows at the interface of motility-induced phases. Soft Matter **14,** 7435–7445 (2018).

120. Dolai, P., Simha, A. & Mishra, S. Phase separation in binary mixtures of active and passive particles. Soft matter **14,** 6137–6145 (2018).

121. Belmonte, J. M., Thomas, G. L., Brunnet, L. G., de Almeida, R. M. C. & Chaté, H. Self-Propelled Particle Model for Cell-Sorting Phenomena. Physical Review Letters **100,** 248702 (2008).

122. Vafa, F., Bowick, M. J., Shraiman, B. I. & Marchetti, M. C. Fluctuations can induce local nematic order and extensile stress in monolayers of motile cells. Soft Matter **17,** 3068–3073 (2021).

123. Monfared, S., Ravichandran, G., Andrade, J. & Doostmohammadi, A. Mechanical basis and topological routes to cell elimination. eLife **12,** e8243 (2023).

124. Chen, C.-S., Hong, S., Indra, I., Sergeeva, A. P., Troyanovsky, R. B., Shapiro, L., Honig, B. & Troyanovsky, S. M. $\alpha$-Catenin–mediated cadherin clustering couples cadherin and actin dynamics. Journal of Cell Biology **210,** 647–661 (2015).

125. Wheelock, M. J., Shintani, Y., Maeda, M., Fukumoto, Y. & Johnson, K. R. Cadherin switching. Journal of Cell Science **121,** 727–735 (2007).

126. Curran, S., Strandkvist, C., Bathmann, J., de Gennes, M., Kabla, A., Salbreux, G. & Baum, B. Myosin II Controls Junction Fluctuations to Guide Epithelial Tissue Ordering. Developmental Cell **43,** 480–492 (2017).

127. Yamamoto, T., Sussman, D. M., Shibata, T. & Manning, M. L. Non-monotonic fluidization generated by fluctuating edge tensions in confluent tissues. Soft Matter **18,** 2168 (2022).

128. Mueller, R. & Doostmohammadi, A. Phase field models of active matter. arXiv: `2102.05557 [cond-mat.soft]` (2021).

129. Duclut, C., Paijmans, J., Inamdar, M. M., Modes, C. D. & Jülicher, F. Active T1 transitions in cellular networks. European Physical Journal E **45** (2021).

130. Merkel, M., Etuornay, R., Popović, M., Salbreux, G., Eaton, S. & Jülicher, F. Triangles bridge the scales: Quantifying cellular contributions to tissue deformation. Physical Review E **95,** 032401 (2017).

131. Lin, S.-Z., Merkel, M. & Rupprecht, J.-F. Structure and Rheology in Vertex Models under Cell-Shape-Dependent Active Stresses. Physical Review Letters **130,** 058202 (2023).

132. Duclut, C., Paijmans, J., Inamdar, M. M., Modes, C. D. & Jülicher, F. Nonlinear rheology of cellular networks. Cells & Development **168,** 203746 (2021).

133. Angelini, T. E., Hannezo, E., Trepat, X., Marquez, M., Fredberg, J. J. & Weitz, D. A. Glass-like dynamics of collective cell migration. Proceedings of the National Academy of Sciences **108,** 4714–4719 (2011).

134. Loewe, B., Chiang, M., Marenduzzo, D. & Marchetti, M. C. Solid-Liquid Transition of Deformable and Overlapping Active Particles. Physical Review Letters **125,** 038003 (2019).

135. Malinverno, C., Corallino, S., Giavazzi, F., Bergert, M., Li, Q., Leoni, M., Disanza, A., Frittoli, E., Oldani, A., Martini, E., Lendenmann, T., Deflorian, G., Beznoussenko, G. V., Poulikakos, D., Ong, K. H., Uroz, M., Trepat, X., Parazzoli, D., Maiuri, P., Yu, W., Ferrari, A., Cerbino, R. & Scita, G. Endocytic reawakening of motility in jammed epithelia. Nature Materials **16,** 587–596 (2017).

136. Torquato, S., Truskett, T. M. & Debenedetti, P. G. Is random close packing of spheres well defined? Physical Review Letters **84,** 2064–2067 (2000).

137. Halperin, B. I. & Nelson, D. R. Theory of Two-Dimensional Melting. Physical Review Letters **41,** 121–124 (1978).

138. Nelson, D. R. & Halperin, B. I. Dislocation-mediated melting in two dimensions. Physical Review B **19,** 2457–2484 (1979).

139. Loewe, B., Chiang, M., Marenduzzo, D. & Marchetti, M. C. Solid-Liquid Transition of Deformable and Overlapping Particles. Physical Review Letters **125,** 038003 (2020).

140. Mazo, R. M. Brownian motion : fluctuations, dynamics, and applications 1st ed. (Clarendon Press, Oxford, 2002).

141. Rozman, J., Krajnc, M. & Ziherl, P. Morphologies of compressed active epithelial monolayers. European Physical Journal E **44** (2021).

142. Tetley, R. J., Staddon, M. F., Heller, D., Hoppe, A., Banerjee, S. & Mao, Y. Tissue fluidity promotes epithelial wound healing. Nature Physics **15,** 1195–1203 (2019).

143. Pinheiro, D. & Bellaïche, Y. Mechanical Force-Driven Adherens Junction Remodeling and Epithelial Dynamics. Developmental Cell **47,** 3–19 (2018).

144. Zankoc, C. & Krajnc, M. Elasticity, Stability, and Quasioscillations of Cell-Cell Junctions in Solid Confluent Epithelia. Biophysical Journal **119,** 1706–1711 (2020).

145. Krajnc, M., Stern, T. & Zankoc, C. Active Instability and Nonlinear Dynamics of Cell-Cell Junctions. Physical Review Letters **127,** 198103 (2021).

146. Lin, S.-Z., Bi, D., Li, B. & Feng, X.-Q. Dynamic instability and migration modes of collective cells in channels. Royal Society Interface **16** (2019).

147. Thampi, S. P. Channel confined active nematics. eng. Current opinion in colloid & interface science **61,** 101613– (2022).

148. Chiang, M., Hopkins, A., Loewe, B., Marchetti, M. C. & Marenduzzo, D. Intercellular Friction and Motility Drive Orientational Order in Cell Monolayers. PNAS **121,** e2319310121 (2024).

149. Gulati, P., Shankar, S. & Marchetti, M. C. Boundaries control active channel flows. Frontiers in Physics (2022).

150. Thijssen, K., Khaladj, D. A., Aghvami, S. A., Gharbi, M. A., Fraden, S., Yeomans, J. M., Hirst, L. S. & Shendruk, T. N. Submersed micropatterned structures control active nematic flow, topology, and concentration. Proceedings of the National Academy of Sciences **118** (2021).

151. Chiang, M., Hopkins, A., Loewe, B., Marenduzzo, D. & Marchetti, M. C. Multiphase Field Model of Cells on a Substrate. *Physical Review E*, in press. arXiv: `2403.10715 [cond-mat.soft]` (2024).

152. Saad, Y. Iterative methods for sparse linear systems 2nd ed. (Society for Industrial and Applied Mathematics SIAM, 3600 Market Street Floor 6, Philadelphia PA 19104, Philadelphia, Pa, 2003).

153. Duclos, G, Blanch-Mercader, C, Yashunsky, V, Salbreux, G, Joanny, J.-F., Prost, J & Silberzan, P. Author Correction: Spontaneous shear flow in confined cellular nematics. Nature physics **15,** 868–868 (2019).

154. Lemma, L. M., Norton, M. M., Tayar, A. M., DeCamp, S. J., Aghvami, S. A., Fraden, S., Hagan, M. F. & Dogic, Z. Multiscale Microtubule Dynamics in Active Nematics. Physical Review Letters **127,** 148001 (2021).

155. Serra, M., Lemma, L., Giomi, L., Dogic, Z. & Mahadevan, L. Defect-mediated dynamics of coherent structures in active nematics. Nature physics **19,** 1355–1361 (2023).

156. Duclos, G., Garcia, S., Yevick, H. G. & Silberzan, P. Perfect nematic order in confined monolayers of spindle-shaped cells. Soft Matter **10,** 2346–2353 (2014).

157. Graham, J. N., Zhang, G. & Yeomans, J. M. Cell sorting by active forces in a phase-field model of cell monolayers. Soft Matter **20,** 2955–2960 (2024).

158. Rozman, J. & Yeomans, J. M. Cell Sorting in an Active Nematic Vertex Model. arXiv: `2407.19591 [cond-mat.soft]` (2024).

159. Graham, J. N. & Rozman, J. Adhesion-Fluctuation-Mediated Fluidisation of Phase-Field Epithelial Monolayers. In preparation (2024).